POLITECNICO
MILANO 1863

DIPARTIMENTO DI CHIMICA,
MATERIALI E INGEGNERIA CHIMICA
GIULIO NATTA

Towards the green production of base chemicals

DOCTORAL PROGRAM IN
INDUSTRIAL CHEMISTRY AND CHEMICAL ENGINEERING

Doctoral Dissertation of:
Andrea Isella
10561233

Supervisor:
Prof. Davide Manca

Tutor:
Prof. Matteo Maestri

Head of the Doctoral Program:
Prof. Carlo Alessandro Cavallotti

Year 2025 – Cycle XXXVII

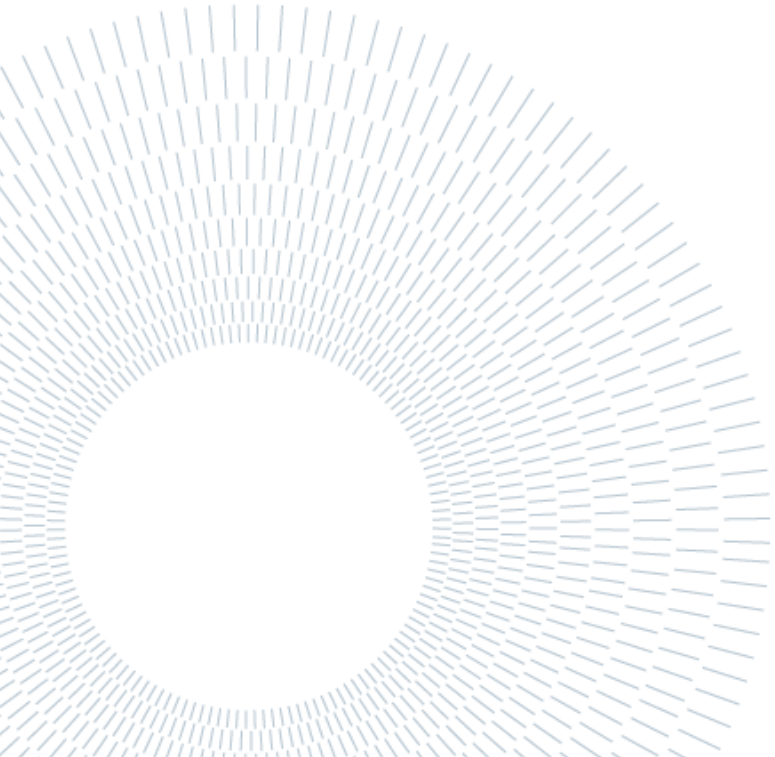

ὁ δὲ κατὰ νοῦν ἐνεργῶν καὶ τοῦτον θεραπεύων καὶ διακείμενος ἄριστα καὶ θεοφιλέστατος ἔοικεν. εἰ γάρ τις ἐπιμέλεια τῶν ἀνθρωπίνων ὑπὸ θεῶν γίνεται, ὥσπερ δοκεῖ, καὶ εἴη ἂν εὔλογον χαίρειν τε αὐτοὺς τῷ ἀρίστῳ καὶ συγγενεστάτῳ (τοῦτο δ᾽ἂν εἴη ὁ νοῦς) καὶ τοὺς ἀγαπῶντας μάλιστα τοῦτο καὶ τιμῶντας ἀντευποιεῖν ὡς τῶν φίλων αὐτοῖς ἐπιμελουμένους καὶ ὀρθῶς τε καὶ καλῶς πράττοντας. ὅτι δὲ πάντα ταῦτα τῷ σοφῷ μάλισθ᾽ὑπάρχει, οὐκ ἄδηλον. θεοφιλέστατος ἄρα. τὸν αὐτὸν δ᾽εἰκὸς καὶ εὐδαιμονέστατον: ὥστε κἂν οὕτως εἴη ὁ σοφὸς μάλιστ᾽εὐδαίμων.

L’uomo che è intellettualmente attivo e che coltiva il suo intelletto sembra che si trovi nella migliore delle disposizioni e che sia il più caro agli dèi. Se, infatti, gli dèi si prendono una qualche cura delle cose umane, come comunemente si ritiene, sarà ragionevole pensare anche che essi si compiacciono dell’elemento umano più elevato e ad essi più affine (e questo sarà l’intelletto), e che ricompensano gli uomini che amano e curano l’intelletto più d’ogni cosa, considerando che questi si curano di cose a loro care e agiscono in modo retto e bello. Che tutto questo si ritrovi soprattutto nel sapiente, è chiaro. Questi, dunque, è il più caro agli dèi. Ed è naturale che lo stesso uomo sia anche il più felice: cosicché anche da questa argomentazione risulterà che il sapiente è sommamente felice.

Aristotele, *Etica Nicomachea* [1179a]

Abstract

Among the main emitters of greenhouse gases in the chemical industry, several base-chemical processes (*e.g.*, ammonia and methanol synthesis) stand out for their high hydrogen consumption. The present doctoral dissertation examines the opportunity of replacing such "grey" hydrogen (as it is typically synthesized from hydrocarbons, *e.g.*, natural gas and coal) with "green" hydrogen (*i.e.* produced via water electrolysis powered by renewable electricity). Nevertheless, major operational issues due to this approach arise from the need to reconcile non-dispatchable renewable energy sources (which inevitably affect the electrolyzer and, therefore, the production of green hydrogen) with the low flexibility of chemical plants (traditionally designed to operate in stationary conditions). Specifically, this thesis introduces new methodologies for the design of (i) systems to produce green hydrogen (*i.e.* aimed at sizing the electrolyzer and its renewable power plant) and (ii) systems allowing the inherent discontinuities of renewable sources to meet the operational requirements of the downstream chemical plant through a material (*i.e.* tanks) or electrical (*i.e.* batteries) storage. Consequently, such tools have been applied to carry out feasibility studies on ammonia plants wherein the fossil-based hydrogen input is partially ("hybrid-green ammonia") or totally ("green ammonia") replaced with green hydrogen.

Keywords: Decarbonization; Renewable energy; Electrolysis; Design-and-operation flexibility; Dynamic operations; Hydrogen storage; Electricity storage; Power-to-X; Green hydrogen; Green ammonia; Multi-objective optimization; Sustainability.

Sommario

Tra i principali responsabili di emissioni di gas climalteranti nell'industria chimica, vi sono diversi processi della chimica di base (*e.g.*, sintesi dell'ammoniaca o del metanolo) che si distinguono per l'elevato consumo di idrogeno. La presente tesi di dottorato si concentra sulla sostituzione di tale idrogeno "grigio" (poiché tipicamente sintetizzato da idrocarburi: *e.g.*, gas naturale o carbone) con idrogeno "verde" (*i.e.* prodotto tramite elettrolisi dell'acqua con elettricità rinnovabile). Nondimeno, la principale complessità operativa introdotta da questo approccio consiste nella necessità di conciliare la non-programmabilità delle fonti energetiche rinnovabili (che si ripercuote inevitabilmente sull'elettrolizzatore e, conseguentemente, sulla produzione di idrogeno verde) con la scarsa flessibilità degli impianti chimici (tradizionalmente concepiti per essere operati in condizioni stazionarie). Nello specifico, in questo lavoro vengono introdotte delle nuove metodologie per la progettazione di (i) sistemi per la produzione di idrogeno verde (*i.e.* volti a dimensionare l'elettrolizzatore ed il parco rinnovabile necessario ad alimentarlo) e (ii) sistemi che consentano di adeguare l'intrinseca discontinuità delle fonti rinnovabili ai requisiti operativi degli impianti chimici a valle tramite accumulo materiale (*i.e.* serbatoi) e/o elettrico (*i.e.* batterie). Dunque, tali strumenti sono stati applicati per condurre studi di fattibilità su impianti per la produzione di ammoniaca il cui fabbisogno di idrogeno fossile risulta parzialmente ("*hybrid-green ammonia*") o totalmente ("*green ammonia*") rimpiazzato con idrogeno verde.

Parole chiave: Decarbonizzazione; Energia rinnovabile; Elettrolisi; Flessibilità; Non-stazionarietà; Accumulo materiale; Accumulo elettrico; Power-to-X; Idrogeno verde; Ammoniaca verde; Ottimizzazione multi-obiettivo; Sostenibilità.

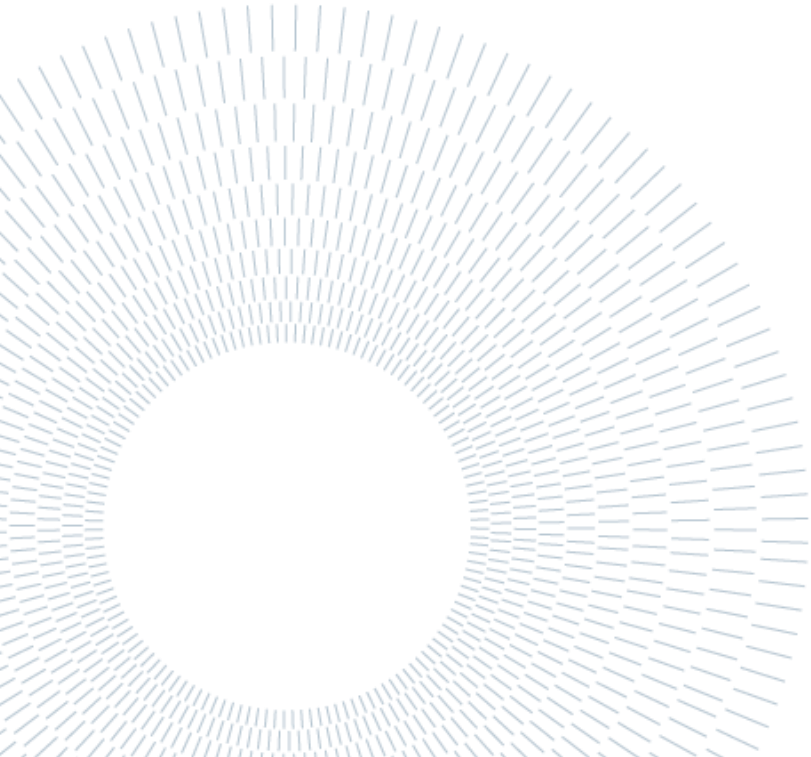

Contents

Introduction

Since the beginning of human history, the relationship between Man and Nature has always been conflictual. Evidence of this can be found in the pagan tradition (*e.g.*, the myths of Prometheus and Heracles: the one asserting the technological domination of nature; the other embodying the role of "civilization hero" who made life easier and safer for people by chasing away wild beasts and clearing land for pastures and crops) as well as in the Judeo-Christian one:

> *Be fertile and multiply and fill the earth. Dread fear of you shall come upon all the animals of the earth and all the birds of the air, upon all the creatures that move about on the ground and all the fishes of the sea; into your power they are delivered. Every creature that is alive shall be yours to eat; I give them all to you as I did the green plants.*
>
> *Genesis* 9:2-3

Yet, throughout the centuries, Science has profoundly reinforced such a paradigm of thinking, especially through the Scientific Revolution. As interestingly pointed out by Zimmerman (1979): if Copernicus, by his heliocentric theory, destroyed the false myth of man as the *physical* center of the universe, Descartes, by his "*cogito, ergo sum*", instead promoted him to the rank of *ontological* center. Thus, it is no surprise to read in his works that:

> *As soon as I had acquired some general notions respecting physics, and beginning to make trial of them in various particular difficulties, had observed how far they can carry us, and how much they differ from the principles that have been employed up to the present time, I believed that I could not keep them concealed without sinning grievously against the law by which we are bound to promote, as far as in us lies, the general good of mankind. For by them I perceived it to be possible to arrive at knowledge highly useful in life; and in room of the speculative philosophy usually taught in the schools, to discover a practical, by means of which, knowing the force and action of fire, water, air the stars, the heavens, and all the other bodies that surround us, as distinctly as we know the various crafts of our artisans, we might also apply them in the same way to all the uses to which they are adapted, and thus render ourselves the lords and possessors of nature.*
>
> Descartes, *Discourse on the Method*, 1637

Only at the dawn of the 19th century, the consequences of this worldview are revealed in their essence and cast doubt on the goodness of such a relationship with nature. For

example, Marx, although considering it necessary (as he was convinced that mankind was the ultimate subject and goal of history), notes that in industrial society:

> *For the first time, nature becomes purely an object for humankind, purely a matter of utility; ceases to be recognized as a power for itself; and the theoretical discovery of its autonomous laws appears merely as a ruse so as to subjugate it under human needs, whether as an object of consumption or as a means of production. In accord with this tendency, capital drives beyond national barriers and prejudices as much as beyond nature worship, as well as all traditional confined, complacent, encrusted satisfactions of present needs, and reproductions of old ways of life. It is destructive towards all of this, and constantly revolutionizes it, tearing down all the barriers which hem in the development of the forces of production, the expansion of needs, the all-sided development of production, and the exploitation and exchange of natural and mental forces.*
>
> Marx, *Grundrisse: Foundations of the Critique of Political Economy*, 1858

Hence the cultural background wherein Chemical Engineering was born and took its first steps, starting from the Second Industrial Revolution. However, "*our innate evolutionary compulsion to seek to exploit as much (wealth, material, energy) as we possibly can*" (Byrne & Fitzpatrick, 2009) has been gradually replaced by increasing sensitivity to sustainability issues starting from the second half of the 20th century. Above all, the call for sustainability emerged in 1987 with the publication of the document *Our Common Future* by the World Commission on Environment and Development (WCED), which stated the definition of sustainable development as "*the development that meets the needs of the present without compromising the ability of future generations to meet their own needs*" (World Commission on Environment and Development, 1987). This event represented the starting point for several further steps, such as the Earth Summit in 1992 in Rio de Janeiro (Brazil), which delivered the celebrated *Agenda 21* (United Nations, 1992), and the World Summit on Sustainable Development in 2002, both promoted by the United Nations. The WCED definition synthesizes in a few words the concept of sustainability and delineates the main features of a new paradigm of development. Also, it deserves credit for having spread the studies on sustainability at an international level. Nevertheless, a more useful definition for engineering decision-making purposes is the one reported by Bakshi and Fiksel (2003): "*A sustainable product or process is one that constrains resource consumption and waste generation to an acceptable level, makes a positive contribution to the satisfaction of human needs, and provides enduring economic value to the business enterprise*". This definition offers interesting hints and outlines the fundamental characteristics of a sustainable system: first, the concept of "an acceptable level" to address sustainability introduces a technical matter (*i.e.* a threshold value for each specific concern is to be specified). In this regard, the choice shall rely on the principle that "*resources must not be consumed at a rate which is faster than the rate of replenishment, and that the waste generation must not exceed the carrying capacity of the surrounding ecosystem*" (Robèrt, 2002). Secondly, the

threefold nature of sustainability (*i.e.* the "three pillars of sustainability"): economic, environmental, and social. In a few words, while an industrial process is economically sustainable when it can incur expenses and earn a profit (*i.e.* it generates new material wealth), it can be said to be environmentally and socially sustainable if harmonized with the needs of the environment (both locally and globally) and society (*e.g.*, workers and population).

Back to Chemical Engineering, technical and economic criteria have traditionally been predominant in the design of chemical processes; now, instead, an increasing number of manufacturing processes call for either redesign (for greenfield projects) or retrofit (for brownfield facilities) to meet the increasingly stringent environmental standards. Therefore, since economic feasibility is usually considered a mandatory pre-condition to develop any industrial activity, environmental sustainability is the major target of chemical companies and, more generally, industrialized countries. Indeed, during the last decades, remarkable efforts have been made to mitigate the environmental impact of chemical processes by improving energy efficiency and developing new "green" technologies. Thus, Green Engineering expresses the natural progression of Chemical Engineering, seeking to achieve "*the design, commercialization, and use of processes and products that are feasible and economical while minimizing the generation of pollution at the source and risk to human health and the environment*" (Allen & Shonnard, 2001). Indeed, Green Engineering relies on 12 principles that offer a general framework for scientists and engineers for applications across different disciplines and design scales (Anastas & Zimmerman, 2003). Such principles focus on fundamental aspects of environmental sustainability, such as pollution prevention, process intensification, heat integration, employment of inherently safe and non-hazardous materials, and improvement of purification efficiency.

This thesis investigates one of the most promising lines of action to decarbonize the chemical industry, thus making chemical engineering a truly "sustainable profession": replacing fossil-based hydrogen with water-based hydrogen (*i.e.* from electrolysis). Specifically, this strategy has been investigated concerning the ammonia industry, although potentially extendable to all those processes featuring high hydrogen consumption. The rationale for this choice will be apparent to the reader in Chapter 1, which provides an overview of today's environmental impact by the chemical industry, followed by a detailed analysis of the challenges related to the production (Chapter 2) and blending into conventional fossil-based processes (Chapter 3) of such "green" hydrogen. Chapters 4 and 5, on the other hand, focus on the main design issues for material and energy storage systems, respectively, having become of primary importance in renewable-powered plants to mitigate the inescapable intermittency of non-dispatchable energy sources (*e.g.*, solar and wind). Finally, Chapter 6 summarizes the lessons learned from previous chapters and addresses the design of a green ammonia plant according to the three pillars of sustainability.

1 Decarbonizing the chemical industry

Introductory comment

The doctoral program started with thorough bibliographical research to identify the most polluting processes of the (petro)chemical industry. In fact, consistent with what is taught in all undergraduate engineering courses, the best way to solve a problem is first to address its top contributor. As ammonia synthesis turned out to be the chemical industry's most carbon-intensive process, here lies the key reason for this thesis's focus on green hydrogen pathways, being the only strategy with the potential to completely decouple the process from fossil fuels (thus eliminating any direct carbon emissions).

The present chapter stems from:

GHG Emissions by (Petro)Chemical Processes and Decarbonization Priorities—A Review

Isella, A., & Manca, D.

Energies, 2022, 15(20), 7560

DOI: https://doi.org/10.3390/en15207560

Abstract

Global warming is becoming an increasing issue, and greenhouse gas (GHG) emissions represent the engine of such a phenomenon. This chapter aims to identify the origin of GHG emissions and focus in detail on the ones related to (petro)chemical industries. The industrial sector is the primary GHG emitter among all the other anthropogenic sources. The chemical industry is the first in charge of that (having accounted for about 6.5% of the global GHG emissions in 2018). Thought-provoking data such as yearly productivities and emission factors related to predominant chemicals prompt the reader to understand the critical activities responsible for carbon-intensive emissions, which should be the first to be decarbonized. Specifically, ammonia synthesis and steam cracking resulted in the most polluting processes of the chemical industry, being responsible for the release of about 440 and 228 Mt_{CO2eq}/y, respectively, in 2020. The same approach also applies to oil refining. Due to the massive amounts of oil barrels produced daily, oil refining is a key player in industrial GHG emissions (about 3% of the global emissions in 2018). Indeed, in 2020, refineries emitted nearly 1313 Mt_{CO2eq}/y.

1.1. Introduction

The awareness of the effects of greenhouse gas (GHG) emissions on climate change and the effort to reduce them from every human activity are increasing daily. In particular, the Paris Agreement (2016), aiming to limit global warming to a maximum of 2 °C (preferably 1.5 °C) compared to pre-industrial levels, represents a true milestone on this path, being the first-ever universal and legally binding international treaty on climate change (European Commission, 2019; UNFCCC, 2022). Nonetheless, GHG emissions still reach very alarming levels. Current estimations agree on global values having risen from 45 to 50 Gt_{CO2eq}/y in the last ten years (Climate Watch, 2022; Our World in Data, 2022) with a monotonically increasing trend (except for 2020, when a considerable decline occurred due to the SARS-CoV-2 pandemic (Rivera *et al.*, 2021)) due to unrelenting demographic growth. According to the United Nations, the world population will reach 8 billion by the end of 2022 (United Nations, 2019). Such a tendency will inevitably lead to increased energy consumption and anthropogenic emissions. Therefore, a proper long-term development strategy for low GHG emissions is recommended, and, in this respect, it is crucial to assess how these emissions are distributed in each human activity. This chapter quantifies the most responsible emitting sources and shows how to prioritize the decarbonizing policies. Indeed, efforts to reduce GHG emissions by focusing on relatively low-polluting human activities would result in negligible benefits, even if very radical. Conversely, even mild environmental mitigation policies targeting remarkably polluting activities would significantly improve the global scale. For clarity, it is essential to elucidate what "human activity" means. GHG emissions can be traced back to the "sector" that

produces them or the "end-user" they are made for. This chapter accounts for both categories by exploiting the data published by Climate Watch (2022) and the World Resources Institute, WRI (2021). It is worth mentioning that most of the reviewed data refer to 2018, which is neither too distant (somewhat well representative of the current situation) nor too close (2018 did not suffer the impact of the economic shutdown originated by the SARS-CoV-2 pandemic). **Table 1.1** lists the analysis results by sector, with the most impactful one being *Electricity and Heat*, as it accounts for almost a third of the total. *Transportation*; *Manufacturing and Construction*; *Agriculture*; *Industrial Processes*; *Fugitive Emissions*; *Buildings*; *Waste*; *Other Fuel Combustion*; and *Land-Use Change and Forestry* follow in descending order (see also **Table 1.1** for further details).

Table 1.1: World GHG emissions (2018) shared among production sectors. Data from Herzog *et al.* (2005); WRI (2021); and Climate Watch (2022).

Sector	GHG Emissions [Mt_{CO_2eq}/y]	Mass Share [-]
Electricity and Heat [1]	15,875	32.2%
Transportation	8418	17.1%
Manufacturing and Construction [2]	6223	12.6%
Agriculture [3]	5803	11.8%
Fugitive Emissions [4]	3354	6.8%
Buildings [5]	3106	6.3%
Industrial Processes	2967	6.0%
Waste [6]	1607	3.3%
Land-Use Change and Forestry	1388	2.8%
Other Fuel Combustion [7]	627	1.3%
Total	49,368	100%

[1] Electricity and heat plants, other Energy Industries. [2] Emissions due to direct fuel combustion in manufacturing and construction sites. [3] Including livestock and manure. [4] Intentional or unintentional releases of gases from human activities (mainly due to fossil fuels extraction, processing, and transmission). [5] Both residential and commercial. [6] Waste management activities (*e.g.*, landfills and wastewater). [7] Emissions related to other unstated sectors, from stationary and mobile sources.

Electricity and Heat is at the top position as global electricity consumption, which recently topped 23 PWh (2019) (IEA, 2021), and most of its production bases on very

carbon-intensive processes. A recent article quantified an average emission factor for electrical energy (which depends on the adopted fuel mix) of about 123 kg_{CO2}/GJ (Kern & Jess, 2021). Such an emission factor is way higher than the ones classically estimated for natural gas, oil, and coal (56, 73, and 95 kg_{CO2}/GJ, respectively) (IPCC, 2006). That is because quite low-efficiency processes mainly produce electricity (consider that the energy ratio of electricity output to fuel input typically ranges from 40 to 50%). However, **Table 1.1** still provides an incomplete picture of those activities responsible for such emissions. Instead of considering "upstream" sectors such as *Electricity and Heat* as distinct categories, it is particularly relevant to analyze how their emissions are distributed among "downstream" activities or, in other terms, which is truly responsible for them. For the sake of detail, let us consider that the main requests for *Electricity and Heat* come from *Industry* and *Buildings*, each representing about 40% of the total demand. Concerning *Manufacturing and Construction*, the leading consumer is *Industry* again, accounting for almost 98% of the whole sector (WRI, 2021). Hence, *Industry* stands as the top emitter among the considered end-users, as from **Table 1.2**.

Table 1.2: World GHG emissions (2018) shared among end-users. Data from WRI (2021) and Climate Watch (2022).

End-User	GHG Emissions [Mt_{CO2eq}/y]	Mass Share [-]
Industry	15,163	30.7%
Buildings	9325	18.9%
Transportation	8617	17.5%
Agriculture	6489	13.1%
Unallocated Fuel Combustion [1]	3425	6.9%
Fugitive Emissions	3354	6.8%
Waste	1607	3.3%
Land-Use Change and Forestry	1388	2.8%
Total	49,368	100%

[1] Includes Own use in electricity, CHP, and heat plants; Nuclear Industry; Biomass combustion; Pumped Storage; Other.

A comparison between **Table 1.1** and **Table 1.2** reveals the remarkable influence of "upstream" activities on "downstream" ones. It is evident that considering emissions associated with productive processes only makes *Industry* a relatively minor emitter (6% of the total GHG emissions). Conversely, considering the indirect emissions (such

as those related to electricity and fuel consumption) makes *Industry* the major emitter (almost 31%).

1.2. Industry

As aforementioned, *Industry* is the primary source of GHG emissions, accounting for almost a third of the total value worldwide.

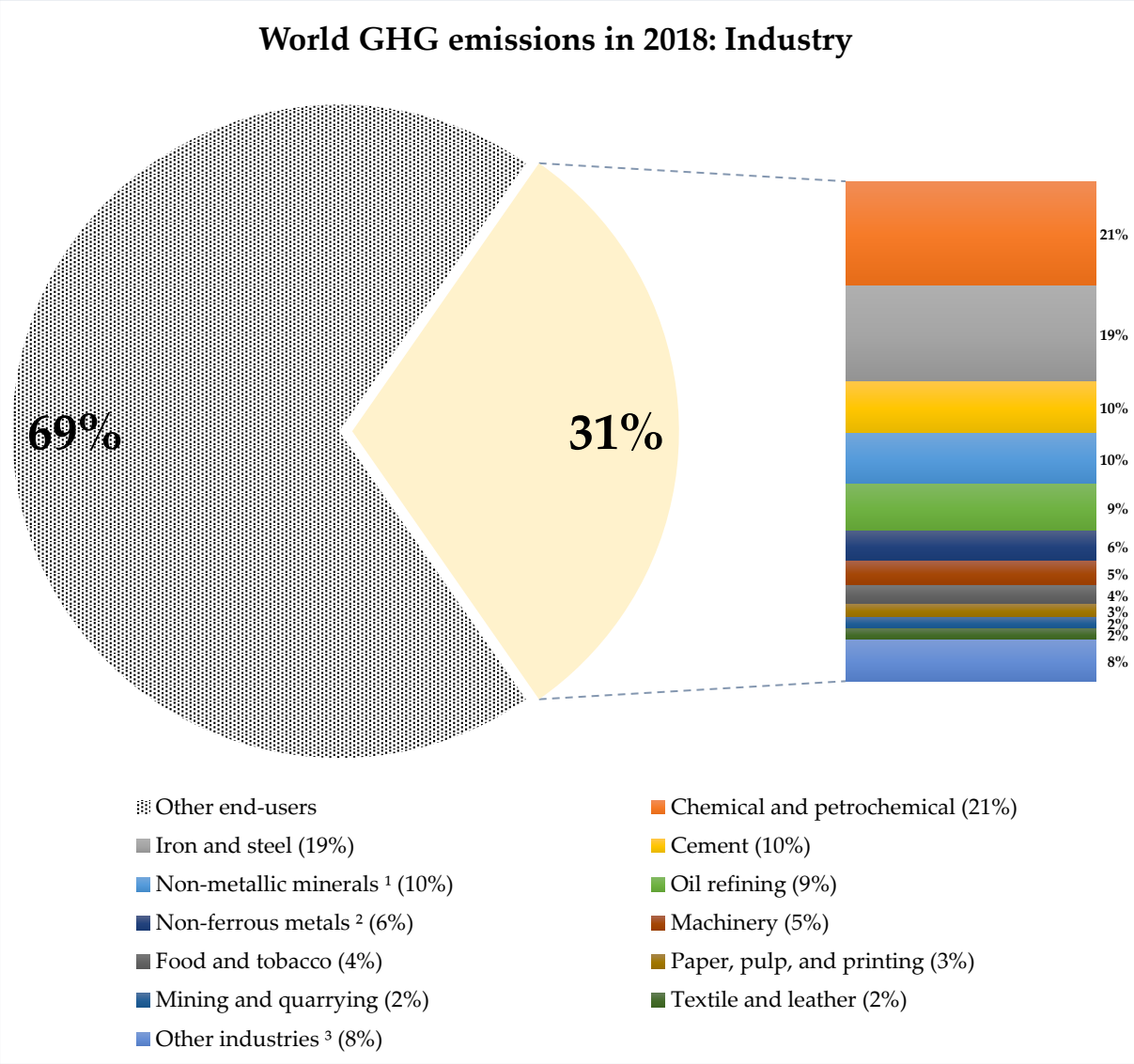

Figure 1.1: Focus on the industry sector's share of global GHG emissions (2018). [1] *E.g.*, lime, glass, and ceramics. [2] *E.g.*, aluminum and magnesium. [3] Includes Transport equipment, Wood industry and products, Electronics. Data from Herzog *et al.* (2005); Jing *et al.* (2020); BP (2021); WRI (2021); and Climate Watch (2022).

Therefore, any effective decarbonization strategy should primarily focus on this sector. **Table 1.1** provides valuable information regarding both environmental and economic data. Worldwide, lawmakers have used these data to enact suitable "carbon taxes",

which charge GHG emissions and/or fuels that release them (Congressional Budget Office, 2013). Carbon taxes promote two synergistic consequences: (i) increase public revenues and (ii) encourage CO_2 reduction. The cost escalation induced by carbon taxes incentivizes companies to manufacture their products in ways that would result in fewer emissions. Ultimately, higher production costs lead to rises in the end-prices of carbon-intensive goods and services, eventually inducing households to moderate use. The assessment of the carbon intensity of each industrial sub-sector must account for both the direct process emissions (*e.g.*, the CO_x and NO_x produced by synthetic routes) and the indirect ones (*e.g.*, arising from utilities such as electricity, fuel gas, fuel oil, *etc.*). An accurate analysis of the diverse industrial sub-sectors is recommended to help address environmental mitigation policies where they are needed the most. Such an approach may prove helpful in identifying the real "players" among the industrial activities in terms of anthropogenic emissions (see **Figure 1.1**). **Figure 1.1** highlights the sub-sectors of *Industry*. As can be seen, some of them are much more polluting than others. They mainly are *Chemical and petrochemical*; *Iron and steel*; *Cement*; *Non-metallic minerals*; *Oil refining*; *Non-ferrous metals*; *Machinery*; *Food and tobacco*; *Paper, pulp, and printing*; *Mining and quarrying*; *Textile and leather*; *Transport equipment*; *Wood industry and products*; *Electronics*, here listed in descending order of GHG emissions. It is worth noting that the first five sub-sectors alone amount to about 70% of the total *Industry* emissions. Finally, it is worth noting that all these five sub-sectors fall under the expertise of chemical engineers.

1.3. Chemicals and Petrochemicals (Plus Oil Refining)

Chemical and petrochemical industry is the top emitter (21%) among all the industrial sub-sectors. Specifically, this sub-sector includes the production of fertilizers, pesticides, pharmaceuticals, plastics, resins, refrigerants, paints, solvents, soaps, perfumes, and synthetic fibers, as well as chemicals derived from oil refining: ethylene, above all, and the so-called petrochemicals, like polyethylene, polystyrene, and polyvinyl chloride. If one adds the emissions due to *Oil refining* (which, after all, is the precursor of almost every petrochemical process), the whole category accounts for about 30% of *Industry* emissions. In other words, the emissions related to the sum of oil refining and chemical plants represent more than 9% (*i.e.* 30% of 31%) of the global GHG emissions. Like *Industry*, it is rather interesting to investigate the most impactful products that make *Chemical and petrochemical industry* so polluting. In this respect, two parameters are crucial to identifying these "dirty" products: their annual production volumes and the corresponding gate-to-gate GHG emission factors. Chemical products may be divided into two main groups by production volumes: commodity and fine chemicals. Commodity chemicals are compounds produced on a vast scale (mostly in dedicated continuous plants) and sold at relatively low prices. Fine chemicals are synthesized in limited volumes (usually in multipurpose batch plants) and sold at higher prices. In our investigation, the compounds of interest are commodity chemicals. This category

is associated with significantly high production volumes and is responsible for direct and indirect GHG emissions.

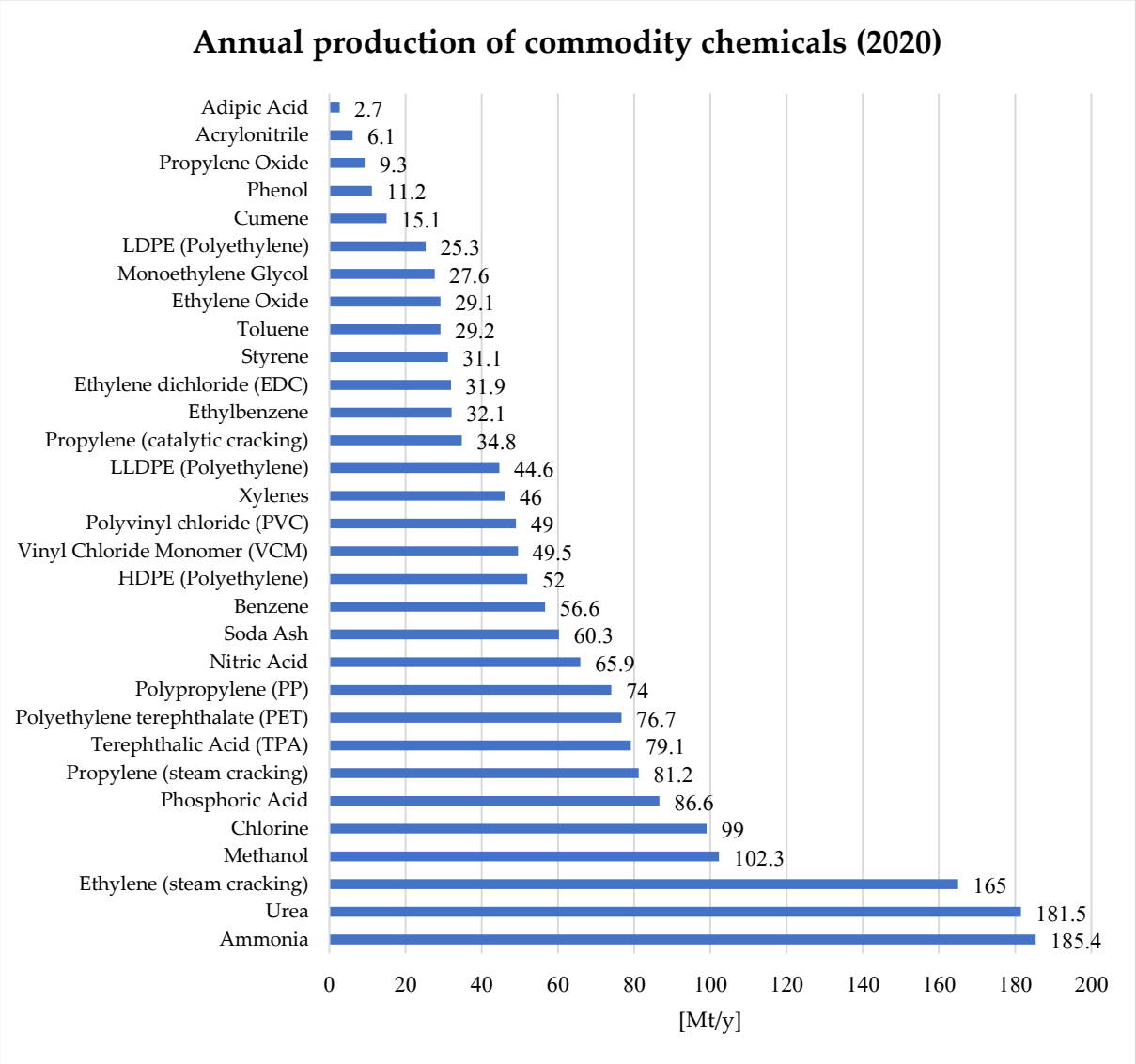

Figure 1.2: Annual production of commodity chemicals (2020). Note that 4165.1 Mt/y of oil (including crude oil, shale oil, oil sands, condensates, and natural gas liquids) were processed in the same year (BP, 2021). Data from Krungsri Research (2019); Beroe (2020a, 2020b, 2020c); IHS Markit (2020a, 2020b, 2021, 2022); NexantECA (2020); ChemAnalyst (2021); IFA (2021a, 2021b, 2021c); Invest Saudi (2021a, 2021b); Mordor Intelligence (2021a, 2021b); ReportLinker (2021); BlueWeave Consulting (2022a, 2022b); ECHEMI (2022); Merchant Research and Consulting Ltd. (2022); MMSA (2022); and Statista (2022a, 2022b, 2022c, 2022d, 2022e, 2022f, 2022g, 2022h).

In addition, it is involved in several downstream processes (*e.g.*, the ones needed to synthesize most fine chemicals). In this respect, **Figure 1.2** lists the analyzed commodity chemicals and reports their production volumes in 2020. The second fundamental indicator to be evaluated is the gate-to-gate GHG emission factor. This

parameter, borrowed from the Life Cycle Assessment (LCA) jargon (Klöpffer, 2005; Klöpffer & Grahl, 2014) and typically expressed in mass of carbon dioxide equivalent per a specific "functional unit", quantifies the carbon footprint associated with a production plant (from the entrance "gate" to the exit "gate"). Similar indicators are the cradle-to-gate and cradle-to-grave GHG emission factors, wherein "cradle" accounts for the extraction of raw materials. At the same time, "grave" considers the waste disposal of the products. Hence, the gate-to-gate perspective represents a methodological approach that deliberately constrains the system boundary to the operational limits of a specific manufacturing facility. Accordingly, chemical engineers predominantly resort to gate-to-gate assessments due to compelling pragmatic and methodological considerations. Principally, it allows for direct operational control and measurement precision, enabling engineers and operators to quantify environmental impacts through empirically collected data within their immediate sphere of influence. Furthermore, gate-to-gate assessments align seamlessly with existing industrial monitoring protocols, regulatory compliance frameworks, and internal performance metrics, making them administratively convenient and economically tractable. Such an approach also mitigates the complexity inherent in comprehensive lifecycle analyses by focusing on measurable, immediate environmental parameters, thus allowing engineers to generate targeted interventions with demonstrable operational improvements. By constraining the investigative boundaries, chemical engineers can develop more focused and implementable sustainability strategies directly addressing process inefficiencies and environmental criticalities within their controlled industrial context. On the other hand, the primary limitation of this approach lies in its potential to disguise significant environmental burdens associated with material sourcing, transportation, and end-of-life product disposal, which may substantially exceed the direct operational footprint. Consequently, chemical engineers employing exclusively gate-to-gate assessments might develop an incomplete picture of the comprehensive environmental impact of their technological interventions. Nevertheless, since this chapter focuses on the *Industry* sector, the cradle-to-grave perspective may prove inappropriately loose. Additionally, regarding the calculations, the broader cradle-to-grave scope may result in subtle errors, particularly concerning "double counting". Indeed, since many chemicals, once synthesized, convert into reagents for subsequent downstream processes and products, it is advisable to analyze each production step individually. For instance, when computing the amount of GHG emissions related to ethylene and polyethylene syntheses, it is better not to use "cradle-to-" data as by doing so, one would compute twice the emissions from the ethylene process, as ethylene is also the cradle of polyethylene. Conversely, suppose one considers the emissions of the sole production steps for each species (*i.e.* "gate-to-gate"). In that case, there are neither risks of overestimation nor underestimation errors since each compound is handled as an isolated compartment. Accordingly, **Figure 1.3** lists the gate-to-gate GHG emission factors of the leading commodity processes (alongside the main processes typically performed in oil refineries).

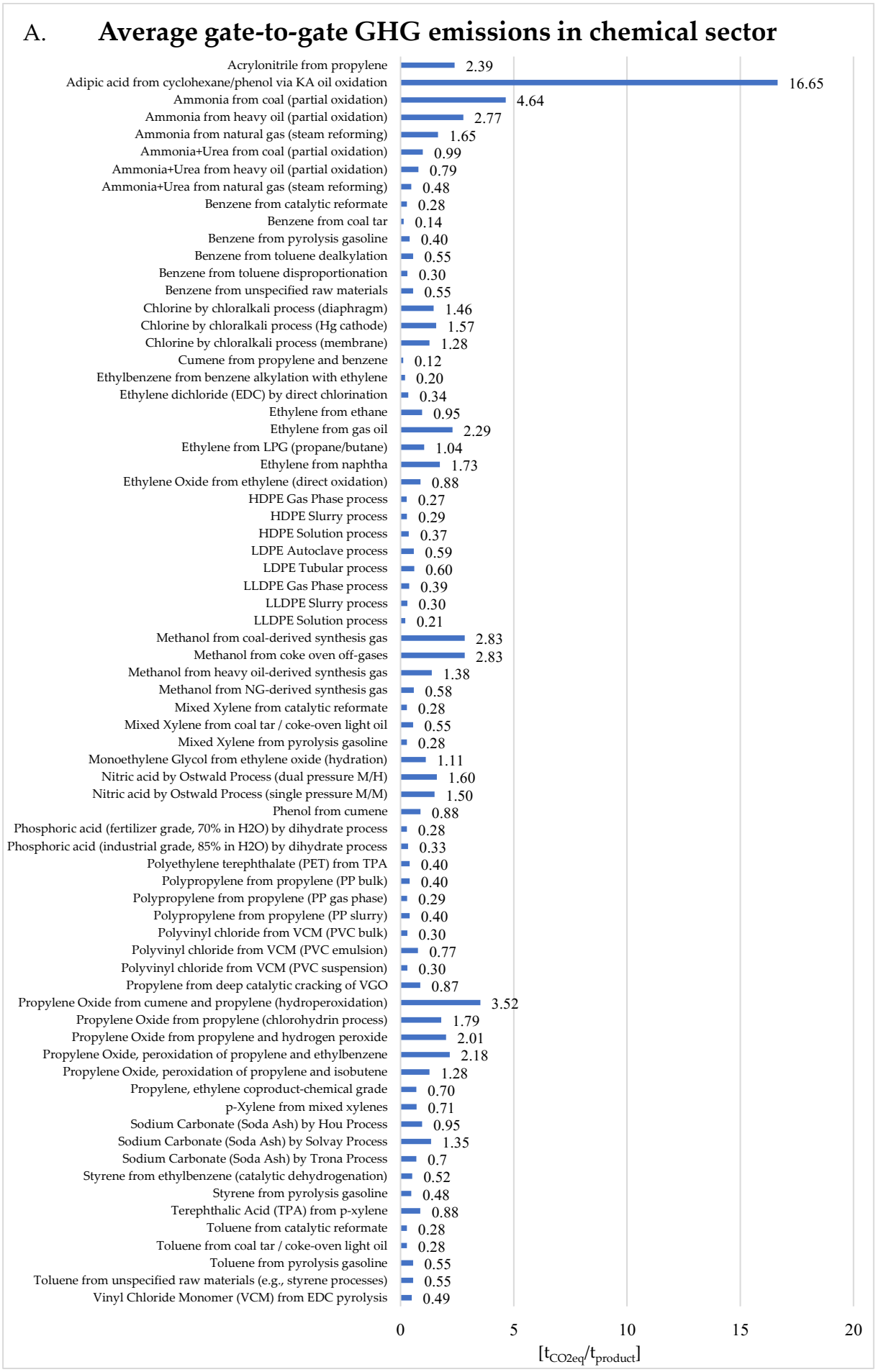
A.
Average gate-to-gate GHG emissions in chemical sector
Acrylonitrile from propylene 2.39
Adipic acid from cyclohexane/phenol via KA oil oxidation 16.65
Ammonia from coal (partial oxidation) 4.64
Ammonia from heavy oil (partial oxidation) 2.77
Ammonia from natural gas (steam reforming) 1.65
Ammonia+Urea from coal (partial oxidation) 0.99
Ammonia+Urea from heavy oil (partial oxidation) 0.79
Ammonia+Urea from natural gas (steam reforming) 0.48
Benzene from catalytic reformate 0.28
Benzene from coal tar 0.14
Benzene from pyrolysis gasoline 0.40
Benzene from toluene dealkylation 0.55
Benzene from toluene disproportionation 0.30
Benzene from unspecified raw materials 0.55
Chlorine by chloralkali process (diaphragm) 1.46
Chlorine by chloralkali process (Hg cathode) 1.57
Chlorine by chloralkali process (membrane) 1.28
Cumene from propylene and benzene 0.12
Ethylbenzene from benzene alkylation with ethylene 0.20
Ethylene dichloride (EDC) by direct chlorination 0.34
Ethylene from ethane 0.95
Ethylene from gas oil 2.29
Ethylene from LPG (propane/butane) 1.04
Ethylene from naphtha 1.73
Ethylene Oxide from ethylene (direct oxidation) 0.88
HDPE Gas Phase process 0.27
HDPE Slurry process 0.29
HDPE Solution process 0.37
LDPE Autoclave process 0.59
LDPE Tubular process 0.60
LLDPE Gas Phase process 0.39
LLDPE Slurry process 0.30
LLDPE Solution process 0.21
Methanol from coal-derived synthesis gas 2.83
Methanol from coke oven off-gases 2.83
Methanol from heavy oil-derived synthesis gas 1.38
Methanol from NG-derived synthesis gas 0.58
Mixed Xylene from catalytic reformate 0.28
Mixed Xylene from coal tar / coke-oven light oil 0.55
Mixed Xylene from pyrolysis gasoline 0.28
Monoethylene Glycol from ethylene oxide (hydration) 1.11
Nitric acid by Ostwald Process (dual pressure M/H) 1.60
Nitric acid by Ostwald Process (single pressure M/M) 1.50
Phenol from cumene 0.88
Phosphoric acid (fertilizer grade, 70% in H2O) by dihydrate process 0.28
Phosphoric acid (industrial grade, 85% in H2O) by dihydrate process 0.33
Polyethylene terephthalate (PET) from TPA 0.40
Polypropylene from propylene (PP bulk) 0.40
Polypropylene from propylene (PP gas phase) 0.29
Polypropylene from propylene (PP slurry) 0.40
Polyvinyl chloride from VCM (PVC bulk) 0.30
Polyvinyl chloride from VCM (PVC emulsion) 0.77
Polyvinyl chloride from VCM (PVC suspension) 0.30
Propylene from deep catalytic cracking of VGO 0.87
Propylene Oxide from cumene and propylene (hydroperoxidation) 3.52
Propylene Oxide from propylene (chlorohydrin process) 1.79
Propylene Oxide from propylene and hydrogen peroxide 2.01
Propylene Oxide, peroxidation of propylene and ethylbenzene 2.18
Propylene Oxide, peroxidation of propylene and isobutene 1.28
Propylene, ethylene coproduct-chemical grade 0.70
p-Xylene from mixed xylenes 0.71
Sodium Carbonate (Soda Ash) by Hou Process 0.95
Sodium Carbonate (Soda Ash) by Solvay Process 1.35
Sodium Carbonate (Soda Ash) by Trona Process 0.7
Styrene from ethylbenzene (catalytic dehydrogenation) 0.52
Styrene from pyrolysis gasoline 0.48
Terephthalic Acid (TPA) from p-xylene 0.88
Toluene from catalytic reformate 0.28
Toluene from coal tar / coke-oven light oil 0.28
Toluene from pyrolysis gasoline 0.55
Toluene from unspecified raw materials (e.g., styrene processes) 0.55
Vinyl Chloride Monomer (VCM) from EDC pyrolysis 0.49
0
5
10
15
20
[tCO2eq/tproduct]

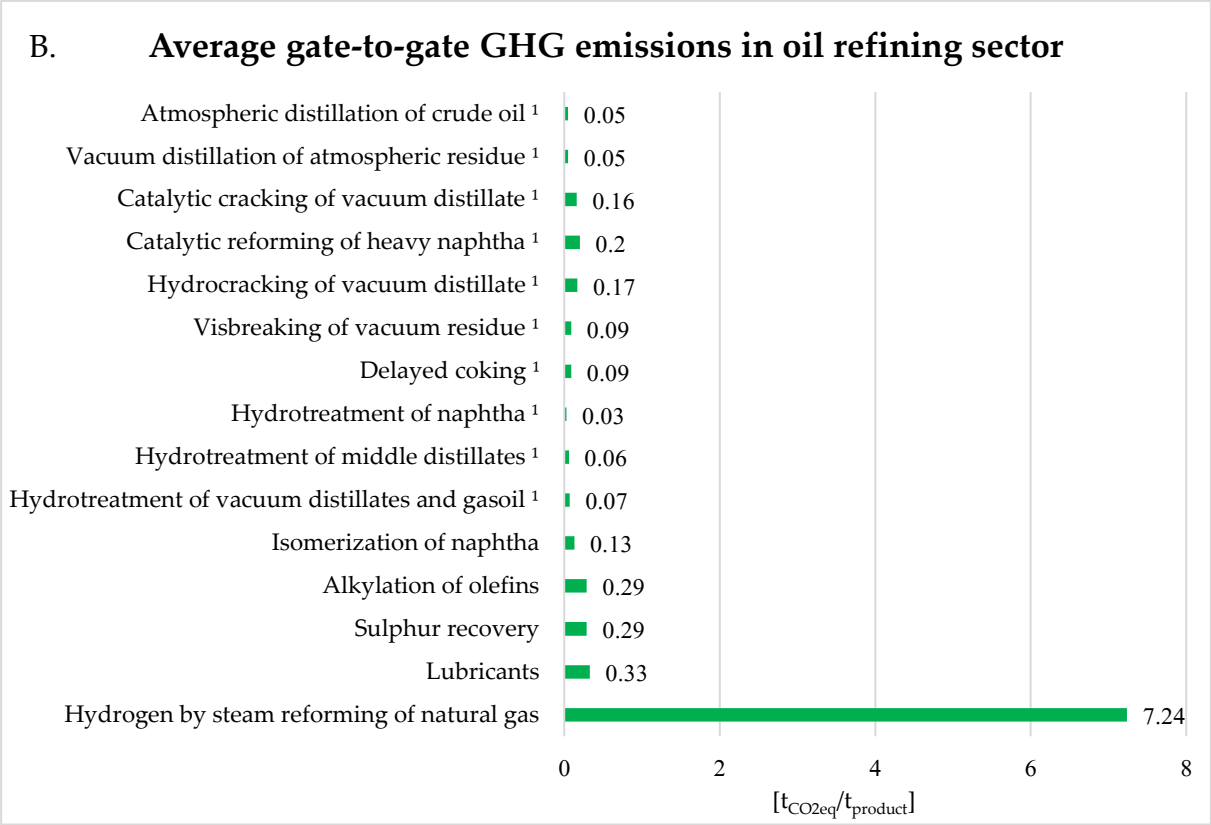

Figure 1.3: Average gate-to-gate greenhouse gas emission factors related to the main processes and products of the (petro)chemical (Panel A, in blue) and oil refining (Panel B, in green) industries. [1] Expressed per metric ton of feedstock (instead of per metric ton of product). Data from Bach *et al.* (2005); Althaus *et al.* (2007); Euro Chlor (2010); United States Senate: Committee on Finance (2010); IEA *et al.* (2013); European Commission *et al.* (2017); and Corona *et al.* (2018).

Concerning **Figure 1.3**, the emission factors cover very different ranges, where the lower is the better, as they quantify the carbon intensity of the process. Secondly, the emission factors were selected from diverse sources, with a few as old as 15 years. Nevertheless, such values should not be considered outdated as they result from material and energy balances, which are universally valid. Deviations may arise concerning time-dependent variables such as (i) the change in the fuel mix of electricity generation or (ii) remarkable modifications in the design of the process units involved. These would lead to updated material and energy balances (*e.g.*, new arrangements of the CO_2 streams within the battery limits of the production plant). Regarding this last point, it is also worth remarking that the 15-year span previously mentioned still falls within the average life of existing chemical plants, whose commissioning and main technological assets date back to those years. Thirdly, the reported values also account for the contribution of indirect emissions (*e.g.*, the ones due to power and fuel consumption). For instance, chlorine is produced by a carbon-free electrochemical reaction from sodium chloride and water. Therefore, no emissions associated with its synthesis are expected. However, chlorine production may generate GHG emissions relating to the electricity consumed for the reaction (carried out within an electrolyzer).

Since the current fuel mix of electricity generation is rather carbon-intensive, the resulting emission factors for chlorine synthesis are significant. Moreover, it is worth considering that these emission factors are expressed per metric ton of product. This means that the lighter the product, the higher the emission factor. For instance, if one considers two compounds produced in the same reaction with the same stoichiometric coefficients, more feedstock is required to collect a metric ton of the lightest one. This explains why the same process (*e.g.*, natural gas steam reforming) exhibits different emission factors for the products being considered. When referring to the production of 1 kg of hydrogen, the corresponding emission factor is 7.24 kg_{CO2eq}/kg_{H2} (see **Figure 1.3**). Conversely, when referring to the production of 1 kg of ammonia, the emission factor is 1.65 kg_{CO2eq}/kg_{NH3} (as 1 kg of ammonia is made of 0.18 kg of hydrogen that is produced in the steam reformer and contributes to CO_2 emissions, while the remaining 0.72 kg comes from nitrogen and does not affect the carbon intensity of the reaction). After having collected the two main parameters of interest (*i.e.* yearly productivity of the main chemicals and their emission factors) for all the examined chemicals, the carbon footprint of each compound can be evaluated by multiplying its annual production(s) by the emission factor(s) of its process route(s). For instance, in the case of ammonia, **Figure 1.3** lists its three main synthetic routes: (i) partial oxidation of coal; (ii) partial oxidation of oil; and (iii) steam reforming of natural gas, as these processes nearly account for 22%, 6%, and 72% of ammonia production worldwide, respectively (Bicer *et al.*, 2016; Kern & Jess, 2021). Such an approach to quantifying GHG emissions is simplified by grounding on average emission factors to account for whole classes of production plants. However, production plants, although based on the same process, may differ regarding direct and indirect emissions. For instance, deviations may occur due to the operation of the plant, its size, age, location, and underlying technology. Moreover, the present analysis discarded minor synthesis routes due to their negligible contribution to the global scale (*e.g.*, ammonia from water electrolysis). However, the assessment procedure proposed in this chapter should be relatively reliable in quantifying the GHG emissions of the (petro)chemical industries, although based on some approximations. **Figure 1.4** shows that oil refining is the greatest emitter among the chemical processes. Indeed, oil refining accounts for about 3% of the annual global anthropogenic GHG emissions. This is not due to the relatively high carbon intensity of refinery processes (which present quite low emission factors, as reported in **Figure 1.3**) but to the massive quantities that undergo such treatments. In fact, according to BP (2021), more than 88 million bbl/d of crude oil were extracted and refined in 2020 (in 2019, just before the SARS-CoV-2 pandemic, that value was almost 95 million bbl/d). On the other hand, ammonia is the most pollutant chemical as it reaches a total amount of GHG emissions, almost a third of the oil refining sector. In this case, the significant production volumes of ammonia (over 185 Mt/y in 2020, as of **Figure 1.2**) contribute to such an outcome. At the same time, there is also a significant problem in terms of carbon intensity for its synthesis. As easily understandable from **Figure 1.3**, the gate-to-gate GHG emission factors for ammonia production strongly

depend on the fossil feedstock provided to the reactors: the carbon-richer the fossil fuel, the dirtier the whole process. Specifically, let us consider the most critical player, China, and another notable one, India. They produce ammonia mainly through coal- and oil-based processes (Bicer *et al.*, 2016; IEA, 2007).

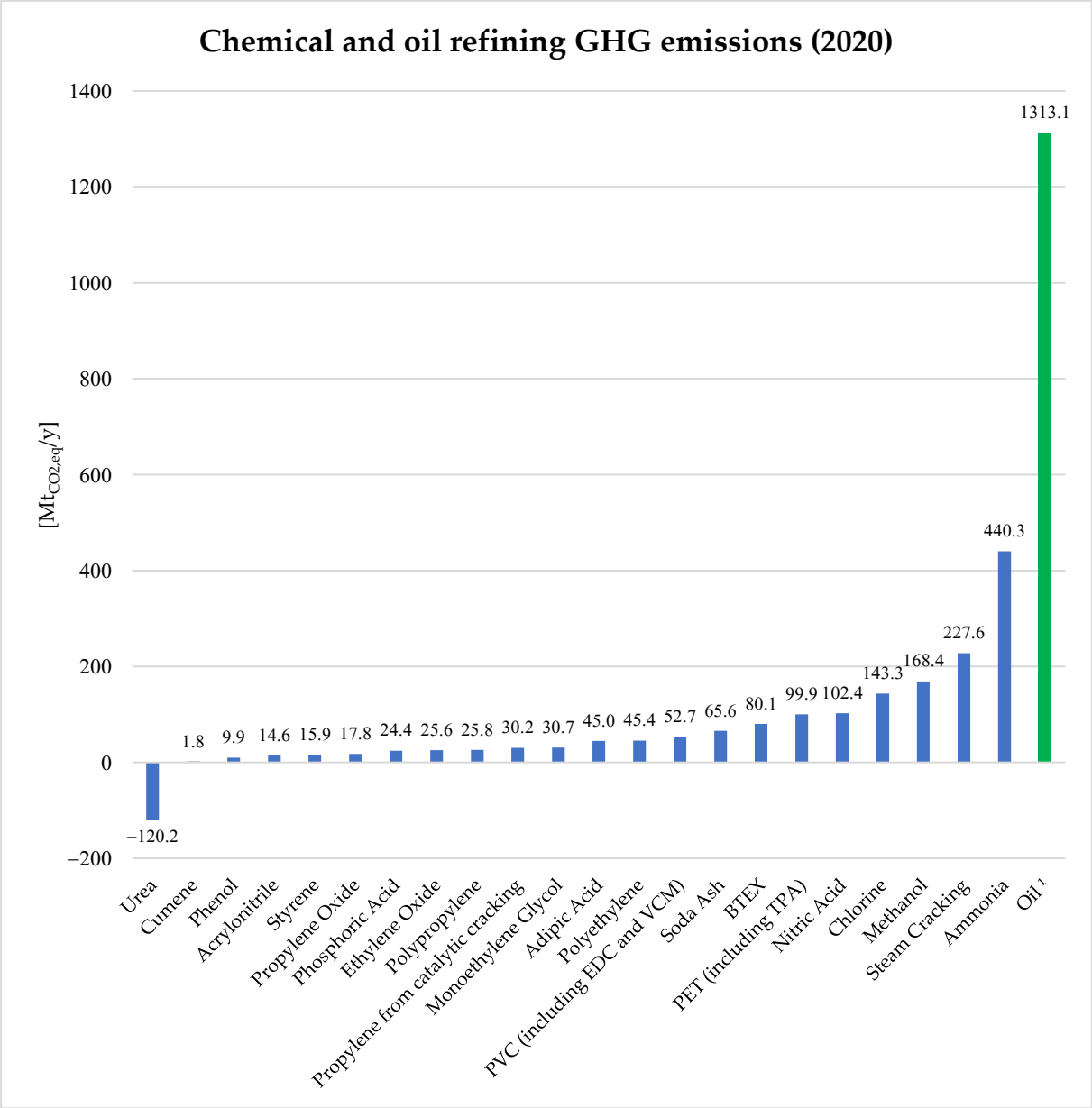

Figure 1.4: Annual global greenhouse gas emissions related to the main products of the chemical (in blue) and oil refining (in green) industry (2020). [1] "Oil" includes crude oil, shale oil, oil sands, condensates, and natural gas liquids. Based on the same references of **Figure 1.2** and **Figure 1.3** with the addition of Syed and Vernon (2002); Bach *et al.* (2005); Althaus *et al.* (2007); Nexant (2009); IEA *et al.* (2013); Fischer *et al.* (2014); Akah and Al-Ghrami (2015); Belis *et al.* (2015); LyondellBasell (2015); Bicer *et al.* (2016); IHS Markit (2016); Azmi and Aziz (2017); European Commission *et al.* (2017); Methanol Institute (2019); ChemIntel360 (2021); IRENA and Methanol Institute (2021); Kern and Jess (2021); Allied Market Research (2022); and IHS Markit (2022).

Such evidence makes ammonia stand as the leading chemical in this ranking. Next, on the third step of the podium, we have steam cracking, which is the main process to produce ethylene and propylene. Such olefins are the precursors of many chemicals, primarily the ones related to the plastics sector. Among all the other compounds, it is worth mentioning the very tail end of the ranking in **Figure 1.4**, urea, which presents a beneficial effect (*i.e.* negative contribution) as CO_2 is consumed for its synthesis. Indeed, one mole of urea is made by combining two moles of ammonia and one mole of carbon dioxide (along with the release of one mole of water): this explains why such a chemical presents a negative balance. However, each urea molecule guarantees a "temporary storage" of CO_2. Mainly utilized as a nitrogen-release fertilizer, when applied to soil, urea hydrolyzes in the presence of the urease enzyme to ammonia and carbon dioxide (Meessen, 2010). Afterward, ammonia is bacteriologically converted to nitrate (and, as such, absorbed by crops), and carbon dioxide is emitted again into the atmosphere. Finally, the lack of other prominent commodity chemicals is attributable to small values of at least one of the two parameters examined (*i.e.* annual production and emission factors). For instance, sulfuric acid is missing in **Figure 1.4** mainly due to its relatively "clean" synthesis, having gate-to-gate GHG emission factors below 10^{-2} t_{CO2eq}/t_{H2SO4} (Althaus *et al.*, 2007). Consequently, despite 256 Mt/y of sulfuric acid production in 2020 (Statista, 2022i), its carbon intensity is negligible compared to other less widespread processes. It is worth mentioning that the ranking shown in **Figure 1.4** is consistent with data published in 2010 (IEA *et al.*, 2013), which are still the most recent ones (The Royal Society, 2020). This accordance mainly relies on the qualitative trend of the annual production ranking, which has been the same for years. Reasonably, the top examined processes (*i.e.* oil, ammonia, olefins, methanol, *etc.*) are expected to retain their position soon, as in the last decades. It is worth noting that the present days coincide with the so-called energy transition age (the Paris Agreement dates to 2016). Accordingly, this assessment may epitomize a pre/early-transition benchmark to discuss and implement future trends and policies.

1.4. Conclusions

This chapter reviewed anthropogenic greenhouse gas emissions by adopting a general approach. By considering the so-called indirect emissions (*i.e.* the ones generated from electricity and fuel consumption), *Industry* is the first GHG emitter (totaling 31% of GHG global emissions). *Industry* and *Buildings* are the primary users of both heat and electric power. Within *Industry*, chemical manufacturing and oil refining are the main CO_2 emitters, contributing to 9.5% of GHG worldwide emissions. Furthermore, this chapter lists the most carbon-intensive processes of the chemical sector. Specifically, their production volumes and gate-to-gate emission factors were analyzed, compared, and discussed. Oil refining, ammonia synthesis, and steam cracking were the most polluting processes of 2020, releasing 1313, 440, and 228 Mt_{CO2eq}/y, respectively. The primary rationale behind this chapter was to provide a reference list and suggest a

methodology that can be updated periodically. Such a methodology may be referred to when dealing with decarbonization policies in the chemical industry. Notably, ranking chemicals in order of GHG emissions allows stakeholders to adopt climate change mitigation policies through suitable priorities.

2 Green hydrogen synthesis

Introductory comment

Before anything else, the shift to green hydrogen in the chemical industry poses a new challenge associated with its production. The correct sizing of the electrolyzer and the renewable park that powers it (*i.e.* process units rather unfamiliar within the chemical engineering domain) is key to minimizing the production costs of green hydrogen and subsequent green chemicals. This chapter summarizes the efforts made to develop a criterion that allows the process engineer to approach such a problem with relative simplicity: it has resulted in a methodology that has the merit of highlighting the trade-off between the size of the electrolyzer and the renewable park, while also accounting for the stochasticity that different renewable profiles may present in the same location over the years, to ensure a design as robust as possible.

The present chapter stems from:

Green Hydrogen Production from Solar-powered Electrolysis: A Novel Optimization Methodology

Isella, A., & Manca, D.

Computer Aided Chemical Engineering, 2024, 53, 2365–2370

DOI: https://doi.org/10.1016/B978-0-443-28824-1.50395-1

Abstract

Today, hydrogen production still relies primarily on fossil fuels. Indeed, over 99% of the hydrogen produced in 2022 was synthesized via highly carbon-intensive routes, such as steam methane reforming and coal gasification (IEA, 2023). This represents a primary problem in the chemical engineering scenario, as hydrogen is the raw material of most commodities produced in tremendous amounts yearly. Thus, hydrogen production accounts for most carbon dioxide emissions within the chemical industry, alongside oil refining (Isella & Manca, 2022). From this perspective, being ever closer to entering a fully green economy, renewable-powered water electrolysis is an increasingly valid option for producing hydrogen. However, properly sizing the renewable power plant (*e.g.*, a solar or wind farm) and the electrolyzer may be challenging since many features should be considered. Facilitating such a task is the main aim of this chapter, which proposes a novel methodology to design optimal green hydrogen production facilities. Specifically, starting from renewable energy availability time profiles in the location of interest, this criterion allows for the optimal evaluation of the installed capacities of both renewable power plant and electrolyzer, minimizing the plant's total costs (*i.e.* its capital and operating expenditures).

2.1. Introduction

In 2022, about 95 Mt/y of hydrogen were produced globally. Like the previous year, low-emission hydrogen was less than 1% and almost entirely based on conventional fossil routes combined with carbon capture, storage, and utilization (CCUS) technologies. Instead, water electrolysis accounts for just 0.1% of hydrogen production worldwide (IEA, 2023); however, installed capacity and industrial facilities are rapidly increasing. That is the case of the REPowerEU Plan by the European Commission, which set the objective to deliver 65 GW of electrolysis capacity in Europe by 2030, plus 41 GW of wind and 62 GW of solar in additional capacity for the related renewable electricity supply (European Commission, 2022). Indeed, producing hydrogen through renewable-powered electrolyzers is the only available-to-date synthetic pathway allowing total hydrogen production decoupling from fossil feedstocks. This allows for eliminating at the same time both upstream Scope 3 (*i.e.* corporate value chain) emissions associated with fossil fuel extraction and all Scope 1 (*i.e.* direct) and 2 (*i.e.* indirect) emissions, given that renewable sources and electricity are used for meeting the energy demand of the whole process (MPP, 2022). The primary drawback of entirely renewable-based (*i.e.* "green") processes, however, relies upon their complete dependence on renewable power generation (such as solar, wind, hydropower, *etc.*). Indeed, as these energy sources are inherently subject to daily (even hourly) fluctuations and seasonal behavior, they tend to convey such discontinuous trends to the whole process they are connected to. Feeding green (*i.e.* intermittent) electric power to an electrolyzer results in equally intermittent green hydrogen mass

flows generated from such a unit. Moreover, the overall trends provided by renewable energy sources may vary from year to year, causing even more difficulties in properly estimating essential sizes such as the power capacities for the renewable power plant and the electrolyzer. This chapter introduces a new criterion to design green hydrogen production facilities both optimally (*i.e.* providing the installed capacities that minimize the levelized cost of hydrogen, LCOH, or of the final product, LCOX, for a specific location and time horizon) and robustly (*i.e.* providing the installed capacities needed to satisfy the same requirements throughout several years of operation).

2.2. Methodology

The present methodology applies to solar-powered green hydrogen production plants (*i.e.* powered by solar energy only). Accordingly, the battery limits (*i.e.* control volume) of the investigated system is the plant itself, which typically consists of: a solar power plant generating the renewable energy needed for water electrolysis; an electrolyzer converting the electric energy harvested by the solar farm into (green) hydrogen mass flows; and a hydrogen buffer storage providing the hydrogen product to downstream processes/users. Accordingly, to optimally design green hydrogen production plants, the following optimization problem is proposed:

$$\begin{cases} \underset{P_S^{\text{inst}}}{\textbf{Min}}\ \Phi_{\text{OBJ}} = \left(CapEx{+}OpEx\right)_S + \left(CapEx{+}OpEx\right)_E + \left(CapEx{+}OpEx\right)_H & \text{(a)} \\ s.t. & \\ \int_0^{t_{tot}} \dot{E}_E(t)\ dt = \dot{E}_E^{\text{target}} \cdot t_{tot} & \text{(b)} \\ \int_0^{t_{tot}} \dot{m}_{H_2}^{OUT}(t)\ dt = \dot{m}_{H_2}^{\text{target}} \cdot t_{tot} & \text{(c)} \\ \text{with: } \dot{E}_E(t) = \min\left(P_S^{\text{inst}}, \dot{E}_S(t)\right) & \text{(d)} \end{cases} \tag{2.1}$$

Namely, P_S^{inst} and P_E^{inst} are the installed capacities of the solar plant and the electrolyzer, respectively; $\dot{E}_S(t)$ is the instantaneous renewable power generated by the solar plant while $\dot{E}_E(t)$ is the instantaneous power consumed by the electrolyzer, that corresponds to the electricity generated by the solar plant but is bounded above by the nominal capacity of the electrolyzer itself; $\dot{m}_{H_2}^{\text{target}}$ and $\dot{E}_E^{\text{target}}$ are the target green hydrogen production rate and the electric power required by the electrolyzer to generate it, respectively; $\dot{m}_{H_2}^{OUT}$ is the green hydrogen mass flow withdrawn from the storage for downstream utilization, and t_{tot} is the total timespan covered by the optimization procedure (*e.g.*, one year). Finally, $\left(CapEx{+}OpEx\right)_S$, $\left(CapEx{+}OpEx\right)_E$, and $\left(CapEx{+}OpEx\right)_H$ are the capital and operating costs of the solar plant, the electrolyzer,

and the hydrogen storage system, respectively, whose sum constitutes the objective function to minimize.

Few input data are needed: namely, the power generation solar profiles from the location of interest (and the installed capacity of such a reference dataset), and techno-economic data regarding the costs (*i.e.* CapEx and OpEx) and the operating requirements of solar plants, electrolyzers, and hydrogen storage systems to be installed. To solve the optimization problem, one may simply consider a grid search minimization within an arbitrarily defined investigation domain of solar plant installed capacities (*i.e.* ranging from the minimum to the maximum installed capacity values specified by the user) and according to the physical limit of non-negative installed capacities. More in detail, for each point of the grid (*i.e.* for each different configuration of solar plant installed capacity): (i) the corresponding power generation profile is estimated by scaling up/down the reference solar power profiles to the actual solar plant installed capacity; (ii) the corresponding electrolyzer size is estimated through Eq. (2.1b) and, if no solution is found, it means that the solar plant installed capacity of such a configuration cannot produce the sufficient amount of electric energy required by the electrolyzer to meet the target specifications (*i.e.* it falls into the unfeasibility region and must be discarded); (iii) the power consumption profile of the electrolyzer is then estimated through Eq. (2.1d); (iv) the green hydrogen profile originating from the electrolyzer is evaluated from the electrolyzer consumption profile and its operating specifications given as input data; (v) The green hydrogen storage size and its outlet mass flow profile are estimated according to Eq. (2.1c); and (vi) the CapEx and OpEx of the corresponding solar plant, electrolyzer, and hydrogen storage are estimated. Precisely, for each process unit, such costs are evaluated by multiplying the intensive input costs data (*e.g.*, CapEx and OpEx per MW installed, or per t_{H2} stored) by the computed sizes. At the end of the whole procedure, once every single solar plant installed capacity scenario has been assessed, the optimal configuration is the one satisfying Eq. (2.1a), *i.e.* resulting in the lowest total costs.

2.3. Case study

This section validates the presented methodology through a feasibility study of a green hydrogen production plant in California, USA.

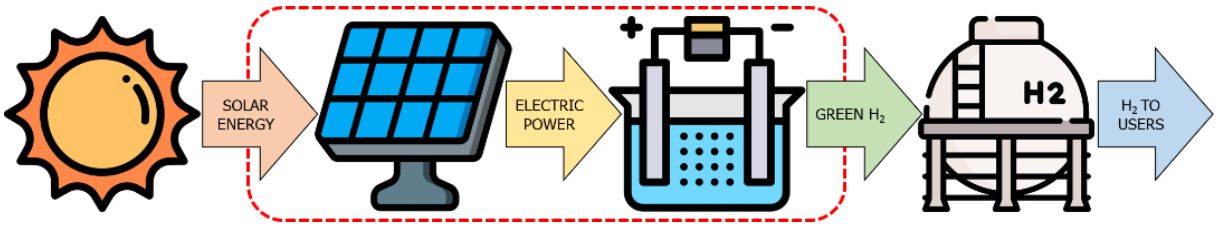

Figure 2.1: System and control volume of the assessed solar-powered green hydrogen production plant.

As we want to estimate the lowest LCOH attainable with our criterion, we consider the system depicted in **Figure 2.1**, which refers to the green hydrogen generation section and neglects any further downstream utilization feature (that is why no hydrogen storage has been included neither in the system nor in the objective function, as its operation completely depends on the user's requirements). Specifically, an average yearly target production rate equal to 1 t_{H2}/h is assumed, and Californian solar hourly profiles from 2022 (CAISO, 2024) are considered as input data. Furthermore, **Table 2.1** reports the reference techno-economic data for the (photovoltaic, PV) solar plant and the (alkaline) electrolyzer.

Table 2.1: Techno-economic assumptions of the assessed solar-powered green hydrogen production plant. From Nel Hydrogen (2021) and DEA (2022).

	Life [y]	CapEx [€2020/MWe]	OpEx [€2020/MWe/y]	Power consumption [kWh/Nm³H2]
Solar plant	20	520,000	9,700	–
Electrolyzer	10	700,000	2% [CapEx/y]	4.5

Thus, we apply the optimization procedure described by Eq. (2.1) by implementing it on MATLAB™ R2022a and selecting an investigation region ranging from $P_{PV}^{\min} = 0$ MW to $P_{PV}^{\max} = 300$ MW. Moreover, to directly estimate the LCOH values corresponding to each solar installed capacity, the objective function (*i.e.* Eq. (2.1a)) is divided by the target hydrogen production rate. Panels A and B of **Figure 2.2** show the assessment's results.

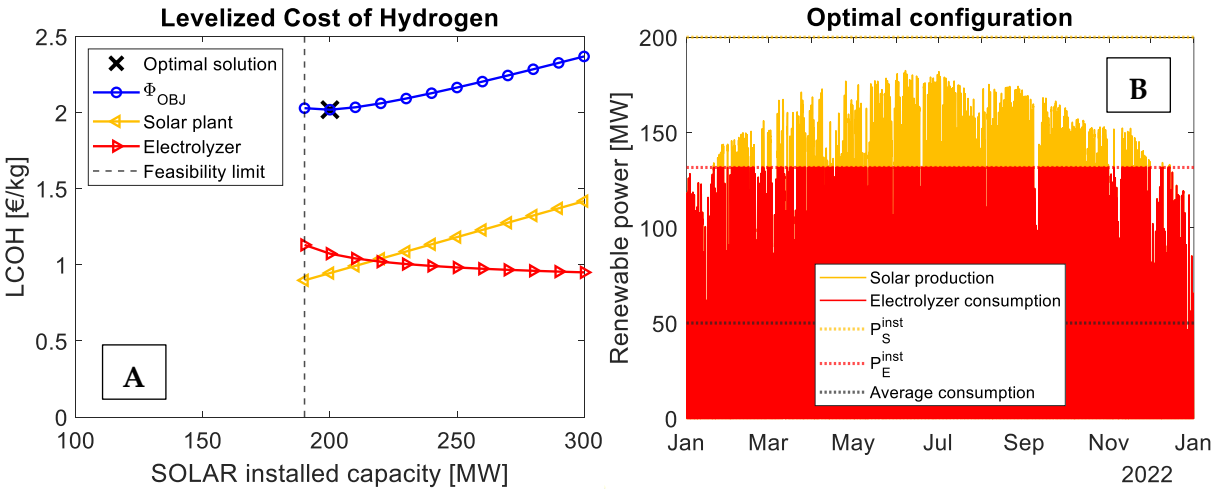

Figure 2.2: (Panel A) Objective function's topology. (Panel B) The optimal configuration.

Focusing on Panel A, the objective function predictably interrupts way before $P_{PV}^{\min}$ (*i.e.* 0 MW), as too small installed capacities of the solar plant cannot produce the sufficient amount of electric energy required by the electrolyzer to meet the 1 t_{H2}/h yearly average production rate specification (see step (ii) in the previous section): precisely, 190 MW is the smallest feasible solar plant installed capacity. However, that is not the

optimal point as smaller solar plants typically call for bigger electrolyzers. Indeed, when producing less renewable energy, the electrolyzer must be oversized to consume its highest possible fraction. Such a trade-off leads to an optimal configuration corresponding to a solar plant installed capacity of 200 MW, which calls for an electrolyzer installed capacity equal to 131.67 MW and ensures an LCOH of 2.02 €/kg, *i.e.* the cheapest one. By focusing on Panel B, instead, the effect of Eq. (2.1b) within the optimization routine becomes evident. Indeed, the winning configuration shows an average electrolyzer consumption rate equal to 50.06 MW (*i.e.* P_{EL}^{target}), that is (considering the power consumption specification of the electrolyzer as reported in **Table 2.1**) the required electric power input for a production rate of 1 t_{H2}/h. Interestingly, such an optimal configuration calls for an electrolyzer sized to fully accommodate the solar production profiles in the off-season (*i.e.* winter) while curtailing the high-season (*i.e.* summer) production peaks.

2.4. Sensitivity analysis

To give more robustness to the results reported in the preceding section, the same case study was assessed by also considering Californian solar hourly profiles from the previous 4 years (*i.e.* since 2018). By doing so, the proposed optimization methodology gives the optimal values for each investigated year, allowing the user to compare them and evaluate how the final installed capacities should change from year to year to minimize the overall production costs. Indeed, due to the high variability that characterizes renewable power generation, the design of renewable-based plants strongly reflects (and suffers from) such undesirable behavior. As an example, the capacity factor of renewable power plants (CF, *i.e.* the dimensionless ratio of the actual electrical energy output over a certain time to the electrical energy output if theoretically operating at full capacity over the same period) might change considerably over the years. However, it is reasonable to expect oscillating values around the characteristic one according to the geographical location.

Figure 2.3 shows the results of such a 5-year assessment: precisely, Panel A displays the topology of the multiple objective functions concerning both solar plant and electrolyzer installed capacities; Panel B focuses on the trade-off between the required solar plant and electrolyzer installed capacities; and Panel C highlights the objective function dependence on the solar plant installed capacity (analogously to Panel A of **Figure 2.2**). As expected, the variability of the input solar power profiles impacts the optimal results, and this can be partially verified by the different capacity factors associated with each investigated year. Indeed, they are an index of how much renewable power has been harvested over a certain time frame but do not give any information concerning the distribution of the power production throughout that period. Indeed, the optimal solar plant installed capacity is 200 MW for 2018, 2021, and 2022 but rises to 210 MW for 2019 and 2020. Analogously, different electrolyzer installed capacities have been obtained: 137.11 MW in 2018; 137.52 MW in 2019;

135.21 MW in 2020; 136.04 MW in 2021; and 131.67 MW in 2022. This implies that a lower-than-average solar power availability occurred in 2019 and 2020 (as it could also be inferred *a priori* from their respective capacity factors, which are the smallest ones provided). Therefore, higher installed solar plant capacities are needed to meet the specified production requirements.

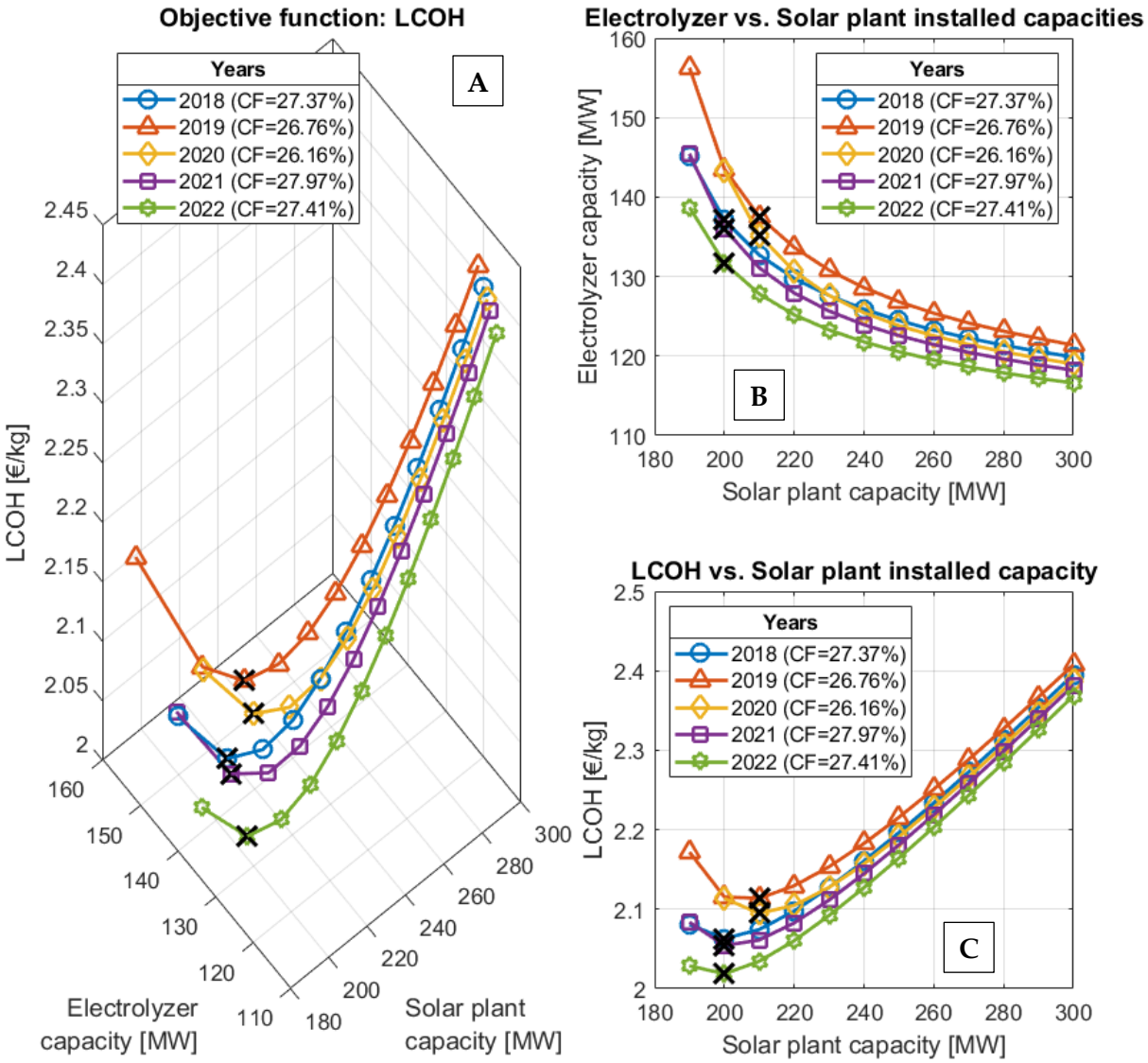

Figure 2.3: (Panel A) Objective function profiles resulting from the 2018-to-2022 assessment (the corresponding yearly solar capacity factors are reported within the legend); (Panel B) Investigated solar plant installed capacities and corresponding electrolyzer installed capacities; (Panel C) Objective function dependence on solar plant installed capacities. Black crosses mark the minimum points, *i.e.* the economically optimal configuration for each year.

2.5. Conclusions

By entering the so-called "green economy", the manufacturing sector increasingly pushes for decarbonization. Green hydrogen might then represent the key raw

material for many processes that currently depend heavily on fossil fuels in procuring hydrogen feedstocks. This chapter presented a novel methodology to design green hydrogen production facilities both optimally (*i.e.* providing the installed capacities that currently minimize the levelized cost of hydrogen or other downstream chemicals, if any) and robustly (*i.e.* providing the optimal results referring to multiple years of operation). It requires just a few input data: *i.e.* the input solar power profiles from the location of interest and the techno-economic data (such as the costs and the operating variables) of the main process units to be installed (namely, the solar plant and the electrolyzer). In this regard, a case study was assessed, first considering a 1-year time frame and then a 5-year one. By doing so, more conservative estimations for the installed capacity requirements for the solar plant and the electrolyzer were made possible, as the methodology considered each year's different solar power availability.

3 Hybrid-green ammonia synthesis

Introductory comment

Before diving into "fully-green" process configurations, a compromise solution was investigated: "hybrid-green" ammonia synthesis, *i.e.* producing ammonia partly from fossil hydrogen (*i.e.* via steam reforming) and partly from green hydrogen (*i.e.* via water electrolysis). Inspired by the industrial partner of the doctoral program (Casale SA, Switzerland), this study resulted in the first techno-economic assessment of hybrid ammonia plants ever documented in the scientific literature. Furthermore, this was also the first case study underlining the importance of process flexibility, which chemical plants must necessarily feature to be powered by renewable sources while keeping reasonable production costs. Specifically, such considerations led to an in-depth analysis of material and energy storage systems to support flexible operations.

The present chapter stems from:

Towards the decarbonization of ammonia synthesis – A techno-economic assessment of hybrid-green process alternatives

Isella, A., Ostuni, R., & Manca, D.

Chemical Engineering Journal, 2024, 486, 150132

DOI: https://doi.org/10.1016/j.cej.2024.150132

Abstract

This chapter analyzes the retrofitting of a conventional "gray" ammonia plant for its partial decarbonization. Specifically, such retrofitting involves the hybridization of the process by providing a certain amount of green hydrogen (*i.e.* by water electrolysis) for the ammonia synthesis to reduce the demand for the original gray hydrogen route (*i.e.* by fossil-based steam reforming) and consequently reduce CO_2 emissions. As the green hydrogen is produced through an electrolyzer that consumes renewable electric energy, two design configurations are considered: (*Option I*) the supply of clean electricity from renewable sources; (*Option II*) the generation of clean electricity by an in-house photovoltaic power plant. Once having analyzed the advantages and limitations of the hybrid plant layouts, the ammonia production costs achieved by the three simulated plants (*i.e.* the reference "gray" plant and the two hybrid alternatives) are estimated by considering the United States (USA) and European Union (EU) market quotations in 2022 and previsions for 2030 and 2050. The main outcomes are that (i) hybrid-green ammonia proves to be a feasible, environmentally friendly retrofitting option for the ammonia production industry, showing production costs that are no more than 36% higher than gray ammonia; and (ii) *Option I* achieves better cost-effectiveness than *Option II* in the USA, while the opposite happens in the EU. Specifically, the resulting 10%-green-on-average hybrid-green ammonia production costs range between +0.3% (*EU-2022*) and +30.8% (*USA-2022*) for *Option I*, and between −1.3% (*EU-2022*) and +35.3% (*USA-2022*) for *Option II*, compared to the reference gray ammonia plant. (iii) Lastly, the projected (*i.e.* in 2030 and 2050) CO_2 avoidance costs associated with hybrid-green ammonia configurations exceed 400 USD/t_{CO2} in the USA and 500 USD/t_{CO2} in the EU.

3.1. Introduction

The decarbonization of ammonia production is a drive that today rises more urgently than ever. In terms of environmental sustainability, ammonia is by far the most carbon-intensive chemical commodity. Specifically, ammonia synthesis was responsible for the generation of approximately 440 Mt/y of CO_2-equivalent emissions in 2020 (Isella & Manca, 2022), which accounted for almost 1% of anthropogenic global greenhouse gas (GHG) emissions of that year (Rivera *et al.*, 2021). The link between GHG emissions and ammonia stems primarily from the hydrogen feedstock to the ammonia synthesis, which is still about 98% derived from fossil fuels: natural gas, 72%; coal, 22%; and crude oil, 4% (Bicer *et al.*, 2016). These can be defined as the "process emissions", representing about 70% of the CO_2 emissions of a conventional ammonia plant. The remaining ca. 30% is associated with the "energy emissions", *i.e.* the ones related to generating the heat and compression required for the process (Isella *et al.*, 2023). Back to the process emissions, it stands clear that the main road to achieving full carbon neutrality in ammonia production is to decouple the whole synthesis route from fossil

feedstocks. This is the basic idea behind the "green ammonia" technologies, which aim to retrofit and finally replace the "gray", fossil-based hydrogen feedstock with a "green", water-based one thanks to renewable-energy-powered electrolyzers. This challenging decarbonization strategy is supposed to represent the endgame of future ammonia production since it stands out as the only zero-emissions technology expected to be economically practicable and technologically established within the next decade (MPP, 2022). Nonetheless, till such zero-emissions technologies become commercially ready for large-scale production in the following decades, an available-to-date alternative such as hybrid-green ammonia is an appealing production pathway. Precisely, "hybrid-green ammonia" consists of retrofitting a conventional gray ammonia plant by adding a parallel line to produce water-based, green hydrogen. By doing so, a certain amount of the hydrogen needed as a reactant in the Haber-Bosch section (*i.e.* the one where hydrogen reacts with nitrogen to produce ammonia) of the hybridized ammonia plant is completely carbon-neutral, resulting in lower CO_2 emissions. In this regard, partial decarbonization of large gray plants can lead to substantial environmental benefits (fitting currently available renewable and electrolyzer capacities) while valorizing existing expensive assets.

The primary rationale of this study is to perform a techno-economic assessment of a hybrid-green ammonia plant to analyze its economic feasibility and determine the best operating conditions. Indeed, to our knowledge, no works have been published yet on this novel technique that might gain increasing importance in the following years as the decarbonization pathway becomes widespread.

3.2. Gray ammonia plant and hybridization challenges

3.2.1. The route to hybridization

Before starting with the techno-economic assessment of the hybrid-green ammonia plant, a conventional, natural gas-based 2000 t_{NH3}/d ammonia plant was simulated in UniSim® Design R491 as the reference plant (**Figure 3.1** shows its block flow diagram); this enabled us to estimate the CO_2 emissions generated by the classic gray layout for benchmarking. Consequently, the hybrid retrofitting of such a plant (to partially abate the CO_2 emissions without affecting its production capacity) would only consist of placing a renewable-energy-powered electrolyzer side by side with the conventional "Front-end" section (*i.e.* the reforming, shift, and syngas purification units), right before the Haber-Bosch process (*aka* the "Synthesis loop", or "Synloop", that is the main section of the so-called "Back-end"). Indeed, being the electrolyzer a unit aimed at producing green hydrogen from renewable electric energy sources, such a process solution allows for a significant decrease in the amount of gray hydrogen. Indeed, gray hydrogen consumes fossil fuels twice (i) as a feedstock for its synthesis by steam reforming (*i.e.* the natural gas feedstock headed to the reformers) and (ii) as a utility for the thermal energy supply (*i.e.* the fuel gas headed to the burners of the primary

reformer furnace). Consequently, a gray ammonia plant involves both process- and energy-related CO_2 emissions, which can be lessened by suitable green retrofitting.

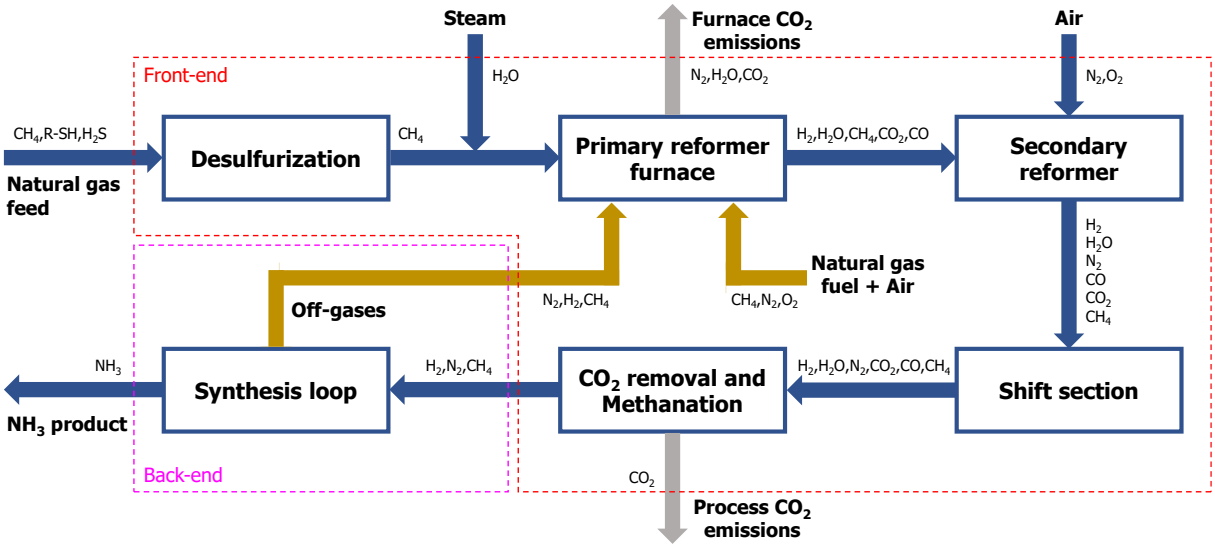

Figure 3.1: Block flow diagram of the reference conventional, natural gas-based (gray) ammonia plant (2000 t_{NH3}/d capacity).

Nevertheless, one of the primary efforts for the best design of such a process is the choice of the optimal decarbonization extent of the hybrid plant: in other words, how much green hydrogen should enter the Haber-Bosch section instead of gray hydrogen. It should be kept in mind that such a key variable is tied to some issues:

1. Availability of renewable power.
2. Operating conditions variation from the nominal ones (*i.e.* those of the gray plant):
    a. The process flow entering the primary reformer (*i.e.* the "throughput").
    b. The operating temperature within the secondary reformer.
    c. The amount of fuel gas fed to the burners of the primary reformer furnace.

The following paragraphs analyze the reasons behind these constraints with greater accuracy.

3.2.2. Hybridization constraints on the availability of renewable power

Starting from the first point of the list above, the electrolyzer should be fed with electrical energy from renewables to ensure fully green operations. This means that the whole green section merged with the original plant is strongly subjected to the fluctuating trends of renewable energy profiles. Indeed, renewable energy production is inherently characterized by the irregular availability of energy sources (*e.g.*, sunlight and/or wind in the case of solar and/or wind farms). This means that, in a certain way,

the electrolyzer will simply transform such intermittent renewable energy profiles into correspondingly intermittent green hydrogen flows. It follows that the target green hydrogen productivity (or, correspondingly, the target decarbonization extent) should be considered as an average of the fluctuations that span from a minimum of zero (when no clean electricity is available) to a maximum, which is strictly related to the capacity factor of the renewable power plant (that provides the peak electric power made available to the final user) as well as few essential design considerations (that were already mentioned in the previous list and will be discussed in depth in the following). Therefore, a storage system is mandatory to mitigate such fluctuations' impact on the rest of the retrofitted plant. This system can be either a hydrogen storage section downstream of the electrolyzer or a battery energy storage system (BESS) amidst the renewable power plant and the electrolyzer.

3.2.3. Hybridization constraints on the operating conditions of the plant

Regarding the second point of the aforementioned list (*i.e.* operating conditions as close as possible to the nominal ones), it is quite reasonable that the partial replacement of gray, fossil-based, hydrogen with green, water-based, hydrogen has several effects on the retrofitted plant, especially if one considers that it was originally designed to be fed with natural gas only. The first obvious effect of hybridization is that the lower demand for gray hydrogen (being partially replaced by the green hydrogen from the electrolyzer) calls for a lower amount of natural gas as feedstock. While this undoubtedly grants lower CO_2 emissions, the main drawback is the drop in mass flows circulating across the front-end section, specifically in the primary reformer (see point 2a of Paragraph 3.2.1). Indeed, a conventional steam reformer cannot operate properly when the throughput decreases too much below the design capacity (our assumption was to set the lower bound to 80% of the nominal capacity (de Jong *et al.*, 2009)). Moreover, such drops in the material flows of the "gray route" might also affect the secondary reformer, specifically its operating temperature (see point 2b). Indeed, since the inlet air flow must be kept constant to meet the nitrogen demand of the plant and guarantee the stoichiometric hydrogen-to-nitrogen ratio for the ammonia converter, the oxygen-to-carbon molar ratio at the secondary reformer inlet increases promptly, and the temperature of the reactor does the same. Such a temperature rise must be as limited as possible (our assumption was to consider +100 °C as the maximum allowed temperature increase within the reactor) to prevent the overheating of the secondary reformer and the downstream process boiler. Finally, the amount of fuel gas fed to the furnace burners (see point 2c) represents a process variable that should not vary significantly from the original operating conditions. However, in this specific case, this is not a substantial risk for the hybrid plant: indeed, as the secondary reformer tends to reach higher temperatures, the equilibrium of the endothermic steam reforming reaction is further shifted forward, which decreases the presence of methane in the outlet products. Consequently, the inert content in the ammonia synthesis loop is expected to drop and, as a result, the methane content in the off-gases to be burnt in

the furnace is lower when compared to the original gray operating conditions, making still compulsory (although necessarily smaller than in the gray plant) the demand for fuel gas. It is also worth bearing in mind that this last issue, *i.e.* the drop in the inert gases heading to the Haber-Bosch section, turns out to be beneficial to the economy of the process as it reduces the compression costs and improves the reaction thermodynamics and kinetics in the ammonia converters.

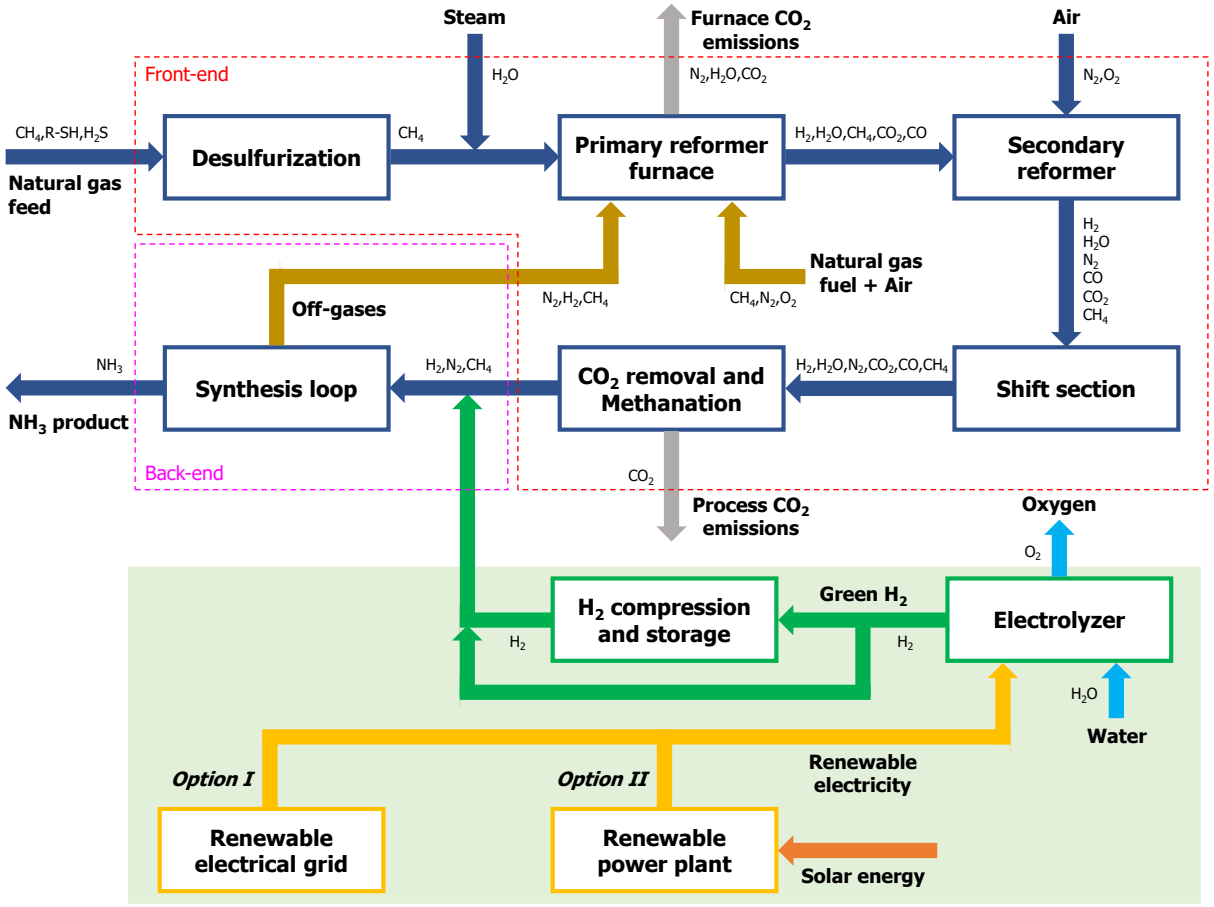

Figure 3.2: The simulated and assessed hybrid-green ammonia plant (2000 t_{NH3}/d capacity). The green rectangle contains all the additional units (whose operation is "green") introduced by the retrofit.

3.3. Process simulation of the hybrid plant

As shown in **Figure 3.2**, the retrofitted ammonia plant calls for a parallel line of hydrogen production using a renewable-energy-powered electrolyzer which should be connected to an electrical power supply (*e.g.*, the electrical network or a dedicated power plant) and followed by a hydrogen storage system (indeed, this design option was preferred to the BESS solution due to its lower cost and higher technology readiness level).

As previously discussed, one of the main efforts for the best design of such a plant is the choice of the optimal decarbonization extent of the hybrid plant, *i.e.* the amount of green hydrogen injected into the Haber-Bosch section instead of gray hydrogen. In this regard, simulating the hybrid plant with increasing contributions of green hydrogen, a nearly identical relation among the ratio of green hydrogen over the total hydrogen entering the synthesis loop (the "green-to-gray hydrogen ratio", G2GHR), the percentage of overall (*i.e.* both process and furnace emissions) decarbonization extent of the hybrid plant ($deCO_2$), and the percentage of throughput decrease in the primary reformer (DR1) arises (see **Figure 3.3**).

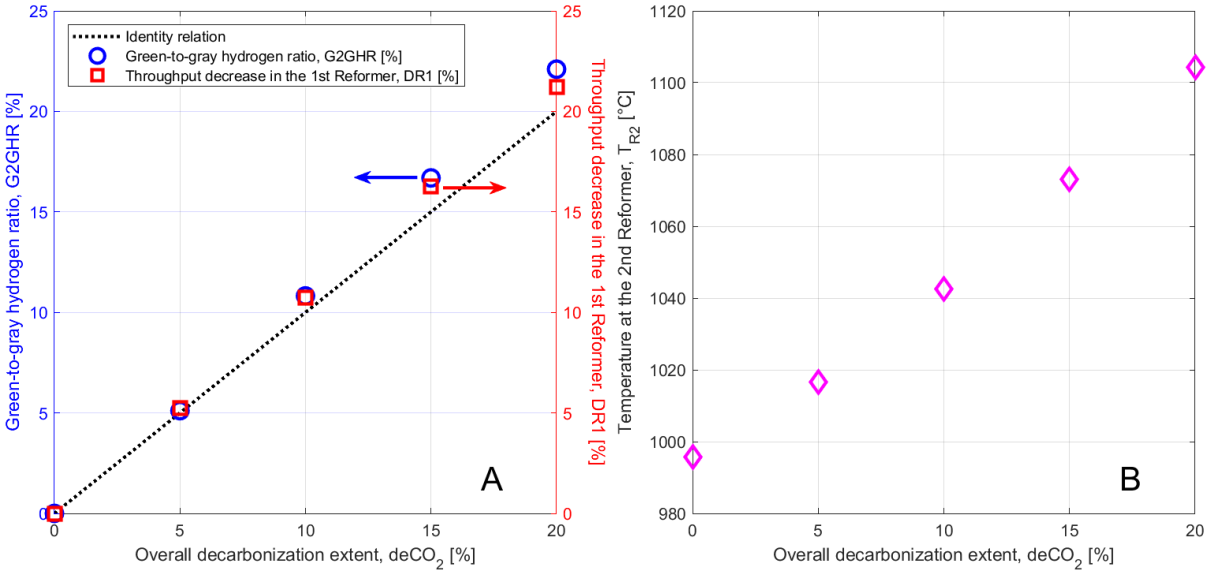

Figure 3.3: The effect of increasing the $deCO_2$ extent on the constraints of the hybrid plant. Panel A, the nearly identical relation between G2GHR and DR1. Panel B, the rise in operating temperature within the secondary reformer.

Panels A and B of **Figure 3.3** show how $deCO_2$ cannot exceed a certain value so as not to overtake the operating boundaries discussed in Paragraph 3.2.3. Specifically, $deCO_2$ should be lower than 20% at the highest to not deplete the primary reformer throughput by more than 20% (following the nearly identical relation shown in Panel A of **Figure 3.3**) and not exceed the maximum allowable temperature rise at the secondary reformer (Panel B of **Figure 3.3**). On the contrary, the constraint on the fuel gas flow does not limit the investigated range, due to the nature of the retrofitting itself. Considering the fluctuating renewable energy trends (as discussed in Paragraph 3.2.2), a reasonable average $deCO_2$ value of 10% is assumed, which indeed falls exactly in the middle of the 0% to 20% allowable range (*i.e.* from the case of no green power/hydrogen availability to the case of maximum green hydrogen input acceptable into the Haber-Bosch section). Specifically, **Table 3.1** reports the main process variables of such three key plant configurations, *i.e.* the hybrid plant performances assessed at the lower (0%), average (10%), and upper (20%) values of $deCO_2$.

Table 3.1: Main operating conditions of the hybrid-green ammonia plant investigated. Each column refers to a different plant configuration and reports the actual process variable values on the left, while their ratio to the corresponding *Lower bound* (*i.e.* the reference plant) ones on the right (in italics).

Process variable [unit]		**Lower bound** ($deCO_2$ = 0%)		**Average** ($deCO_2$ = 10%)		**Upper bound** ($deCO_2$ = 20%)	
Green hydrogen to the synloop	[t/h]	0		1.74		3.55	
Primary reformer throughput	[t/h]	163	*100%*	146	*89.3%*	129	*78.8%*
Natural gas feed to the front-end	[t/h]	38.0	*100%*	33.9	*89.3%*	29.9	*78.8%*
Natural gas fuel to the furnace	[t/h]	12.9	*100%*	11.9	*92.3%*	10.7	*82.8%*
Furnace CO_2 emissions	[t/h] [t_{CO2}/t_{NH3}]	38.9 0.467	*100%*	34.8 0.418	*89.5%*	30.7 0.368	*78.8%*
Process CO_2 emissions	[t/h] [t_{CO2}/t_{NH3}]	97.4 1.17	*100%*	87.9 1.06	*90.3%*	78.1 0.937	*80.1%*
Total CO_2 emissions	[t/h] [t_{CO2}/t_{NH3}]	136.3 1.64	*100%*	122.7 1.48	*90.0%*	108.8 1.31	*79.8%*

Section 3.4 assesses the proper design of the electrolyzer, the renewable power plant, and the hydrogen storage to guarantee the requirements of the average configuration continuously.

3.4. Techno-economic assessment of the retrofitting

3.4.1. CapEx and OpEx estimation of the electrolyzer

Disregarding for the moment the installed capacity of the electrolyzer (as it will be discussed in Paragraph 3.4.4), the following data and conservative hypotheses were considered for its techno-economic assessment:

- An alkaline electrolyzer was examined. Different electrolyzer technologies are commercially available: alkaline (AWE) and proton exchange membrane (PEM) electrolyzers are the most widespread. More recently, solid oxide (SOE) and anion exchange membrane (AEM) electrolyzers have been developed, but both are still far from reaching market availability (David *et al.*, 2019). Here, an AWE was preferred to a PEM since the former is still maintaining a market-leading position in the sector (particularly, due to its long tradition) and because, despite its higher inertia due to the greater liquid hold-up, it shows sufficiently higher flexibility for its integration into ammonia plants. Indeed, an AWE-type electrolyzer is much more flexible than the ammonia plant in terms of load ramps and turndown ratio. Specifically, the electrolyzer is here assumed to show perfectly flexible behavior, as characteristic AWE maximal ramping rates of ±20%/s are sufficiently rapid to match solar energy variations in renewable power production (Armijo & Philibert, 2020). Moreover, although achieving a higher current density, a greater operating range, and a higher hydrogen purity, PEM electrolyzers are nevertheless more expensive and less durable. That said, the performances of the AWE unit are inferred from Nel Hydrogen (Nel Hydrogen, 2023), a global company that provides solutions for producing, storing, and distributing hydrogen from renewable energy sources. Specifically, the electrolyzer shows a nominal electricity consumption of 4.5 kWh/Nm^3_{H2}, water consumption of 0.9 kg_{H2O}/Nm^3_{H2}, and a hydrogen outlet temperature and pressure of 35 °C and 30 bar, respectively (Nel Hydrogen, 2021). Coupling such operating data with the process simulation results, it turns out that the electric demand of the electrolyzer can be as high as 177 MW_e (*upper bound*), with an *average* value of 87 MW_e. Analogously, the demineralized water demand can be as high as 35.5 t/h (*upper bound*), with an *average* value of 17.4 t/h. Note that the *average* configuration values do not correspond exactly to half of the maximum values due to the aforementioned nearly identical relation among the different deCO_2 configurations.
- The electrolyzer has a lifetime of 10 years and its CapEx amounts to 700 USD/kW_e (Fraunhofer ISE, 2021). This value includes engineering, housing, and balance-of-plant components such as the compression and the water and hydrogen purification units. Such a reference value relies on the pronounced economy of scale affecting AWE modules having an installed power capacity above 100 MW_e.

3.4.2. CapEx and OpEx estimation of the renewable electric power input

Two renewable electrical energy sourcing alternatives are investigated:

I. Buy electricity from a certified renewable power provider, which delivers it through the grid according to a Power Purchase Agreement (PPA) (*Option I* as in **Figure 3.2**).

II. Produce electricity on-site from a photovoltaic (PV) power plant (*Option II* as in **Figure 3.2**).

Both cases show different pros and cons. *Option I* allows the plant to receive a continuous electrical energy input that does not call for any "intermittency-mitigating" features such as supplementary hydrogen storage. Its main drawback, however, is the dependency on the renewable electricity market, which is subjected to strong fluctuations (Isella *et al.*, 2023) and thus can suddenly impose very expensive costs. *Option II* allows the plant to be self-sufficient from an electric energy point of view (*i.e.* all the renewable electrical energy needed for the process is produced on-site by a photovoltaic solar park and is not purchased from external sources). However, it takes over all the previously mentioned problems of renewable hydrogen generation (above all, the intermittency issues) and, obviously, the investment and operating expenditures (and the required space) for the power station and the hydrogen storage.

Regarding *Option I*, the economic assessment of the electric power term simply necessitates as input the market price of clean electricity: *e.g.*, 71.65 EUR/MWh in Europe, January 2023 (Pexapark, 2023).

Conversely, here follow the data and hypotheses assumed for the design of the PV power plant, as required by *Option II* (disregarding, for now, its installed capacity, as it will be discussed in Paragraph 3.4.4):

- The power station has a lifetime of 20 years. This is a conservative hypothesis since the estimated operational lifetime of a present-day photovoltaic module exceeds 30 years (DOE, 2023). Moreover, since both the PV panels and the electrolyzer deal with direct current (DC), no solar inverters are required. Instead, only DC/DC converters are needed for voltage conditioning (Guilbert *et al.*, 2017).
- The CapEx and OpEx techno-economic assumptions related to the PV power plant modules and units come from IRENA (2023) and are reported in **Table 3.2**.

3.4.3. CapEx and OpEx estimation of the hydrogen storage

As discussed in the previous paragraph, *Option II* calls for hydrogen storage after the electrolyzer to deal with the intermittency and seasonality of the solar power input and to avoid inlet green hydrogen amounts above the deCO_2=20% threshold.

The data and hypotheses assumed for the hydrogen storage section are as follows:

- The hydrogen storage system has a lifetime of 10 years and mainly consists of a compressor and multiple Type I pressurized tanks (*i.e.* hydrogen storage vessels commonly used for stationary applications (Mucci *et al.*, 2023a)) operating at 200 bar.

- The CapEx and OpEx techno-economic assumptions related to the hydrogen storage section come from DEA (2020) and are reported in **Table 3.3**.

Table 3.2: Techno-economic assumptions for the photovoltaic power station (IRENA, 2023). O&M = Operation & Maintenance.

PV solar: utility-scale, ground-mounted, single-axis tracking panels (USA, 2022)		
Total installed costs	1119	[USD_{2022}/kW_e]
Modules (Hardware Costs)	403.4	[USD_{2022}/kW_e]
Inverters (Hardware Costs)	75.4	[USD_{2022}/kW_e]
Racking and Mounting (Hardware Costs)	84.6	[USD_{2022}/kW_e]
Cabling/Wiring (Hardware Costs)	75.4	[USD_{2022}/kW_e]
Grid Connection (Hardware Costs)	64.4	[USD_{2022}/kW_e]
Safety and Security (Hardware Costs)	25.8	[USD_{2022}/kW_e]
Monitoring and Control (Hardware Costs)	12.9	[USD_{2022}/kW_e]
Mechanical Installation (Installation Costs)	161.9	[USD_{2022}/kW_e]
Electrical Installation (Installation Costs)	23.9	[USD_{2022}/kW_e]
Inspection (Installation Costs)	5.5	[USD_{2022}/kW_e]
Margin (Soft Costs)	115.9	[USD_{2022}/kW_e]
Financing Costs (Soft Costs)	14.7	[USD_{2022}/kW_e]
System Design (Soft Costs)	27.6	[USD_{2022}/kW_e]
Permitting (Soft Costs)	5.5	[USD_{2022}/kW_e]
Incentive application (Soft Costs)	17.6	[USD_{2022}/kW_e]
Customer acquisition (Soft Costs)	4.5	[USD_{2022}/kW_e]
Total O&M costs	9.1	[$USD_{2022}/kW_e/y$]

Table 3.3: Techno-economic assumptions for the hydrogen storage system (DEA, 2020). A conversion factor of 0.95 EUR/USD (IEA, 2023), *i.e.* the 2022 annual average, has been used. O&M = Operation & Maintenance.

Pressurized hydrogen gas storage system (Compressor & Type I tanks at 200 bar)		
Gravimetric energy density	33.3	[kWh/kg]
Specific investment	0.060	[$MUSD_{2022}$/MWh]
Compressor component	0.032	[$MUSD_{2022}$/MWh]
Type I tanks component	0.019	[$MUSD_{2022}$/MWh]
Installation, equipment, manhours	0.009	[$MUSD_{2022}$/MWh]
Fixed O&M	630	[USD_{2022}/MW/y]

3.4.4. Power plant, electrolyzer, and hydrogen storage sizing

Option I, since it benefits from continuous renewable electric power input, simply calls for an electrolyzer capacity equal to the upper-bound plant electricity demand (*i.e.* $deCO_2$=20%: 177 MW_e). Conversely, *Option II* calls for an optimization procedure to select the most convenient size of the photovoltaic power plant, the electrolyzer, and the hydrogen storage.

Different photovoltaic installed capacities are investigated and, for each of them, the corresponding electrolyzer installed capacity must guarantee an average power input equal to 87 MW_e (*i.e.* $deCO_2$=10% target): finally, the hydrogen storage size follows by analyzing the hydrogen flow originating from the electrolyzer.

In this regard, we consider a "flexible" hydrogen delivery, *i.e.* showing a hydrogen outlet flow that varies in time, depending on the instantaneous hydrogen inlet flow and hold-up conditions, since a variable hydrogen outlet mass flow guarantees a smaller (and cheaper) design.

Alternatively, one might consider a "rigid" hydrogen delivery, *i.e.* showing a constant outlet flow set equal to the hydrogen consumption by the ammonia synthesis loop at target operating conditions (*i.e.* $deCO_2$=10%: 1.74 t_{H2}/h) of the hybrid plant, regardless of the unsteady inlet contribution equal to the production rate profiles of the electrolyzer. Such a configuration is way easier to design but requires much higher storage volumes, as it does not adapt to the seasonal behavior of renewable energy generation (Armijo & Philibert, 2020).

Accordingly, the whole problem can be summarized by the following optimization procedure:

$$\begin{cases} \underset{P_S^{inst}}{\textbf{Min}}\ \Phi_{\text{OBJ}} = \left(CapEx_y + OpEx\right)_S + \left(CapEx_y + OpEx\right)_E + \left(CapEx_y + OpEx\right)_H \\ s.t. \quad \int_0^{t_{tot}} \min\left(\dot{E}_S(t), P_E^{inst}\right) dt \ = \ \dot{E}_E^{10\%} \cdot t_{tot} \\ \qquad \int_0^{t_{tot}} \dot{m}_{H_2}^{OUT}(t)\ dt \ = \ \dot{m}_{H_2}^{10\%} \cdot t_{tot} \end{cases} \tag{3.1}$$

Where P_S^{inst} and P_E^{inst} are the installed capacities of the PV plant and the electrolyzer, respectively; $\left(CapEx_y + OpEx\right)_S$, $\left(CapEx_y + OpEx\right)_E$, and $\left(CapEx_y + OpEx\right)_H$ are the sum of the annualized capital expenditures and the annual operating expenditures of the PV plant, the electrolyzer, and the hydrogen storage, respectively; t_{tot} is the total timespan considered (a 1-year time frame was assumed); $\dot{E}_S(t)$ is the instantaneous renewable power produced by the photovoltaic power plant (which depends on the total installed capacity of the PV plant itself); $\dot{E}_E^{10\%}$ is the renewable power that the electrolyzer needs to produce $\dot{m}_{H_2}^{10\%}$, *i.e.* the green hydrogen mass flow that should enter the ammonia synthesis loop to reach a $deCO_2$ value equal to 10% (namely, 1.74 t_{H2}/h); and $\dot{m}_{H_2}^{OUT}(t)$ is the instantaneous green hydrogen mass flow withdrawn from the hydrogen storage.

Note that the annualized CapEx (since they must add to the annual OpEx) have been evaluated by the following formula (Aromada *et al.*, 2021):

$$CapEx_y = \frac{CapEx}{\sum_{n=1}^{NY}\left(1+r\right)^{-n}} \tag{3.2}$$

Where NY is the lifetime (in years) and r is the discount rate. In the specific case, a 5% discount rate is considered (Mucci *et al.*, 2023a).

Therefore, we referred to a few Californian solar profiles (for a total of five years, 2018-2022, to provide more robustness to the assessment) and minimized the total costs for each PV, electrolyzer, and hydrogen storage configuration (see **Figure 3.4**).

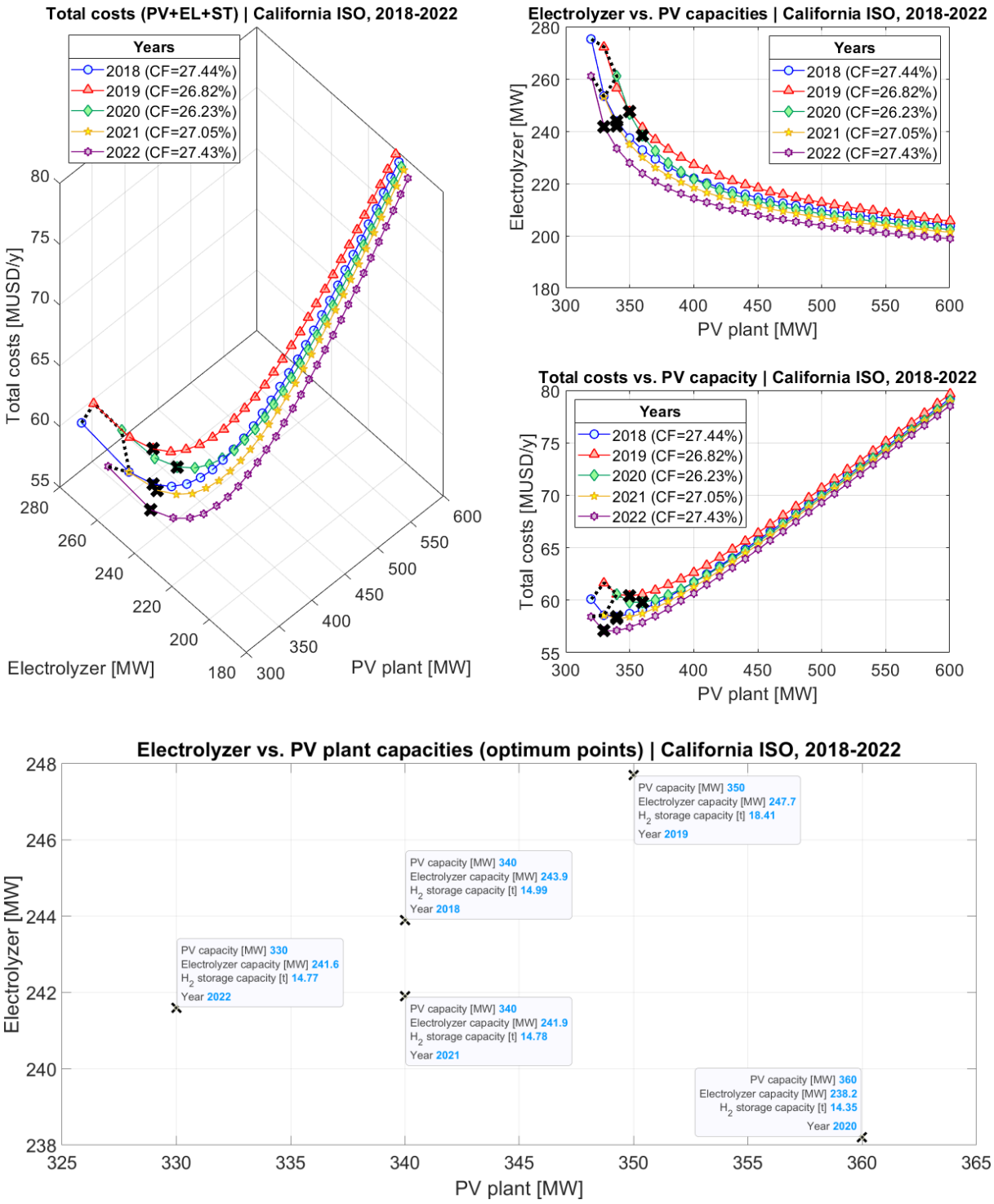

Figure 3.4: Objective function (see Eq. (3.1)) for the optimal sizing of both the photovoltaic power plant and the electrolyzer, based on Californian solar profiles (CAISO, 2024) for the 2018-2022 quinquennium. Each curve presents a PV plant capacity ranging from an upper limit equal to 600 MW_e to a lower limit (*i.e.* the minimum value below which not enough renewable power is produced) that depends on the year assessed (black dotted line). The black bold crosses represent the optimal configurations (*i.e.* minimum points) for each year.

Figure 3.5 provides information regarding how total costs are split between the PV plant, the electrolyzer, and the hydrogen storage (in 2019).

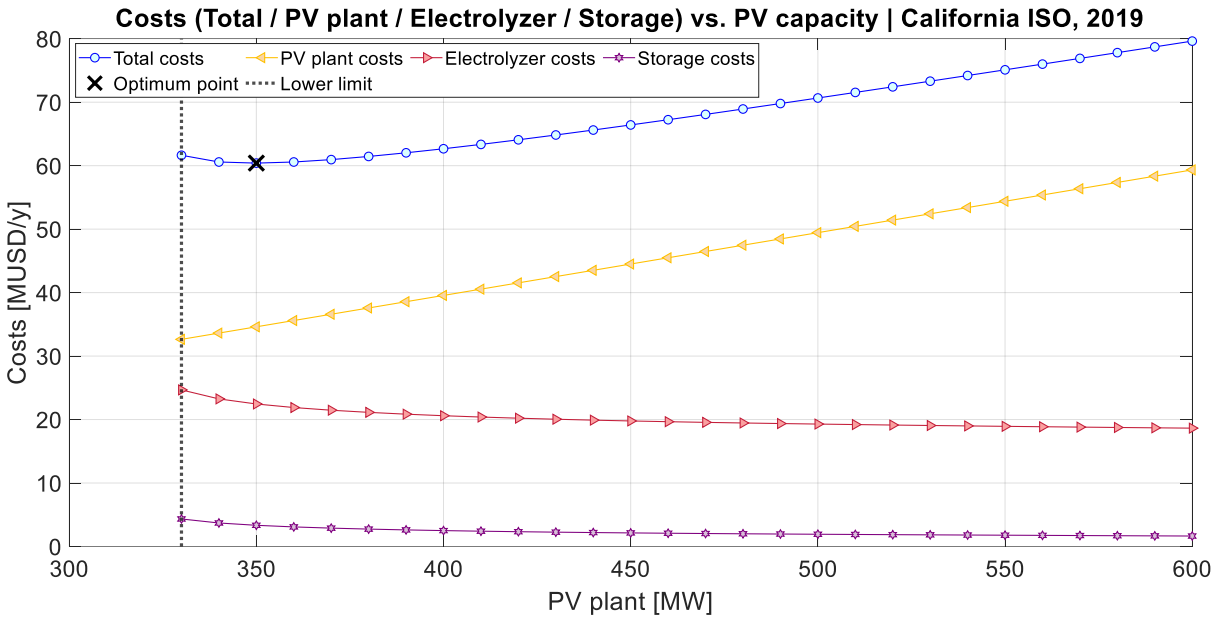

Figure 3.5: Focus on the total costs profile for 2019, showing the contribution of PV plant, electrolyzer, and hydrogen storage expenditures. The black dotted vertical line represents the lower limit for the PV plant installed capacity, while the black cross is the minimum, *aka* optimum, point (*i.e.* 60.4 MUSD/y).

The consistent renewable energy management of the optimal configuration is even more visible in **Figure 3.6** (still referring to the most conservative scenario: *i.e.* the 2019 results, as they provide the highest total costs).

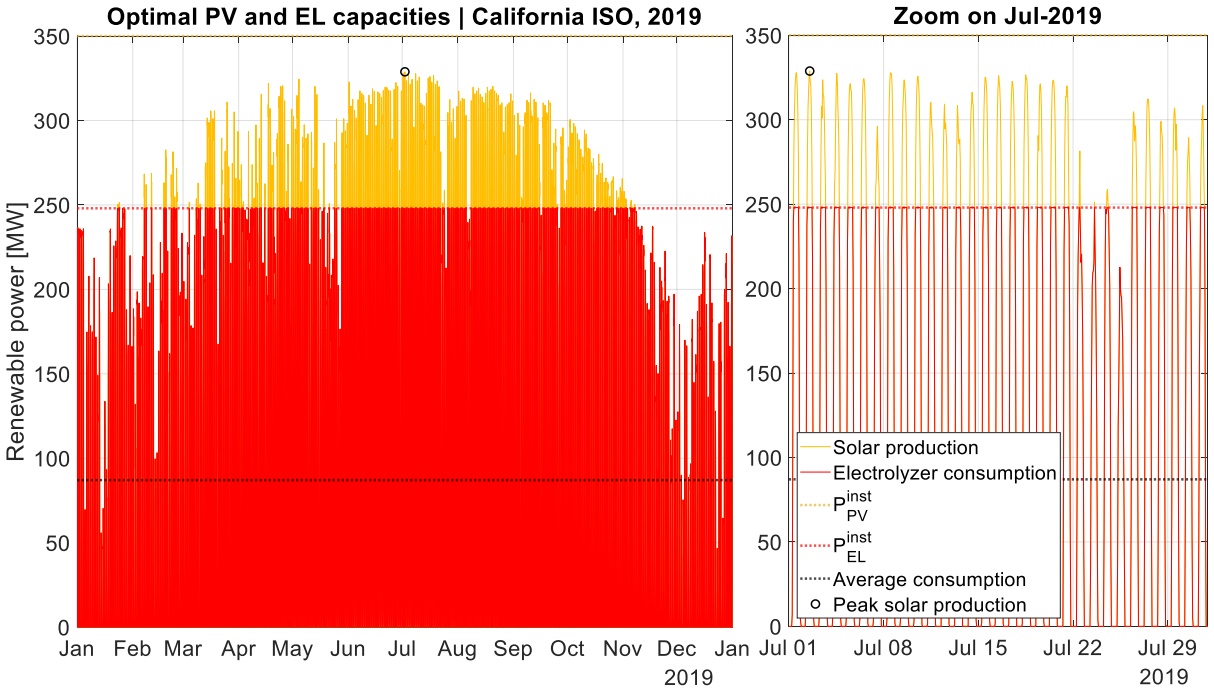

Figure 3.6: Optimal photovoltaic plant and electrolyzer sizing. PV plant capacity of 350 MW_e and electrolyzer installed capacity of 248 MW_e, considering Californian solar profiles in 2019 (CAISO, 2024). Left panel, over the entire 2019 year. Right panel, zoom over July 2019 only.

Indeed, the optimal configuration depicted in **Figure 3.6** guarantees an average renewable power input equal to 87 MW_e (*i.e.* an average $deCO_2$ value equal to 10% throughout the entire operating time) and it accounts for just 7.05% of wasted (*i.e.* overproduced) energy as against the total amount produced by the photovoltaic plant. However, the main drawback of such a configuration is that – due to its oversizing compared with the $deCO_2$=20% boundary's demand (*i.e.* 177 MW_e) – the electrolyzer reaches instantaneous $deCO_2$ values as high as 30.9%. Indeed, considering the electrolyzer specifications listed in Paragraph 3.4.1, an electric power input of 248 MW_e (*i.e.* the optimal installed capacity of the electrolyzer as for 2019) corresponds to a green hydrogen production rate of 4.95 t_{H2}/h. For this reason, an upper limit for the $deCO_2$=20% boundary has been specified regarding the hydrogen mass flow withdrawn from the storage and headed to the ammonia synthesis loop (which must be less than or equal to 3.55 t_{H2}/h, as reported in **Table 3.1**). The hydrogen storage size is evaluated according to Armijo and Philibert (2020), *i.e.* computing the minimal required storage size ($m_{H_2,\min}$) as:

$$m_{H_2,\min} = \max\left(\underline{m}_{H_2}\right) - \min\left(\underline{m}_{H_2}\right) \tag{3.3}$$

Where $\underline{m}_{H_2}$ is the vector containing all the hourly hydrogen hold-up values within the storage system ($m_{H_2,k}$) throughout the year (*i.e.* $k = 1, \ldots, 8760$). Specifically, the variation of the hydrogen storage level is computed as:

$$m_{H_2,k} - m_{H_2,k-1} = \left(\dot{m}^{IN}_{H_2,k} - \dot{m}^{OUT}_{H_2,k}\right) \cdot \Delta t \tag{3.4}$$

Where $\dot{m}^{IN}_{H_2,k}$ and $\dot{m}^{OUT}_{H_2,k}$ are the hydrogen mass flows that are entering and exiting, respectively, the storage system at each hour step (Δt). In this regard, it is worth noting that not all the hydrogen produced by the electrolyzer enters the storage: indeed, its input just consists of the excess amount that cannot be directly fed to the ammonia synthesis loop to satisfy the operating boundaries. Specifically, this also applies to the hydrogen compression section, which processes just the hydrogen flows entering the storage. Finally, **Figure 3.7** shows the total hydrogen storage capacity (*i.e.* 18.5 t_{H2}, note that "Rigid" storage would have required a capacity of 1863 t_{H2}) and hold-up variation to guarantee an average $deCO_2$=10% green hydrogen supply over an entire year while dealing with such a constraint. No specific ramping rates were considered for the green hydrogen load variation entering the Haber-Bosch process, as the gray hydrogen coming from the front-end, which represents the vast majority of the overall hydrogen feed (since constantly operating at G2GHR≤20%), easily succeeds in counteracting and mitigating such fluctuations with sufficient promptness.

For the sake of our techno-economic analysis, precisely the results for 2019 (*i.e.* the year scoring the highest – and then the most conservative – PV plant, electrolyzer, and hydrogen storage capacities of the last five years) were considered as the optimal

photovoltaic power station, electrolyzer, and hydrogen storage sizes for the *Option II* hybrid configuration.

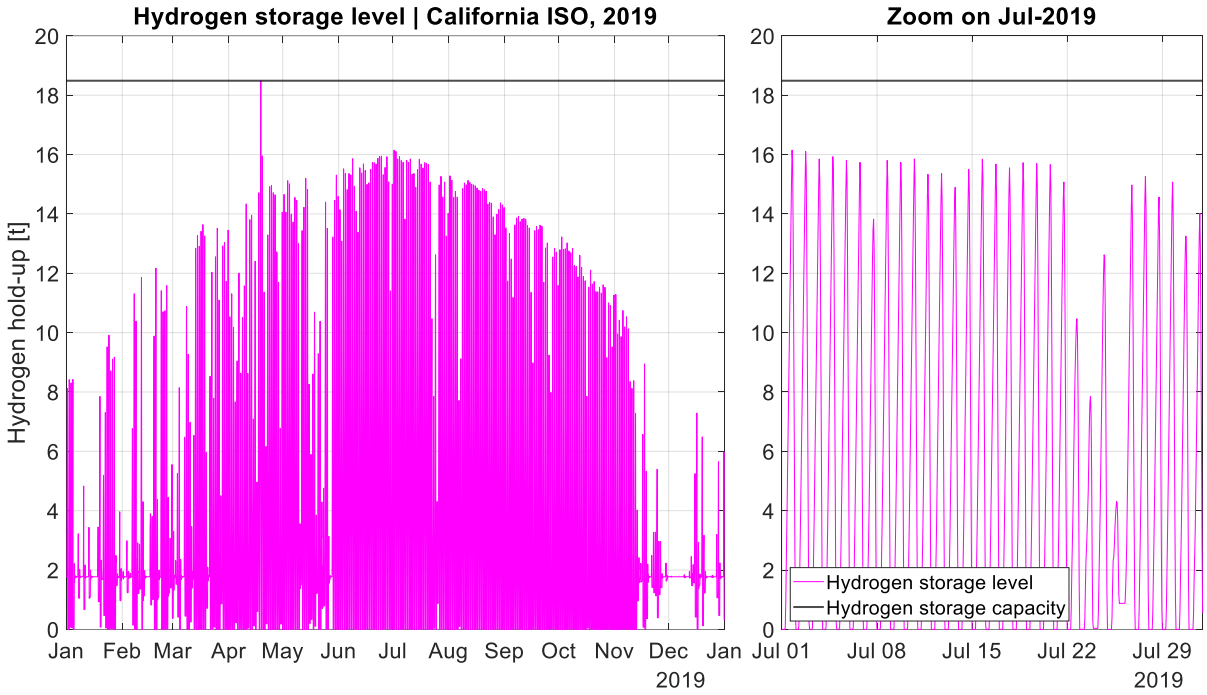

Figure 3.7: Green hydrogen storage hold-up corresponding to the renewable energy and electrolyzer profiles reported in **Figure 3.6**. The left panel shows the entire 2019-year profile, while the right panel focuses on July 2019 only.

Namely:

- PV plant with an installed capacity of 350 MW_e.
- Electrolyzer with an installed capacity of 248 MW_e.
- Hydrogen storage with a capacity of 18.5 t_{H2}.

On the other hand, an electrolyzer of 177 MW_e was considered for the *Option I* configuration, which does not feature any hydrogen storage as the grid provides the renewable electric energy, constantly ensuring target (*i.e.* $deCO_2$=10%) green hydrogen feed to the ammonia synthesis loop.

3.5. Ammonia production cost assessment

The ammonia production costs of the reference and hybrid (both *Option I* and *II*) plants were estimated. Some further details of the plants investigated are reported here:

- The production facilities operate 8000 h/y.
- The costs for cooling (CW) and demineralized (DMW) water are 0.06 USD/m^3 (Intratec, 2023a) and 0.78 USD/m^3 (Intratec, 2023b), respectively.
- The profits from the medium-pressure steam surplus, generated on-site by recovering waste heat from the process streams, are estimated by considering

the equivalent amount of natural gas that would be used to produce it in an auxiliary boiler (Noelker & Ruether, 2011). Precisely, starting from water at 35 °C and 40 bar we have a steam energy export of 0.13 MWh/t_{NH3}, regardless of the process alternative.

The ammonia production costs following the three investigated plant configurations (*i.e.* gray ammonia plant, *aka Reference*; hybrid-green ammonia plant with certified renewable electric power delivered through the grid with a PPA, *aka Option I*; and hybrid-green ammonia plant with electric power from a renewable on-site PV power plant, *aka Option II*) were estimated by considering representative values of the United States and European market quotations in 2022, 2030, and 2050 (see **Table 3.4**).

Table 3.4: United States (USA) and European Union (EU) reference market values as of 2022, 2030, and 2050. Natural gas, renewable electricity prices (VALCOE), and EU carbon prices (according to the Stated Policies Scenario, STEPS) from IEA (2023); USA (California) carbon prices from The Brattle Group (2017).

Reference market values	**2022**		**2030**		**2050**	
	USA	***EU***	***USA***	***EU***	***USA***	***EU***
Carbon price [USD_{2022}/t_{CO2}]	30	80	55	120	130	135
Natural gas [USD_{2022}/MBtu]	5.1	32.3	4.0	6.9	4.3	7.1
Renewable electricity [USD_{2022}/MWh]	55	80	55	85	60	90

Figure 3.8 shows the results of the ammonia production cost assessment for each plant configuration, while **Figure 3.9** reports all the terms that concur in determining such final costs. In the present evaluation, only one negative contribution (*i.e.* revenue) appears, corresponding to the income by selling the medium-pressure steam surplus (that depends on the natural gas price). Except for the *EU-2022* scenario, **Figure 3.8** shows that the hybrid layout always calls for higher prices than the conventional plant. **Figure 3.9** highlights that the additional expenses associated with the retrofitting significantly exceed the savings resulting from lower natural gas demand (feedstock and fuel) and carbon tax. The exception for the 2022 European market scenario occurs since at that time natural gas prices recorded unprecedented remarkably high values in the EU (with a peak quotation of 339.2 EUR/MWh in August 2022) and, although it steadily declined in the following months, it was still sold at 47.84 EUR/MWh in March 2023, which is almost seven times higher than the March 2020 price (Trading Economics, 2023). Consequently, such a trend heavily influenced the ammonia price as well. Indeed, while the average gray ammonia market price was as low as 300 USD/t_{NH3} in 2020, it exceeded 1600 USD/t_{NH3} in 2022 (EIA, 2022). In addition, concerning the market fluctuations of natural gas prices, it is worth remarking that

plants producing tradeable and storable commodities like ammonia and fertilizers generally shut down when the fossil feedstock becomes too expensive.

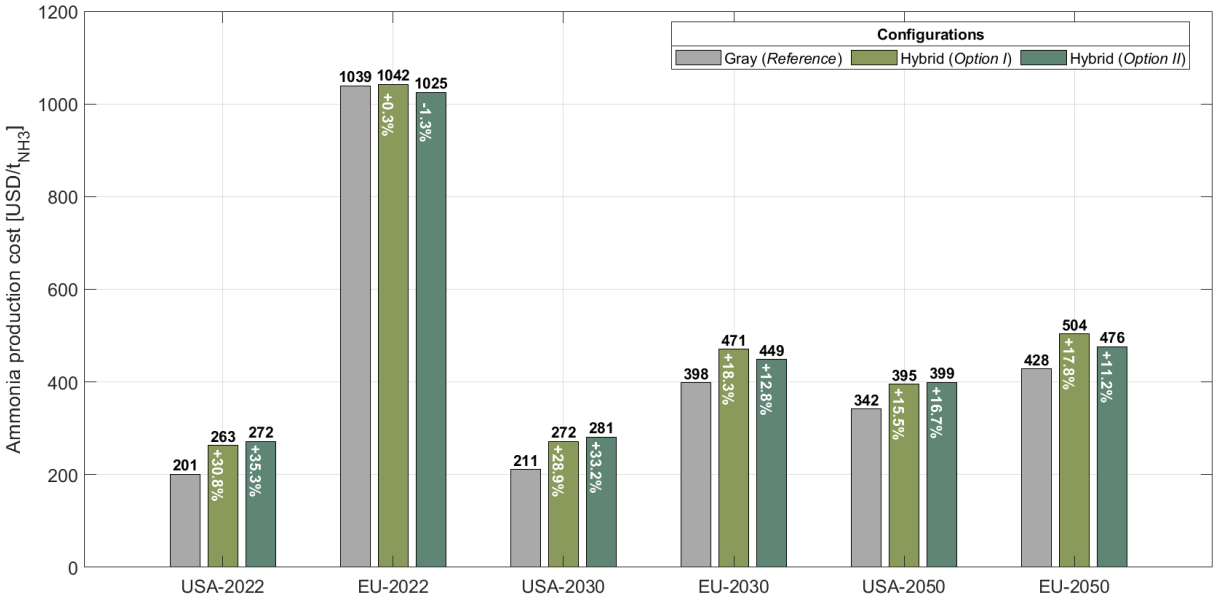

Figure 3.8: Ammonia production cost estimations for the three investigated configurations (*i.e. Reference*, *Option I*, and *Option II*) as of 2022, 2030, and 2050 in the United States and the European Union. The percentage values inside the bars refer to the percentage difference between the hybrid and gray ammonia costs.

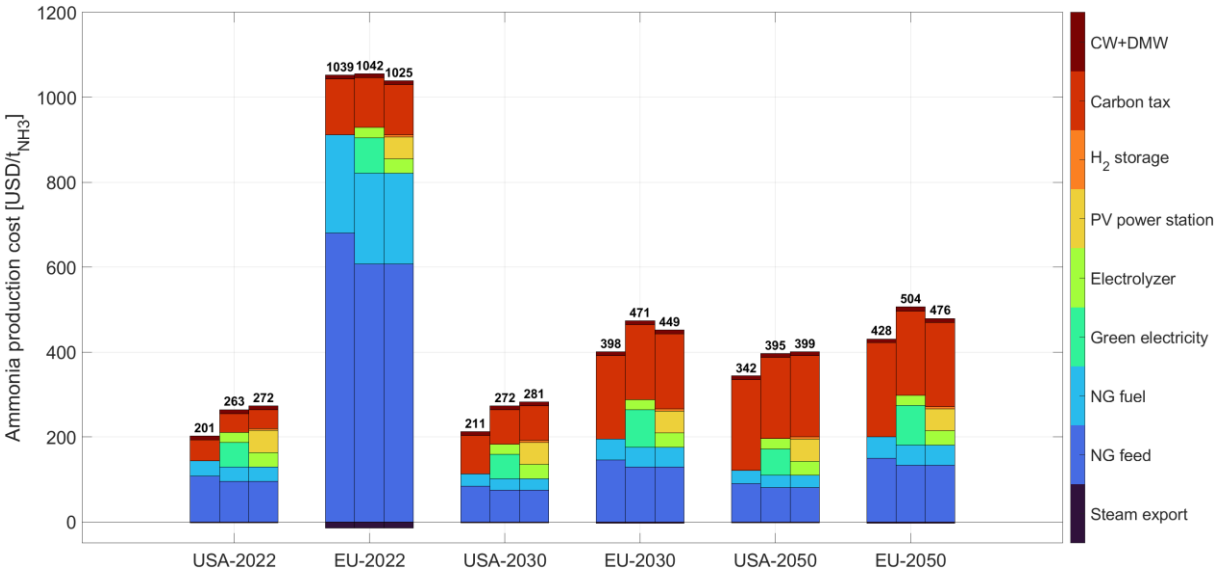

Figure 3.9: Relative importance of each contribution to the ammonia production costs by the three investigated configurations (*i.e. Reference*, *Option I*, and *Option II*) for the same scenarios reported in **Figure 3.8**. The discount associated with the medium-pressure steam export revenues on the final ammonia cost is reported as a negative contribution.

Hence, even when such a green retrofit is implemented, times of very high fuel prices might still call for a plant shutdown. Nonetheless, in this case, instead of leaving the

photovoltaic power station, the electrolyzer, and the hydrogen storage system unused (as it would lead to very high economic inefficiencies), in principle the renewable hydrogen generation section might be kept functioning (*e.g.*, to harvest and sell green hydrogen to the energy market or other final users). Of the two hybrid configurations, *Option I* is the most competitive in the USA, while *Option II* is favored in the EU. Such an outcome is mainly due to the different electricity market values in those two areas (see **Table 3.4**). Indeed, as the prices of renewable electric energy turn out to be very expensive in the EU, European scenarios discourage sourcing it from the grid and favor self-sufficiency instead. In this regard, production of renewable energy on-site as opposed to its purchase might turn out to be ever more appealing in the future thanks to three key trends: (i) as for natural gas, power purchase agreements (PPA) aimed at renewable power sourcing from the grid strongly depend on market volatility (Pexapark, 2023). Indeed, at least in Europe, PPA prices recently followed quite similar trends to those of natural gas and crude oil, strongly affected by the outburst of the Russia-Ukraine hostilities in February 2022 (Isella *et al.*, 2023). (ii) Renewable power generation technologies have shown monotonically decreasing costs (in terms of both CapEx and OpEx) in the last decades. Indeed, concerning the PV power station of *Option II*, it is worth noting that the global weighted-average levelized cost of electricity from utility-scale PV plants dropped by 82% in the last decade, from around 378 USD/MWh in 2010 to 68 USD/MWh in 2019 (IRENA, 2020). (iii) The continuously increasing service lifetime (and, consequently, longer depreciation times) of the renewable power generation infrastructures strongly mitigates the weight of CapEx contributions on the *Option II* final ammonia cost. By entering a decarbonized economy, PV power plants also represent valid investments for a possible switch to completely green ammonia synthesis or to produce power from renewables even when the production facility would end its lifetime (*e.g.*, for urban use in nearby residential areas). Finally, to quantify the appeal of the hybrid green retrofitting strategy, the CO_2 avoidance cost of both hybrid configurations was evaluated for each assessed market scenario (see **Table 3.5**).

Table 3.5: CO_2 avoidance cost of both hybrid layouts for each assessed market scenario.

CO_2 avoidance cost [USD_{2022}/t_{CO2}]	**2022**		**2030**		**2050**	
	USA	***EU***	***USA***	***EU***	***USA***	***EU***
Hybrid (*Option I*)	395	98	412	549	441	580
Hybrid (*Option II*)	450	1	468	423	464	417

Precisely, the CO_2 avoidance cost is the extent of carbon tax at which the cost of the product of interest is the same either by producing it from the conventional, carbon-intensive route (but paying the carbon tax) or from a plant including carbon mitigation (thus avoiding most of the carbon tax) (Simbeck & Beecy, 2011). Except for the *EU-2022*

scenario (which is not fully representative due to the exceptionally high natural gas prices recorded in Europe right after the outbreak of the Russia-Ukraine war), all the estimated CO_2 avoidance costs are very high. Especially considering that conventional carbon capture, utilization, and storage (CCUS) technologies range today between 15-25 USD/t_{CO2} for industrial processes generating highly concentrated CO_2 streams (IEA, 2021). As a result, although carbon prices of 200 USD/t_{CO2} or higher might even become standard by the end of this decade (Sheppard & Hodgson, 2021) or a few years later (Kaufman *et al.*, 2020) (for instance, EU ETS carbon permits are showing a rapidly increasing overall trend), heavy carbon taxation seems an insufficient instrument for making hybrid-green ammonia economically attractive, especially when compared with the so-called "blue" ammonia (*i.e.* gray ammonia with CCUS). Indeed, implementing carbon removal would avoid over 70% of the CO_2 emissions (*i.e.* the *Process CO_2 emissions* in **Table 3.1**) as opposed to the sole 10% for the hybrid-green alternative. However, it must also be pointed out that, although the capture of process emissions from the manufacturing sector is well established, the development and scaling of a commercial CO_2 transport and storage infrastructure still face many obstacles. Indeed, while studies confirm that the world shows ample carbon storage capacity in salt caverns and depleted oil and gas fields, few sites have been settled for actual use (Global CCS Institute, 2021). Lastly, blue ammonia synthesis also means relying heavily on fossil fuels instead of replacing them as in hybrid-green (partially) and green (totally) ammonia synthesis.

3.6. Conclusions

Hybrid-green ammonia proved to be an available-to-date retrofitting strategy to reach partial decarbonization in the ammonia production industry. However, while the environmental sustainability of hybrid plants has been verified, their economic sustainability is currently less appealing compared to other carbon-mitigating routes (*e.g.*, gray ammonia with CCUS, *aka* blue ammonia). Indeed, disregarding the 2022 results (unusually encouraging due to the exceptional geopolitical circumstances that occurred in that year), the CO_2 avoidance costs associated with hybrid-green ammonia plants (operating at deCO_2=20% at maximum) generally exceed 400 USD/t_{CO2} in the USA and 500 USD/t_{CO2} in the EU. Alternatively, CCUS costs are currently an order of magnitude lower, ensuring CO_2 abatement potentials above 70%. Regarding the production costs achieved by the two investigated hybrid configurations, *Option I* showed percentage differences ranging from +0.3% (*EU-2022*) to +30.8% (*USA-2022*) compared to the *Reference* case (gray ammonia) over the assessed scenarios. Conversely, *Option II* resulted in ammonia production costs ranging from −1.3% (*EU-2022*) to +35.3% (*USA-2022*), compared to the *Reference* case. Specifically, *Option I* resulted in the most competitive configuration in the USA, as electricity sourcing from American renewable electric grids is now less expensive than directly generating it on-site (due to still moderately high CapEx associated with the photovoltaic station). On

the other hand, high renewable electricity prices in Europe have led *Option II* to stand as the most competitive configuration in the EU. A few additional remarks follow: first, in many geographical areas, the only way to provide renewable power is by considering an on-site production as seen in *Option II* (mainly because the concept, and the infrastructures, of a renewable electrical grid still needs to evolve in the next years and decades and may be unavailable at the present time, especially for big consumers). Second, the quite optimistic results shown by both *Option I* and *Option II* should encourage governments to invest in the creation and diffusion of renewable energy generation infrastructures and truly renewable electric grids to facilitate the access of the chemical industry and the manufacturing sector to renewable energy and – concerning the grids – to mitigate better the problems associated to intermittent power availability. Third, as a final consideration, the hybrid-green ammonia route might become increasingly competitive by entering a progressively decarbonized economy. Indeed, this already happened in 2022 due to the exceptional rise in natural gas prices (Isella *et al.*, 2023) and may occur again if proper decarbonization policies are adopted.

4 Flexible hydrogen storage

Introductory comment

As discussed in the previous chapter, storage systems are essential to reconcile the erratic nature of renewable sources with the rigidity of chemical plants. Among them, the most common method is placing a material storage system of the green hydrogen product from the electrolyzer (as it is a very flexible process unit) and the downstream chemical process (as it typically is much less flexible). Because of the high costs related to hydrogen compression and storage, the design of such systems was thoroughly investigated. Specifically, this study led to a highly accessible and intuitive criterion identifying the optimal withdrawal rates for hydrogen storage tanks, minimizing their sizes and total costs. Once again, the results confirmed that greater process flexibility allows for remarkable cost savings.

The present chapter stems from:

A general criterion for the design and operation of flexible hydrogen storage in Power-to-X processes

Isella, A., & Manca, D.

International Journal of Hydrogen Energy, 2025, 99, 649–660

DOI: https://doi.org/10.1016/j.ijhydene.2024.12.228

Abstract

This chapter introduces a general criterion for the optimal design and operation of hydrogen storage tanks. Specifically, the proposed procedure identifies the optimal delivery schedule that minimizes the capacity of material storage systems. Indeed, many manufacturing processes need some buffer storage to administer mass flows appropriately according to the operating needs (one class above all: Power-to-X processes) and have one of their highest expenditures right in those tanks when proving not sufficiently flexible. Hence, the novelty of the proposed method lies in a rigorous mathematical formulation that converts arbitrarily fluctuating inlet streams into optimally fluctuating outlet streams that minimize the storage volume and comply with different operating requirements. The criterion is validated by considering the techno-economic assessment of a chemical plant featuring a dedicated green hydrogen production facility that feeds the process. Specifically, the required capacity of the "*Flexible*" hydrogen buffer storage, which connects the green hydrogen generation system to the conversion process, significantly decreases by 91.31%-99.31% (depending on the flexibility ranges enabled by the downstream conversion process) compared to the "*Rigid*" storage alternative based on a constant outlet mass flow withdrawal, coinciding with the hydrogen consumption rate at nominal operating conditions. Correspondingly, the resulting levelized cost of hydrogen benefits accordingly, ranging from 4.19 to 6.03 USD/kg (California, 2023).

4.1. Introduction

As we gradually enter the so-called "green economy", an increasing number of manufacturing processes call for either a redesign (for greenfield projects) or a retrofit (for brownfield facilities) to comply with the increasingly stringent environmental standards. Specifically, this is also the case of the chemical industry, which today accounts for approximately 6.5% of the global anthropogenic greenhouse gas emissions (Isella & Manca, 2022). In this regard, one of the most promising lines of action consists in replacing the "gray" (*i.e.* by fossil-based steam reforming) hydrogen commonly fed to heavily carbon-intensive petrochemical processes (*e.g.*, ammonia and methanol synthesis) with "green" (*i.e.* by renewable-energy-powered water electrolysis) hydrogen (Incer-Valverde *et al.*, 2023). However, by doing so, the operations of such plants cannot be carried out in steady-state conditions anymore. Indeed, they need to adapt to the intermittence of renewable energy sources. As these sources (*e.g.*, solar and wind power) are distinctly subject to rapid fluctuations and substantial seasonal variabilities, they typically transfer such discontinuous trends to the downstream conversion processes. In simpler terms, powering an electrolyzer with intermittent electricity translates to equally intermittent hydrogen production. However, the fluctuations of renewable energy sources clash with the demand for steady-state operation of continuous equipment in chemical plants, which (although

allowing flexible operation, *i.e.* neither in stationary nor in nominal conditions) require an adequate supply (*i.e.* between a minimum and a maximum threshold) to meet both quantitative and qualitative specifications of the process adequately. Hence, mitigating the impact of such intermittencies on the rest of the plant is why the call for buffer storage systems is growing. Few works in the scientific literature have carried out a techno-economic assessment related to this class of green processes (*aka* "Power-to-X", where "Power" originates from renewables and "X" denotes the final product) (Nayak-Luke *et al.*, 2018; Armijo & Philibert, 2020; Mucci *et al.*, 2023a; Isella *et al.*, 2024), and distinctly highlighted the beneficial effects of operating flexibility on the production costs.

Table 4.1: Relevant works addressing flexible hydrogen storage design in Power-to-X processes.

	Power-to-X process	**X-process flexibility**	**Problem formulation**[1]
Armijo and Philibert (2020)	Power-to-NH_3	Yes	MINLP
Li *et al.* (2020)	Power-to-NH_3	Yes	LP
Osman *et al.* (2020)	Power-to-NH_3	No	LP
Chen and Yang (2021)	Power-to-CH_3OH	Yes	LP
Chen *et al.* (2021)	Power-to-CH_3OH	No	NLP
Mucci *et al.* (2023a)	Power-to-CH_3OH	Yes	MINLP
Wang *et al.* (2023)	Power-to-NH_3	Yes	MDP
Marocco *et al.* (2024)	Power-to-H_2	Yes	MILP
Weiss and Ikäheimo (2024)	Power-to-Steel	Yes	LP

[1] LP = Linear Programming; MDP = Markov Decision Process; MILP = Mixed-Integer Linear Programming; MINLP = Mixed-Integer Nonlinear Programming; NLP = Nonlinear Programming.

Precisely, the most common process alternatives are placing a hydrogen storage tank downstream of the electrolyzer or, otherwise, a battery system for electric energy storage amidst the renewable power plant and the electrolyzer (some plants even show both features together). As we will extensively discuss the latter option in the next chapter, where a framework for the optimal design of battery electric storage systems (BESS) is proposed (Isella & Manca, 2025a), we will now focus only on the former (*i.e.* the use of buffer storage tanks). The major novelty introduced by this chapter consists

indeed of a general criterion that identifies the optimal dynamic delivery schedule, which minimizes the capacity of a material storage system (hence both its capital and operating expenditures) while also complying with multiple supply specifications demanded by the downstream conversion process (*e.g.*, target productivity, ramping rates, and load flexibility constraints). Indeed, the scientific works covering this subject (such as those reported in **Table 4.1**) typically estimate the hold-up variation and the resulting size of the hydrogen storage system as the result of specified constraints within the addressed techno-economic modeling and optimization problem, without applying (or, at least, reporting explicitly) any mathematical expressions to optimally evaluate the outlet mass flows to be dynamically withdrawn from the storage system. To our knowledge, no previous work has ever provided methodologies addressing the design of flexible storage systems that can be easily extrapolated from the optimization procedure they belong to (since each of them necessarily requires the formalization of *ad hoc* problem formulations). Conversely, we introduced a criterion that applies to any scale (*e.g.*, as a practical tool for short-cut estimations or as a specific constraint of rigorous optimization problems concerning any manufacturing process featuring flexible operations). Specifically, once the input mass flows from upstream processes and the (flexible) supply specifications of the downstream processes are known or assigned, the presented criterion rapidly estimates the buffer storage system's optimal withdrawal rates and hold-up profiles (hence its minimum size).

This chapter is structured as follows: Section 4.2 sets out a novel sizing criterion starting from the mathematical model of a conventional buffer storage tank; Section 4.3 validates the resulting methodology through the techno-economic assessment of an industrial facility producing renewable hydrogen to synthesize green commodity chemicals (such as ammonia or methanol), and discusses the outcomes. Lastly, Section 4.4 draws final comments and conclusions.

4.2. Mathematical model

Our dynamic delivery criterion to minimize the size of flexible storage systems refers to conventional storage tanks. Accordingly, the following discussion considers as control volume an elementary material buffer storage system like the one depicted in **Figure 4.1** (*i.e.* the "storage node"), whose mass balance is:

$$\frac{d}{dt} m(t) = \dot{m}_{IN}(t) - \dot{m}_{OUT}(t) \tag{4.1}$$

where both inlet and outlet mass flows vary in time, t. The former term ($\dot{m}_{IN}(t)$, here considered as assigned data) fluctuates according to the intermittent upstream conditions; the latter term ($\dot{m}_{OUT}(t)$) must be subject to a suitable user-defined delivery schedule (*e.g.*, the optimal one that we intend to develop). Such a delivery schedule shall also consider that the outlet flow must comply with the requirements of the downstream units: *e.g.*, when providing the feedstock to a conversion process, the

storage system cannot deliver mass flows either above or below the maximum or minimum allowed loads, or displaying a too much high rate of change.

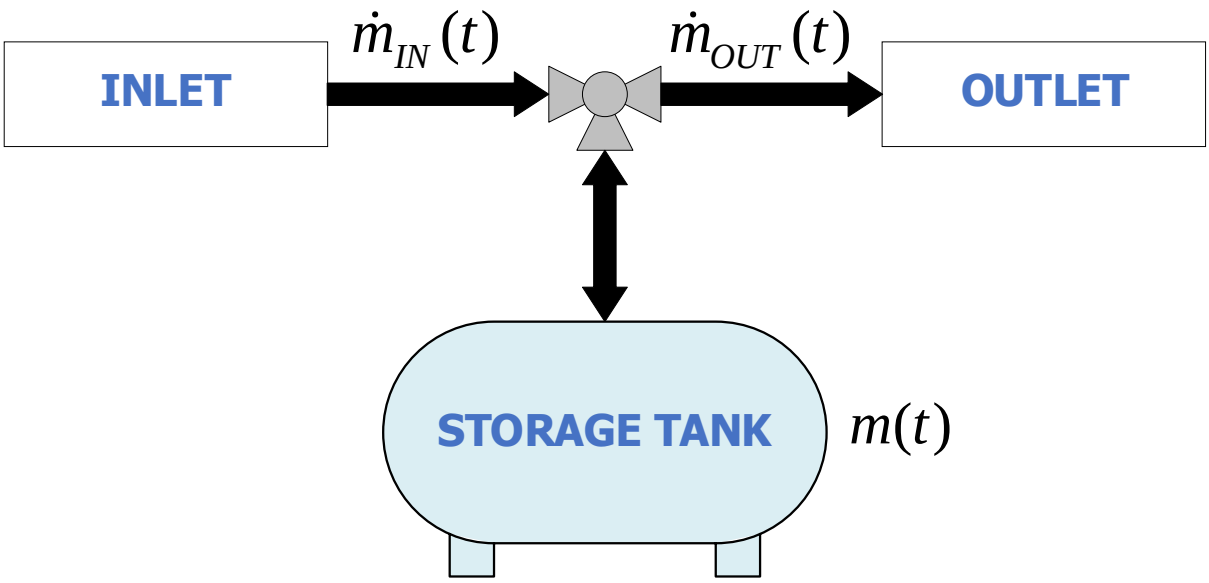

Figure 4.1: A conventional material buffer storage system (*i.e.* the control volume of the proposed criterion).

Hence, the key principle of our criterion is to estimate the optimal $\dot{m}_{OUT}(t)$ that (i) complies with such operational constraints and (ii) minimizes the capacity (and thus the total costs) of the storage. In other words, point (ii) implies that the accumulation term should always be as small as possible, ideally:

$$\frac{d}{dt}m(t) \to 0 \tag{4.2}$$

By looking again at Eq. (4.1), it follows that Eq. (4.2) holds if and only if:

$$\dot{m}_{OUT}(t) = \dot{m}_{IN}(t) \tag{4.3}$$

However, there are many cases in which we cannot make the outlet mass flow equal to the inlet one. Namely: (a) when $\dot{m}_{OUT}(t)$ falls below the minimum value of mass flow required downstream; (b) when $\dot{m}_{OUT}(t)$ exceeds the maximum value of mass flow required downstream; (c) when $\dot{m}_{OUT}(t)$ does not meet some bumpless implementations (*e.g.*, a specific ramping rate) of the outlet stream such as ±X% variations at most as against either previous values or assigned maximum deviations.

Accordingly, when such conditions occur, the storage system must accumulate/hold the absolute difference between the inlet and the (constrained) outlet streams. Therefore, to account for these occurrences (and then to discharge the resulting hold-up whenever possible, both to fully satisfy the downstream demand and minimize the

required storage capacity), an additional term is introduced, acting as a "memory" of the limitations encountered so far in applying Eq. (4.3):

$$\dot{m}_{OUT}(t) = \dot{m}_{IN}(t) + \frac{1}{\Delta t} \cdot \int_{1}^{t-1} \left[\dot{m}_{IN}(\tau) - \dot{m}_{OUT}(\tau) \right] d\tau \tag{4.4}$$

An interesting parallel can be drawn between Eq. (4.4) and the integral law for feedback controllers (Stephanopoulos, 1984): following the analogy, the accumulation within the storage tank can be viewed as the error term that such a control law aims to nullify, at all times, as far as possible.

Nevertheless, since the profiles of industrial variables (especially those concerning renewable energy sources: *e.g.*, solar and wind power generation) usually show a temporal discretization (as they are mostly collected hourly), Eq. (4.4) is rewritten and adapted to the typical discrete formulation of such problems (from now on, in fact, only discrete formulae will be considered):

$$\dot{m}_{OUT}(t) = \dot{m}_{IN}(t) + \sum_{\tau=2}^{t} \left[\dot{m}_{IN}(\tau - 1) - \dot{m}_{OUT}(\tau - 1) \right] \tag{4.5}$$

Specifically, Eq. (4.5) approximates the integral term in Eq. (4.4) by the Riemann sum. Indeed, it successfully applies to any definite integration problem whose function to be integrated is generally continuous (*i.e.* according to the Riemann-Lebesgue criterion, the set of discontinuity points, if any, has a null measure). Furthermore, higher computational ease aside, such a technique was preferred over numerical integration methods based on interpolating functions (such as Simpson's rule) as it reconstructs the discrete-time values as a piecewise-constant continuous profile (*i.e.* a procedure that, by its nature, never generates values outside the range of the discrete-time ones). On the other hand, methods based on n-order polynomial interpolations (*e.g.*, Simpson: n=2) might introduce non-conservative excursions beyond the range of the discrete-time values of the dataset they aim to integrate (Stephanopoulos, 1984; Manca, 2007).

Consequently, the resulting $\dot{m}_{OUT}(t)$ should be checked to guarantee that it complies with the aforementioned (a), (b), and (c) cases. If yes, it can be imposed as it is; if not, it should be replaced by the closest allowed value (*i.e.* the one respecting the lower or upper limits according to the downstream constraints). Furthermore, since the first element of $\underline{\dot{m}}_{OUT}$ cannot be estimated from Eq. (4.5) (as $\dot{m}_{OUT}(t-1)$ is needed), such a value is specially assigned ahead of the rest: if $\dot{m}_{IN}(1)$ falls within the allowed mass flow range that can be supplied downstream (according to the process specifications), $\dot{m}_{OUT}(1)$ shall match it; if $\dot{m}_{IN}(1)$ is higher/lower than the maximum/minimum allowed load, $\dot{m}_{OUT}(1)$ shall coincide with such a maximum/minimum value.

For the sake of completeness, we report a MATLAB implementation of the criterion (as for the notation used so far in the equations above, it is worth noting that MATLAB arrays start from element 1 instead of 0):

Algorithm 4.1: Flexible storage sizing framework

```
function m_OUT = STORAGE_size(m_IN,m_OUT_MIN,m_OUT_MAX,Ramp)
% Pre-allocate the m_OUT vector
m_OUT = zeros(1,length(m_IN));
% Evaluate the 1st value of the m_OUT vector
if m_IN(1) <= m_OUT_MIN % check case (a)
    m_OUT(1) = m_OUT_MIN;
elseif m_IN(1) >= m_OUT_MAX % check case (b)
    m_OUT(1) = m_OUT_MAX;
else
    m_OUT(1) = m_IN(1);
end
% Computing all the other values of the m_OUT vector
for t = 2:length(m_IN)
m_OUT(t) = m_IN(t) + sum(m_IN(1:t-1) - m_OUT(1:t-1)); % Eq. (4.5)
    % Check case (c)
    if m_OUT(t-1) ~= 0
        m_OUT(t) = min(m_OUT(t),(1+Ramp)*m_OUT(t-1)); % Upper bound
        m_OUT(t) = max(m_OUT(t),(1-Ramp)*m_OUT(t-1)); % Lower bound
    end
m_OUT(t) = max(m_OUT(t),m_OUT_MIN); % check case (a)
m_OUT(t) = min(m_OUT(t),m_OUT_MAX); % check case (b)
end
end
```

Therefore, once the optimal outlet mass flow profile is estimated, the corresponding mass hold-up profile within the storage tank is provided by numerically integrating Eq. (4.1):

$$m_0(t) = \sum_{\tau=1}^{t} \left[\dot{m}_{IN}(\tau) - \dot{m}_{OUT}(\tau) \right] \Delta t \tag{4.6}$$

As for Eq. (4.5), the integration performed by Eq. (4.6) relies on the Riemann sum due to the piecewise constant data profiles considered in such temporally discretized problems. However, since the mass profile resulting from Eq. (4.6) might assume even non-positive values (*e.g.*, due to the prevalence of negative accumulation terms), $\underline{m}_0$ is

entirely shifted to the non-negative real numbers domain (*i.e.* $\forall m(t) \in \mathbb{R}_{\geq 0}$, according to the physical sense of the problem) by referring to its minimum value:

$$m(t) = m_0(t) - \min(\underline{m}_0) \tag{4.7}$$

Analogously, the minimal required capacity of the storage system can be computed as:

$$m_{tot} = \max\left(\underline{m}_0\right) - \min\left(\underline{m}_0\right) = \max\left(\underline{m}\right) \tag{4.8}$$

Lastly, once the storage system's size is known, its capital and operating expenditures can be assessed. It is worth highlighting that the present criterion, whose core novelty essentially lies in Eq. (4.5), allows the estimation of $\underline{\dot{m}}_{OUT}$ (*i.e.* the vector of the outlet mass flows) and m_{tot} just from $\underline{\dot{m}}_{IN}$ (*i.e.* the vector of the inlet mass flows, given as input data). No additional parameters are required. Also, for how it was developed, this methodology intrinsically leads to full respect for any productivity specification (*e.g.*, according to a following conversion process) as long as the input streams do. Indeed, as our flexible storage system attempts to transfer all the input flows as output flows to nullify the instantaneous accumulation at each time step, one must only be sure that the input itself as a whole (over the assessed timespan) is sufficient to satisfy the user's requirements. In this regard, any residual deviation from the overall amount supplied downstream may eventually arise only at the very last hours of operations, since temporary accumulations due to those mentioned above (a), (b), and (c) cases remain pending as the assessed time window suddenly ends. As a final remark, it is worth observing that the proposed model refers to a control volume that considers the storage system as a "node" between the upstream and downstream units. In this regard, industrial practice shows that not all the mass flows coming from the preceding units and going to the following ones must pass through the storage system. Indeed, when not needed, it can be bypassed (through the three-way valve of **Figure 4.1**). In such cases, the user must consider $\dot{m}_{IN}(t)$ and $\dot{m}_{OUT}(t)$ as the mass flows entering and exiting that node (*i.e.* the control volume, not necessarily the storage tank). On the contrary, the mass flows specifically entering/exiting the storage tank can be estimated by referring to the positive/negative values resulting from Eq. (4.1) (*i.e.* the accumulation term, which truly affects the storage hold-up).

4.3. Validation and discussion

The proposed criterion is validated through a case study. Although, in principle, our method applies to any industrial process involving a material storage system, we will now focus on Power-to-X plants and, specifically, the production of commodity chemicals from green hydrogen. Indeed, these processes have become increasingly relevant in recent years due to the global effort to decarbonize the manufacturing sector (Mucci *et al.*, 2023b) and, particularly, to mitigate the environmental impact of

hydrogen production (being conventionally based on fossil feedstocks such as natural gas, oil, and coal).

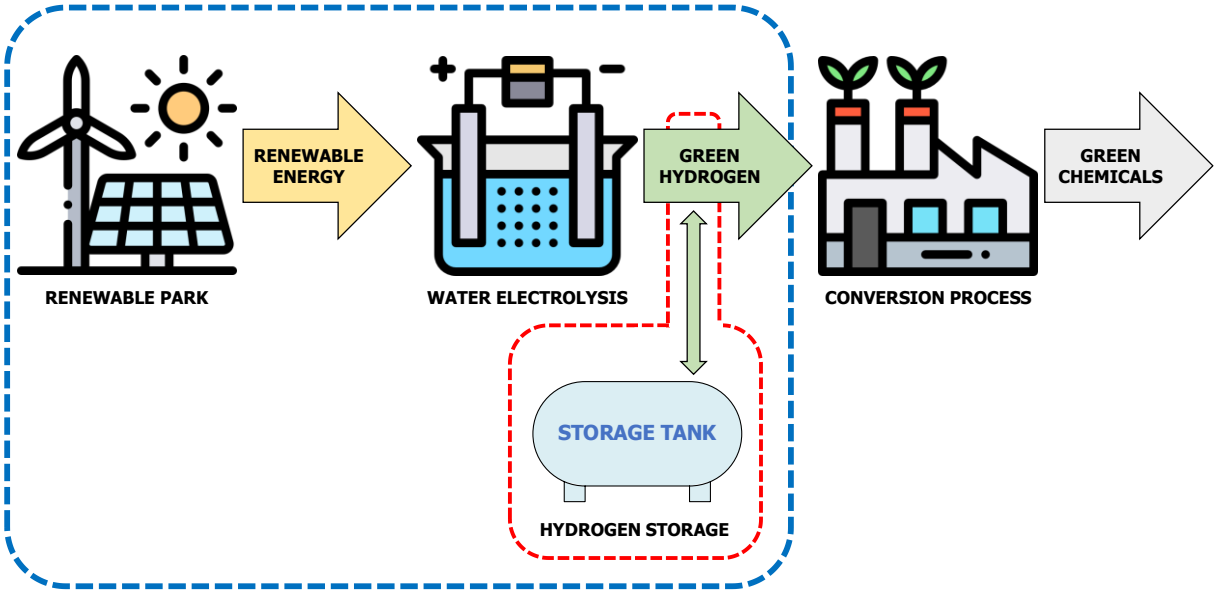

Figure 4.2: The typical layout of a Power-to-X plant. The dashed red box (*i.e.* the buffer hydrogen storage system, located amidst the electrolyzer and the conversion process) is the control volume of our sizing criterion; the dashed blue box is the control volume of the following optimization problem.

Figure 4.2 shows a typical configuration of such chemical processes (*i.e.* "Power-to-X" or, even more precisely, "Power-to-Chemicals"), which will also act as the case study assessed to validate the presented methodology. Specifically, here, the hydrogen buffer storage is key to properly administering the green hydrogen input flow (as it continuously fluctuates due to the intermittent availability of renewable energy) in compliance with the downstream process requirements (*e.g.*, maximum vs. minimum deviations from the nameplate capacity and/or maximum feedstock ramping rates). Specifically, we consider a solar-and-wind-powered Power-to-X plant in California (United States) whose conversion process calls for a nominal green hydrogen feed rate ($\dot{m}_{OUT}^{target}$) of 1 t_{H2}/h (a value that can approximately lead to productivities of either 136 t/d of green ammonia or 192 t/d of green methanol). Such a geographical location has been chosen due to the extensive collection of renewable power generation data made available by the California Independent System Operator (CAISO) (CAISO, 2024), *i.e.* one of the largest and most modern power grids in the world that also boasts a significant integration of renewable resources into the transmission system (an estimated 36% of California's electricity retail sales in 2019 (CAISO, 2021)).

To identify the economically optimal design of the Power-to-Hydrogen facility (*i.e.* the one minimizing the production cost of the green hydrogen intended for the downstream conversion process), we must consider an optimization problem that determines the best sizes of the renewable (*i.e.* solar and wind) power plant, the

electrolyzer, and the hydrogen storage. The optimization procedure is very similar to the one shown in Isella and Manca (2024), and is reported in Eq. (4.9):

$$
\begin{cases}
\underset{P^{S}_{\text{inst}},P^{W}_{\text{inst}}}{\textbf{Min}}\left[LCOH = \dfrac{\sum_{j=S,W,E,H}\left(CapEx_y + OpEx\right)_j}{8760\cdot \dot{m}^{H_2}_{\text{target}}} \right] & \\
\text{s.t.:} & \\
\dot{E}^{E}(t) = \min(\dot{E}^{S}(t) + \dot{E}^{W}(t), P^{E}_{\text{inst}}) & \text{(a)} \\
\sum_{\tau=1}^{8760} P^{E}(\tau) = 8760\cdot \dot{E}^{E}_{\text{target}} & \text{(b)} \\
\dot{m}^{H_2}_{IN}(t) = P^{E}(t)\cdot \dfrac{\rho_{H_2}}{\xi_E} & \text{(c)} \\
\dot{m}^{H_2}_{OUT}(t) = \dot{m}^{H_2}_{IN}(t) + \sum_{\tau=2}^{t}\left[\dot{m}^{H_2}_{IN}(\tau-1) - \dot{m}^{H_2}_{OUT}(\tau-1)\right] & \text{(d)}
\end{cases}
\tag{4.9}
$$

Where $LCOH$ is the levelized cost of hydrogen; P^{S}_{inst}, P^{W}_{inst}, and P^{E}_{inst} are the installed capacities of the solar farm, wind farm, and electrolyzer, respectively; $\left(CapEx_y + OpEx\right)_{S,W,E,H}$ are the sum of the annualized capital expenditures ($CapEx_y$) and the annual operating expenditures ($OpEx$) of the solar farm (S), wind farm (W), electrolyzer (E), and hydrogen storage system (H), respectively; 8760 (hours) is the timespan assessed, that is one year (assuming uninterrupted operation, *i.e.* neither maintenance breaks nor emergency shutdowns occur); $\dot{E}^{S}(t)$ and $\dot{E}^{W}(t)$ are the instantaneous renewable power delivered by the solar and wind farms, respectively (depending on the solar and wind total installed capacity); $\dot{E}^{E}(t)$ is the instantaneous power fed to the electrolyzer; $\dot{E}^{E}_{\text{target}}$ is the electric power that the electrolyzer needs to operate at the nominal hydrogen production rate $\dot{m}^{H_2}_{\text{target}}$ (*i.e.* 1 t_{H2}/h); $\dot{m}^{H_2}_{IN}(t)$ and $\dot{m}^{H_2}_{OUT}(t)$ are the hydrogen mass flow entering and exiting the storage node, respectively; lastly, ξ_E is the specific (*i.e.* per normal cubic meter of hydrogen) electricity consumption of the electrolyzer and ρ_{H_2} is the hydrogen mass density. With regards to the equality constraints: (a) $P^{E}(t)$ equals the overall (*i.e.* both solar and wind) generated renewable electricity but bounded above by the installed capacity of the electrolyzer (*i.e.* what exceeds such a threshold is curtailed); (b) the amount of renewable energy fed to the electrolyzer throughout the whole year must be equal to the electricity needed to meet the hydrogen productivity target; (c) the hydrogen produced by the electrolyzer is estimated by assuming constant power consumption and perfectly flexible behavior, consistent with latest electrolysis technologies (Armijo & Philibert, 2020); and (d) the hydrogen product is sent to the downstream conversion process according to our dynamic delivery criterion developed in Section 4.2. For further information on the

hydrogen production model and the conversion process operation, additional details are provided by Isella *et al.* (2024), as it addresses the green retrofitting of a gray ammonia plant through a similar optimization problem formulation. It is worth noting that, though the present case study assumes a constant target demand (*i.e.* 1 t_{H2}/h), our model may also contemplate fluctuating target demands, as long as they are scheduled *a priori*, *i.e.* before running the searching phase. In this way, such operating requirements can be properly subject to suitable equality constraints, such as Eq. (4.9b), referring to each time frame wherein target demand varies. Therefore, according to chemical process control terminology, this criterion does not provide for regulation problems in downstream target demand, yet it covers planned servo problems. **Table 4.2** reports all the techno-economic specifications used as input data by the optimization procedure.

Table 4.2: Techno-economic input data for the optimization problem.

	Value	Unit	Reference
Interest rate	5	%	Mucci *et al.* (2023a)
Solar (Photovoltaics)			
Capacity factor (California, 2023)	26.64	%	CAISO (2024)
CapEx (USA, 2022)	1119	USD/kW	IRENA (2023)
OpEx	1.70	% CapEx/y	Armijo and Philibert (2020)
Life	25	y	Armijo and Philibert (2020)
Wind (Onshore)			
Capacity factor (California, 2023)	29.66	%	CAISO (2024)
CapEx (USA, 2022)	1285	USD/kW	IRENA (2023)
OpEx	2	% CapEx/y	Armijo and Philibert (2020)
Life	25	y	Armijo and Philibert (2020)
Electrolyzer (Alkaline)			
Electricity consumption	4.65	kWh/Nm^3_{H2}	McPhy (2023)
CapEx	700	USD/kW	Isella *et al.* (2024)
OpEx	2	% CapEx/y	Armijo and Philibert (2020)
Life	10	y	Isella *et al.* (2024)

Hydrogen storage (Compressor & Type I tanks @ 200 bar)			
CapEx[1]	1900	USD/kg$_{H2}$	Isella *et al.* (2024)
OpEx[2]	1	% CapEx/y	Armijo and Philibert (2020)
Life	10	y	Isella *et al.* (2024)
Conversion process (Flexibility constraints)			
Nominal H_2 feed mass flow	1	t$_{H2}$/h	Assumption
Minimum H_2 feed mass flow (turn-down)	70	% Nominal H_2 feed	Assumption
Maximum H_2 feed mass flow (turn-up)	110	% Nominal H_2 feed	Assumption
Maximum ramping rate	±20	%/h	Assumption

[1] Capital costs for Type I tanks and the compression system; [2] Excluding compression power (*i.e.* electricity supplied by the renewable power plant).

Hence, the optimization problem is solved by implementing a grid-search minimization routine on MATLAB R2024a and selecting an investigation region with installed solar and wind capacities both ranging from 0 to 350 MW.

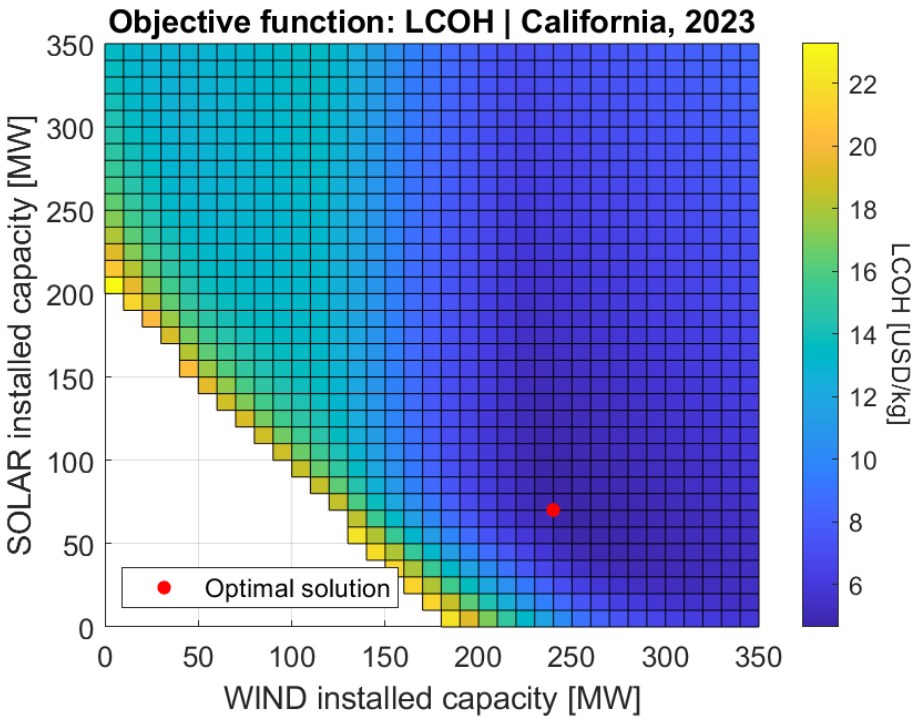

Figure 4.3: Objective function (*i.e.* LCOH) of the optimization problem reported in Eq. (4.9). The red dot represents the optimal solution (*i.e.* the solar and wind installed capacities minimizing the LCOH, equal to 4.64 USD/kg), while the white area represents the unfeasibility region.

First, **Figure 4.3** shows the topology of the objective function and its minimum (*i.e.* the optimal solution). Specifically, cooler colors here mean lower LCOH values and vice versa; instead, the white area at the bottom left corner of the investigated domain represents the unfeasibility region (*i.e.* all configurations whose renewable power installed capacities are not sufficiently high enough to meet the target hydrogen productivity).

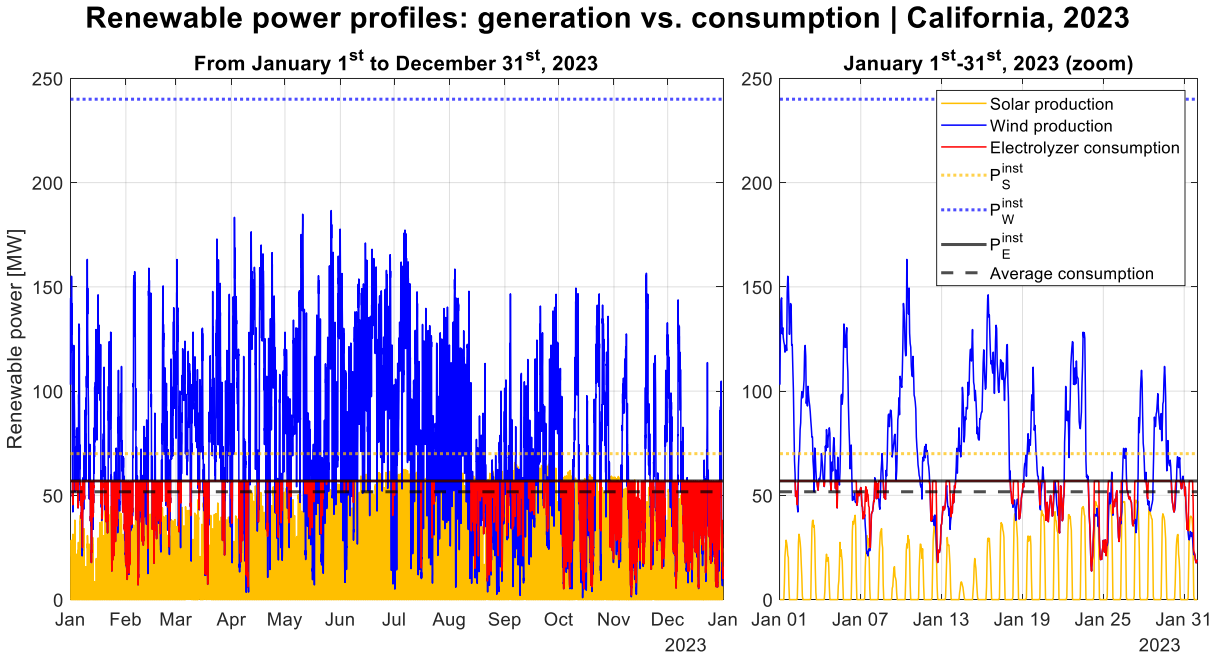

Figure 4.4: Renewable power generation and consumption profiles (considering Californian solar and wind profiles in 2023 (CAISO, 2024)) by a power plant showing 70 MW of solar and 240 MW of wind installed capacities and an alkaline electrolyzer of 57 MW. Note that the electrolyzer cannot consume power inputs exceeding its installed capacity, and the average consumption power (black dashed line) equals 51.72 MW (according to the 1 t_{H2}/h and 4.65 kWh/Nm^3_{H2} specifications).

Focusing on the optimum point, **Figure 4.4** shows the corresponding generation (at the solar and wind farms) and consumption (at the electrolyzer) of electric power profiles for the whole year assessed (*i.e.* from January 1st to December 31st, 2023). A close-up for January 2023 is also provided to visualize the trend of such curves better. From the electricity consumption profile supplied to the electrolyzer (computed in such a way that its arithmetic mean satisfies the yearly hydrogen productivity constraint, as specified by Eq. (4.9b)), the corresponding green hydrogen mass flows (*i.e.* $\underline{\dot{m}}_{IN}^{H_2}$, whose mean value over the whole year is indeed equal to 1 t_{H2}/h) are produced according to Eq. (4.9c) and, therefore, delivered to the storage node. Once there, our "*Flexible*" withdrawal policy applies (*i.e.* $\dot{m}_{OUT}^{H_2}(t)$ changes dynamically according to Eq. (4.5), see Eq. (4.9d)), as it calls for some operational flexibility downstream but grants remarkably smaller volumes and costs of the buffer hydrogen storage.

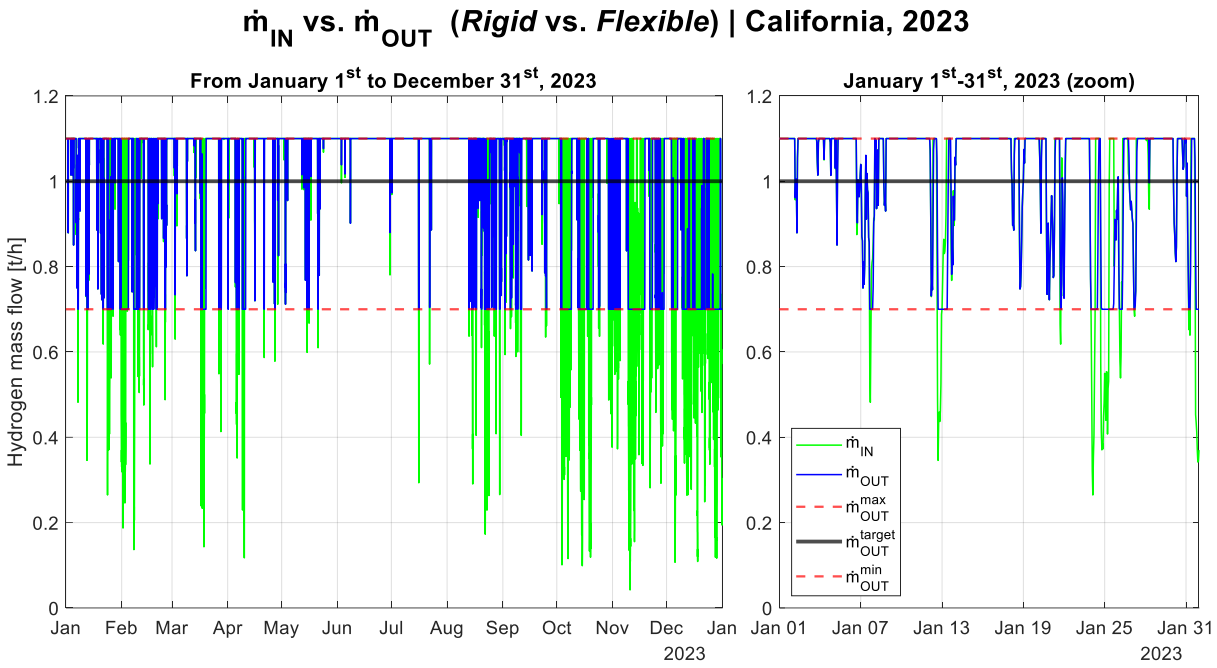

Figure 4.5: Inlet (green) and outlet (*Rigid*, black, and *Flexible*, blue) mass flows at the storage node. The red dotted lines denote the load flexibility boundaries of the downstream conversion process (*i.e.* its maximum and minimum allowed hydrogen feed rate thresholds, as reported in **Table 4.2**).

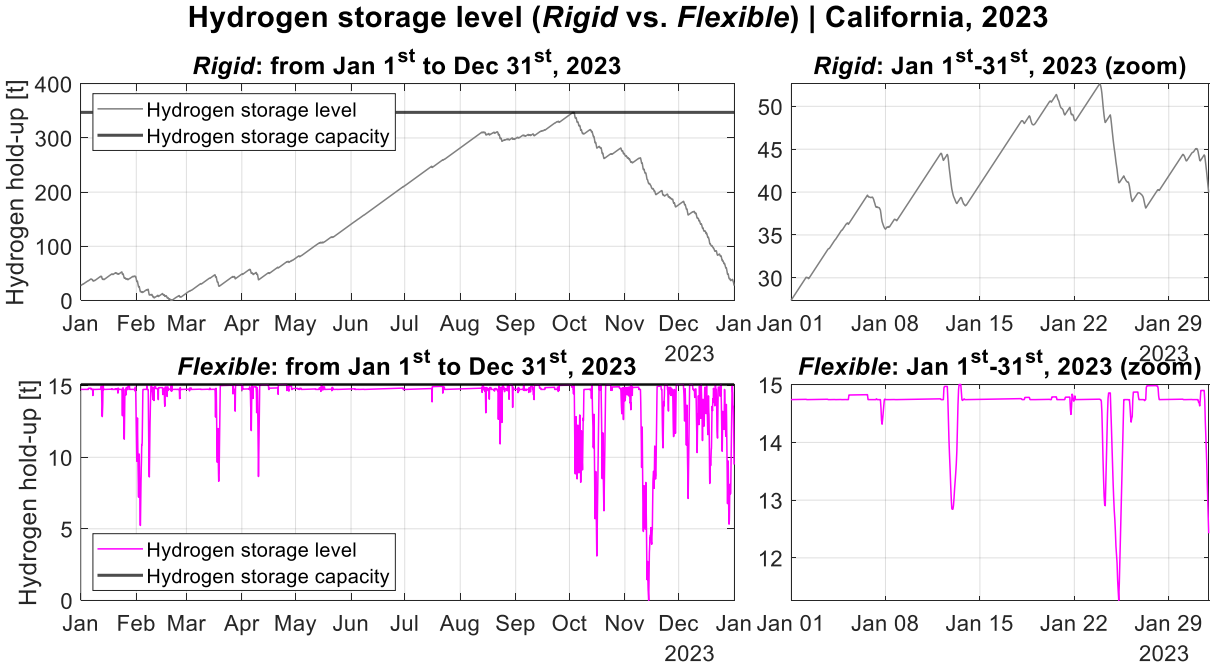

Figure 4.6: Hydrogen storage hold-up profiles and required capacity for both *Rigid* (gray) and *Flexible* (magenta) scenarios.

Specifically, as from **Table 4.2**, it has been assumed that the downstream conversion process allows both −30% and +10% (compared to its nameplate capacity) operating bounds (*i.e.* 0.7 t_{H2}/h ≤ $\dot{m}_{OUT}^{H_2}(t)$ ≤ 1.1 t_{H2}/h) and a ramp constraint equal to ±20%/h

respect to previous operating values. Alternatively, one could, in principle, consider a "*Rigid*" storage policy (*i.e.* $\dot{m}_{OUT}^{H_2}(t)$ constantly equal to $\dot{m}_{\text{target}}^{H_2} = 1$ t_{H2}/h), which would guarantee steady-state operations downstream but also lead to impressively high storage capacities, mainly due to the inability to adapt to the daily and seasonal behaviors of renewable energy generation. **Figure 4.5** shows $\underline{\dot{m}}_{OUT}^{H_2}$ (as against $\underline{\dot{m}}_{IN}^{H_2}$) according to both *Rigid* and *Flexible* withdrawal policies. At last, by applying Eqs. (7) and (8) to such inlet and outlet mass flow profiles, both the *Rigid* and *Flexible* corresponding hold-up profiles and required storage capacities can be easily computed (see **Figure 4.6**): while the *Rigid* scenario calls for a hydrogen storage capacity of 347.25 t_{H2}, the *Flexible* scenario shrinks to 15.09 t_{H2} only (hence achieving a 95.65% saving in design volume). Expressly, the comparison between the two hold-up profiles underlines how well a sufficiently flexible design can overcome the problems related to the seasonal behavior of renewable energy sources. Indeed, the *Rigid* storage visibly alternates a period of significant hydrogen abundance throughout the summer (*i.e.* when the sun and wind are most available in California (CAISO, 2024)) with a period of hydrogen depletion throughout the winter: this leads to big storage sizes as such a unit needs to store the hydrogen surplus in the summer to deliver it later during the winter. On the other hand, our sizing criterion causes the storage to suffer less from the variable availability of renewables throughout the year, allowing it to deliver more/less hydrogen when its availability is higher/lower.

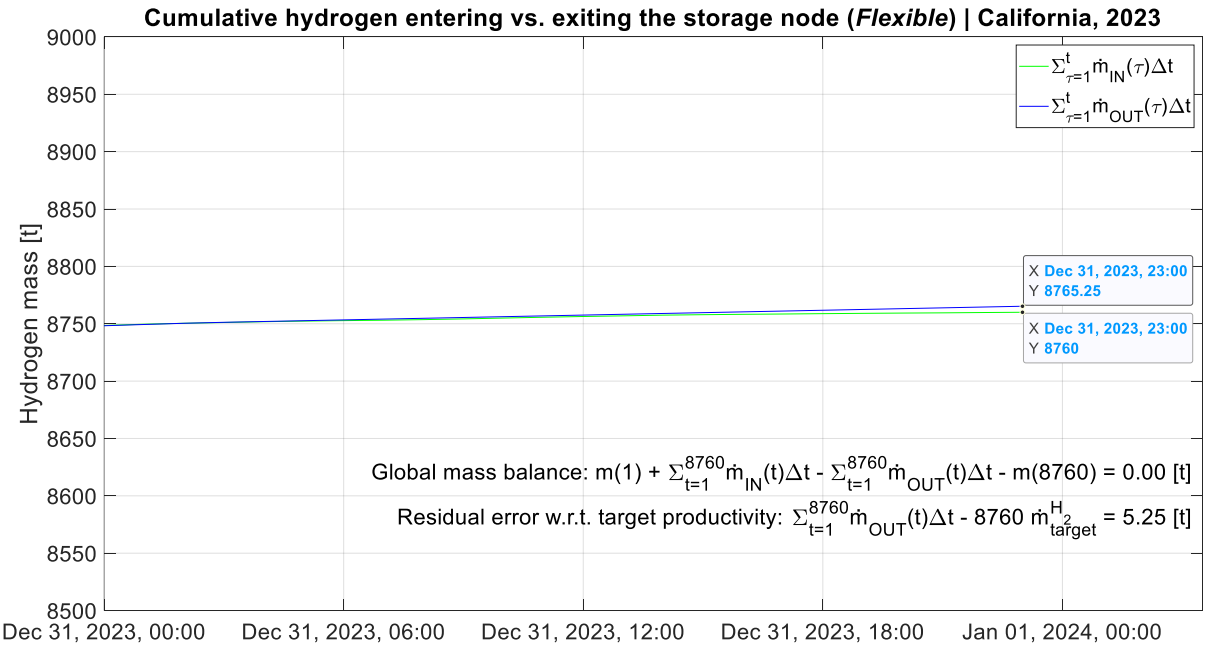

Figure 4.7: Cumulative profiles of the hydrogen mass entering and exiting the storage node (detail of the last simulated day of operation, *i.e.* December 31st, 2023).

Finally, **Figure 4.7** compares the cumulative amount of hydrogen entering vs. exiting the storage node throughout the year, as computing and visualizing them allows for performing a few consistency checks (*e.g.*, verifying that the principle of mass

conservation always applies). As expected, both values converge to 8760 t_{H2}/y (*i.e.* 1 t_{H2}/h times 8760 h/y). Hence, the difference between the specified target productivity and the hydrogen supplied to the downstream user tends to be zero, as it should always be. In other words, there is neither excessive nor insufficient hydrogen delivery compared to the target productivity: at most, minor deviations may occur just for the very last operating hours of the assessed timespan. Indeed, though in full compliance with the global mass balance, a small discrepancy arises in **Figure 4.7** between the expected hydrogen supply (*i.e.* according to the target productivity) and the actual one (*i.e.* resulting from our dynamic delivery policy). This happens because of the prolonged occurrence of limiting cases (a), (b), and (c) (see Section 4.2) in the last operating hours, as they trigger short-term disturbances that call for being mitigated later on, as soon as the opportunity arises. However, as the time window ends, no pending issues can be postponed. In this specific situation, case (a) continuously occurs in the last 18 hours of assessment, thus causing a higher hydrogen withdrawal than needed. Nevertheless, showing such a low residual error (*i.e.* slightly less than 0.06%), the productivity specification is substantially respected.

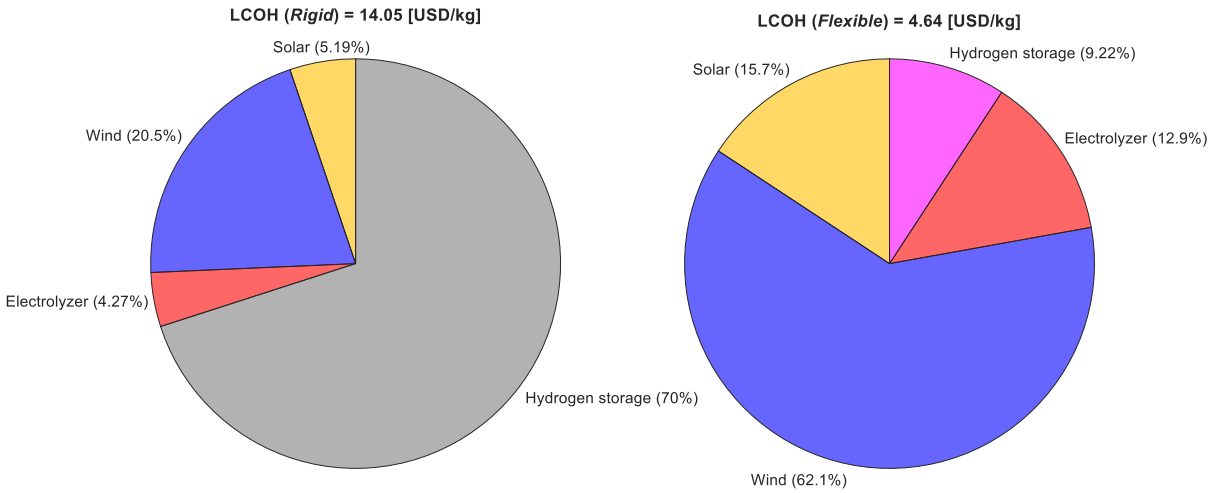

Figure 4.8: Optimal LCOH breakdown for the *Rigid* (left) vs. *Flexible* (right) scenarios.

Hence, based on the results of the case study, our methodology is a beneficial and easy-to-implement tool for minimizing the required hydrogen storage capacity in dynamically operated industrial plants. By doing so, several advantages follow, especially addressing the so-called "three pillars of sustainability" (*i.e.* economic, environmental, and social). To name one for each pillar: higher cost-effectiveness of the resulting plant (*i.e.* saving a conspicuous portion of CapEx and OpEx meant for the storage system if operated rigidly, see **Figure 4.8**); lower cradle-to-grave emissions (due to the reduced handling of resources and manufacturing); improved process safety (as lower storage capacities imply lower hydrogen hold-up, hence lower hazard severity associated with incidental events such as fires and explosions). However, even a few drawbacks follow. Above all, higher operational risks such as insufficient supply during periods of high demand or scarce renewable inputs. Indeed, as already stated

in Section 4.2, this methodology estimates the minimal required capacity of the storage system (*i.e.* m_{tot}). This means its operating regime spans from complete filling to complete emptying over the assessed timespan (having both events occurring at least once). Therefore, in case such operating conditions must always be avoided for technical reasons (*e.g.*, to properly face a potential increase in storage pressures due to high temperatures from hot ambient conditions or to guarantee a safe storage reserve even for unpredictably pejorative scenarios), the resulting capacity must be oversized by a given safety factor (*e.g.*, equal to 10% (EERE, 2001)).

To further verify the consistency of such results, the same optimization routine was applied to the solar and wind profiles recorded in the exact location during the five years preceding 2023 (*i.e.* from 2018 to 2022). This led to a sensitivity analysis investigating the impact of different years (hence different renewable energy availabilities) on the optimal plant design. In this regard, the solar and wind annual capacity factors (*i.e.* the ratios of the actual amount of electricity harvested over the year of reference to the theoretical amount of electricity that could have been produced if the power plant had operated continuously at full power during the same period (NRC, 2023)) are the best metric to assess the extent of renewable energy sources' availability and the attractiveness of a geographical area for renewable power generation. Specifically, all the assessed years show very similar (and relatively high, if compared to the world average (IEA, 2020)) solar and wind power availability, which allows the optimizer to choose between solar and wind power even more unbiasedly. Hence, the renewable park must be sufficiently large to harvest the electric energy required at the electrolyzer yearly, and the hydrogen storage must be sufficiently large to meet the storage demands throughout the plant's operational life.

Accordingly, **Table 4.3** reports the optimal results for each year assessed. First, due to the high hydrogen compression and storage costs, all assessed years show a relatively low hydrogen storage volume (*i.e.* ranging from 12.75 t_{H2}, in 2022, to 34.44 t_{H2}, in 2019) at the expense of larger solar and wind installed capacities. Accordingly, the size of the electrolyzer in each scenario does not differ from the other for more than 150 kW (*i.e.* ca. ±0.25% variability), as it is both constrained by the hydrogen productivity target and tied to the optimal $\underline{\dot{m}}_{IN}^{H_2}$ profile allowing such low storage volumes. Secondly, focusing on the hydrogen hold-up profiles at the storage, they all show similar trends: specifically, severe hydrogen scarcity is usually recorded first around January and February and then around October and November. As such days are the critical factors in determining the capacity of the hydrogen storage (since its goal is precisely to provide hydrogen when the renewable power input is not available), one can consider avoiding operating the storage system during those periods (*e.g.*, by scheduling its shut-down or maintenance and thus deciding to import an equivalent amount of hydrogen directly from other external sources) to reduce its design volume significantly.

Table 4.3: Optimization results from 2018 to 2023.

	Value	Unit	Hydrogen storage hold-up profile
2018			
Solar capacity factor	27.37	%	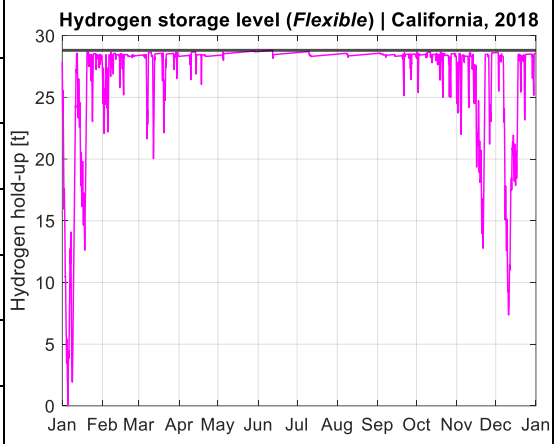
Wind capacity factor	29.62	%	
Solar installed capacity	90	MW	
Wind installed capacity	340	MW	
Electrolyzer size	56.92	MW	
Hydrogen storage size	28.81	t	
LCOH	6.44	USD/kg	
2019			
Solar capacity factor	26.76	%	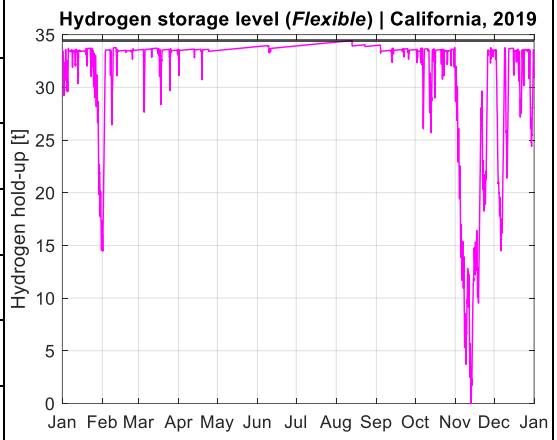
Wind capacity factor	27.06	%	
Solar installed capacity	90	MW	
Wind installed capacity	440	MW	
Electrolyzer size	56.92	MW	
Hydrogen storage size	34.44	t	
LCOH	7.80	USD/kg	
2020			
Solar capacity factor	26.16	%	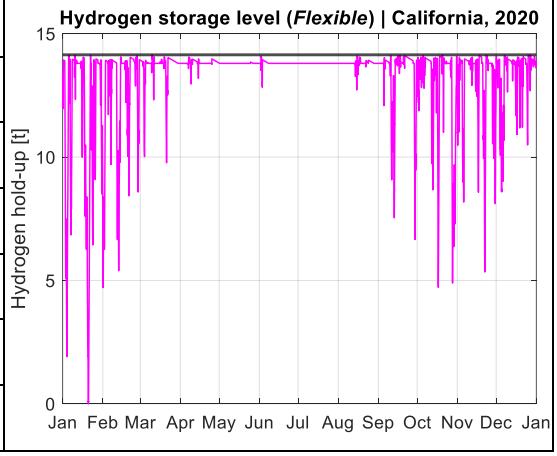
Wind capacity factor	26.82	%	
Solar installed capacity	90	MW	
Wind installed capacity	330	MW	
Electrolyzer size	56.83	MW	
Hydrogen storage size	14.14	t	
LCOH	5.90	USD/kg	

2021		
Solar capacity factor	26.97	%
Wind capacity factor	30.28	%
Solar installed capacity	80	MW
Wind installed capacity	260	MW
Electrolyzer size	56.89	MW
Hydrogen storage size	17.79	t
LCOH	5.06	USD/kg
2022		
Solar capacity factor	27.41	%
Wind capacity factor	26.64	%
Solar installed capacity	70	MW
Wind installed capacity	280	MW
Electrolyzer size	56.98	MW
Hydrogen storage size	12.75	t
LCOH	5.05	USD/kg
2023		
Solar capacity factor	26.64	%
Wind capacity factor	29.61	%
Solar installed capacity	70	MW
Wind installed capacity	240	MW
Electrolyzer size	56.91	MW
Hydrogen storage size	15.09	t
LCOH	4.64	USD/kg

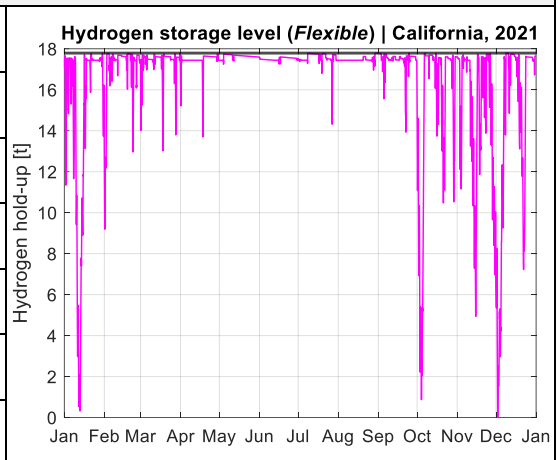

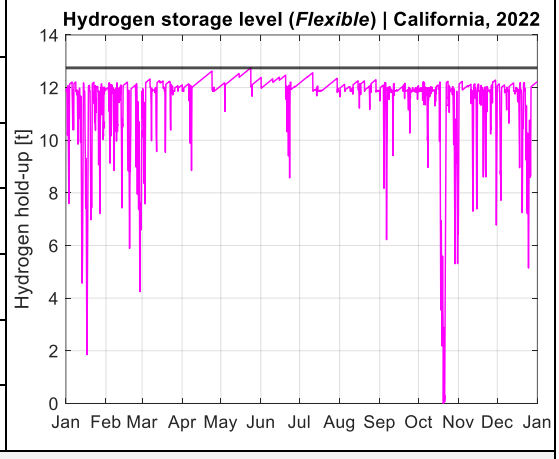

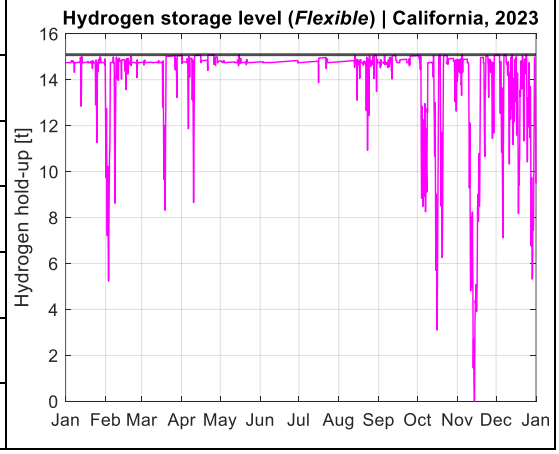

For example, let us consider the 2019 case: though featuring capacity factors not dissimilar to those of the other assessed years, such a scenario led to a significant increase in the optimal LCOH mainly due to the exceptional scarcity of renewable power in the first half of November. This means that, although the amount of renewable power harvested throughout that year of operations was similar to the other

scenarios (leading to comparable capacity factors), its distribution over time (being entirely disregarded by capacity factors) was so uneven that the storage system was significantly stressed. Accordingly, higher renewable installed capacities were required to avoid huge hydrogen storage sizes, hence a higher LCOH. Thus, neglecting the impact of the first half of November would lead to a need for a hydrogen storage capacity of approximately 14.5 t_{H2} lower than the actual one (*i.e.* resulting in ca. 42% savings in design volume and total costs). Under such circumstances, however, the auxiliary hydrogen source must be considered carefully. If "green" (*i.e.* from renewable energy sources), it will not affect the carbon intensity of the process; if not (*e.g.*, "gray" or "brown" (Incer-Valverde *et al.*, 2023), *i.e.* from fossil sources), regulatory limits and environmental considerations should apply. In this regard, it is also worth noting that this optimization problem was carried out under the conservative assumption of no external electric supply to mitigate the unavailability of renewable power (*i.e.* an islanded system with neither grid connection nor own power generation sources). By relaxing such a rigid assumption, the resulting LCOH would drop significantly (especially concerning the decline in required solar and wind installed capacities). Lastly, a further sensitivity analysis was performed regarding the impact of the downstream conversion process (*e.g.*, Haber-Bosch process) flexibility on the optimal hydrogen storage size. Indeed, this is a crucial parameter for the optimization problem since higher process flexibilities extend the applicability of Eq. (4.3), thus theoretically reducing the need for buffer storage.

Table 4.4: Impact of the conversion process turn-down flexibility on the optimization problem (2023 scenario).

Conversion process turn-down flexibility (Max ramp = ±20%/h)	**10%**	**20%**	**30%**	**40%**	**50%**	**60%**	**70%**	**80%**	**90%**
***Solar park* [MW]**	60	60	50	50	50	70	70	50	50
***Wind farm* [MW]**	240	240	250	250	250	240	240	260	340
***Electrolyzer* [MW]**	57.14	57.14	57.12	57.12	57.12	56.91	56.91	56.67	54.48
***Hydrogen storage* [t]**	10.39	7.26	5.62	5.87	6.74	6.92	15.09	28.41	30.18
***LCOH* [USD/kg]**	4.40	4.32	4.28	4.29	4.32	4.41	4.64	5.05	6.03

In this regard, **Table 4.4** reports the optimization results for the 2023 scenario according to different values of maximum allowable turn-down at the conversion process, ranging from 90% to 10% (according to the most flexible solutions commercially available for ammonia synthesis (Genova & Panza, 2022)). As expected, increasing the process flexibility of the downstream conversion process (*i.e.* allowing

severe turn-down conditions) leads to smaller renewable power plants and hydrogen storage capacities. As the turn-down extent progressively broadens from 90% to 30%, both sizes decrease monotonically, and the LCOH behaves accordingly. However, such a trend changes for the 20% and 10% cases, as the hydrogen storage capacity (thus the resulting LCOH) rises again (though the overall renewable installed power still stands at the minimum attained value so far, *i.e.* 300 MW). By analyzing the respective hold-up profiles (see **Figure 4.9**), these deviations seem attributable to the ramping rate constraint, as higher flexibilities allow $\dot{m}_{OUT}^{H_2}(t)$ to oscillate more thus making the ±20%/h requirements even more stringent: so higher oscillations are accompanied by higher sluggishness in the response (stressing the storage system as soon as undesired hydrogen inputs arise abruptly).

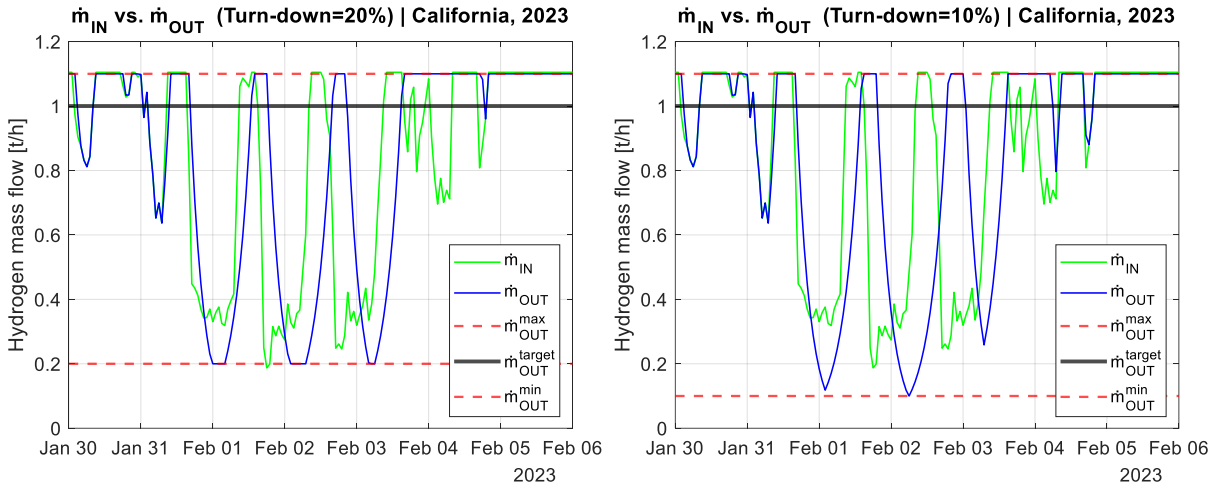

Figure 4.9: Inlet (green) and outlet (blue) hydrogen mass flows for the 20% (left) and 10% (right) turn-down scenarios reported in **Table 4.4** (detail of a week of operations, *i.e.* from January 30th to February 5th, 2023).

In confirmation of this interpretation, by accepting much higher ramping rates (*i.e.* ±100%/h, according to the most flexible solutions commercially available for ammonia synthesis (Genova & Panza, 2022)), a strictly monotonically decreasing trend in the LCOH is observed for all the scenarios from 90% to 10% turn-down (see **Table 4.5**). Comparing **Table 4.5** to **Table 4.4**, the sensitivity to the maximum ramping rate is higher when the process flexibility increases since higher flexibility implies much more ramping. Indeed, the optimal configuration for the 90% turn-down case (*i.e.* the least flexible one) is the same for the ±20%/h and ±100%/h constraints; conversely, if broadening the allowable turn-down extent (*i.e.* increasing the downstream process' flexibility), the hydrogen storage (hence the LCOH) benefits from remarkable savings when considering ±100%/h instead of ±20%/h. Therefore, **Table 4.4** highlights a limit of the proposed criterion, *i.e.* its incapability to determine *a priori* if larger flexibility constraints would improve the storage size and thus the overall process (*e.g.*, due to the ±20%/h ramp constraint assessed in **Table 4.4**, operating with a 10% turn-down

extent would have sensibly increased the required storage size, hence the LCOH, compared to the less flexible 20% turn-down scenario).

Table 4.5: Impact of the conversion process maximum ramping rates on the optimization problem (2023 scenario).

Conversion process turn-down flexibility (Max ramp = ±100%/h)	**10%**	**20%**	**30%**	**40%**	**50%**	**60%**	**70%**	**80%**	**90%**
***Solar park* [MW]**	50	50	50	50	50	70	70	50	50
***Wind farm* [MW]**	250	250	250	250	250	240	240	260	340
***Electrolyzer* [MW]**	57.12	57.12	57.12	57.12	57.12	56.91	56.91	56.67	54.48
***Hydrogen storage* [t]**	2.39	2.94	3.98	5.29	6.69	6.20	14.71	28.21	30.18
***LCOH* [USD/kg]**	4.19	4.21	4.24	4.28	4.32	4.39	4.63	5.04	6.03

Accordingly, it is suggested that more flexibility ranges be assessed through basic sensitivity analyses before determining the ultimate design capacity of the flexible storage system. This also leaves room for future research on the proposed algorithm, such as enabling it to autonomously identify the best flexibility ranges leading to the minimum size (or expense) configuration. However, this feature would necessarily call for improving the computational structure and calculation efficiency, whose present simplicity makes it a practical turnkey tool.

4.4. Conclusions

This chapter introduced, described, validated, and discussed a simple and general method for evaluating the optimal delivery policy, (time)step-by-(time)step, of dynamically operated material storage systems to minimize the required capacity to be installed. Remarkably, the proposed method calls for one input data: the inlet mass flow as a function of time. It meets full compliance with multiple supply specifications usually required by downstream uses, such as target productivity, ramping rates, and load flexibility constraints. Also, being a numerically explicit method based on simple mathematical operations, it requires little effort to be implemented and a short computational time to be run, hence taking the form of a handy shortcut method for designing flexible material storage systems. Ultimately, a case study aimed to optimize the production and storage of green hydrogen from renewables successfully validated said methodology and stressed the importance of flexibility in developing sustainable production processes. More specifically, our flexible criterion led to hydrogen storage size savings of over 90% higher than those resulting from steady-state withdrawal

policies. Consequently, this also improved the corresponding optimal LCOH values, spanning from 4.19 to 6.03 USD/kg according to the flexibility ranges enabled by the downstream process. The proposed algorithm may help researchers and stakeholders in designing and techno-economically assessing manufacturing plants featuring a material storage system: *e.g.*, Power-to-X processes, whose flexible operation is critical for their economic competitiveness compared to conventional (but carbon-intensive) process alternatives.

5 Flexible electricity storage

Introductory comment

The counterpart of mass accumulation is energy accumulation. Therefore, after having extensively addressed the former (*i.e.* hydrogen storage), the line of research moved on to the latter, namely electrical storage (*i.e.* batteries). Indeed, Battery Energy Storage Systems (BESSs) are gaining industrial interest to increase the flexibility of renewable-energy-powered plants, representing a reservoir of electricity to be drawn whenever the generation from renewables is insufficient to power the process (*e.g.*, electrolysis). Generally placed amidst the renewable power plant and the electrolyzer, BESSs were the subject of a detailed study to develop a design criterion to minimize their size and hence the costs. Once again, the proposed approach aimed to establish an optimal dynamic withdrawal strategy of practical utility for design and process engineers.

The present chapter stems from:

A framework for the design of battery energy storage systems in Power-to-X processes

Isella, A., & Manca, D.

Journal of Energy Storage, 2025, 123, 116744

DOI: https://doi.org/10.1016/j.est.2025.116744

Abstract

Energy storage has become increasingly crucial as more industrial processes rely on renewable power inputs to achieve decarbonization targets and meet stringent environmental standards. Storage systems are essential for mitigating the fluctuations in plant operations that result from the discontinuity of renewables, allowing for a smooth reconciliation of renewable power with the steadiness of the process. This chapter introduces a simple and general framework to identify the optimal delivery policies minimizing the capacity of battery energy storage systems in Power-to-X processes. The main novelty of this framework lies in its rigorous mathematical formulation, which converts the inherently fluctuating electric power availability from renewable sources into an optimally scheduled electric power output. In this way, the required storage capacity is minimized, while also meeting various operating requirements, such as ramping rates and load flexibility constraints. Lastly, this chapter assesses a case study based on the design optimization of a solar- and wind-powered industrial facility for green hydrogen production to validate and show the framework's effectiveness.

5.1. Introduction

As the decarbonization of the chemical industry (and the manufacturing sector as a whole) demands increasing reliance on renewable energy, adaptation problems to such inherently discontinuous energy sources are urgently pressing. The fluctuating nature of renewables calls for processes to operate flexibly according to the intermittent availability of electricity and raw materials. However, many process units are not flexible enough to withstand such heavy discontinuities. Hence, storage systems are required to mitigate them and ensure viable operating regimes. In this regard, storage systems may refer to mass or energy accumulation. In the case of mass, storage systems typically consist of tanks and vessels providing/accumulating raw materials or (intermediate) products. In the case of energy, the nature of the storage system strictly depends on the form of energy. Precisely, standard storage technologies nowadays involve thermal, mechanical, chemical, or electrochemical energy (by even combining them in some cases) (Amir *et al.*, 2023). For instance, thermal energy storage may call for diathermic fluid circuits, such as molten salts in concentrating solar power plants (Prieto *et al.*, 2024), or air in several thermo-mechanical storage solutions, such as liquid air- (Vecchi *et al.*, 2021) or advanced compressed air-energy storage (Zhang *et al.*, 2024). Conversely, electrical energy storage generally requires a battery energy storage system (BESS) (Rey *et al.*, 2023). Specifically, utility-scale battery systems typically show storage capacities ranging from a few to hundreds of megawatt-hours. Among the battery storage technologies developed recently, lithium-ion, sodium-sulfur, and lead-acid batteries are known to be the most commonly used (IRENA, 2019). In particular, over the last few years, most market growth has been seen in

lithium-ion batteries due to their steadily declining production costs. Also, a new boost is now addressing solid-state batteries, showing comparable cost and superior electrochemical performances to commercial nonaqueous lithium-ion batteries (Li, 2023), together with the technologies aiming to replace rare metals (*e.g.*, cobalt and nickel, but even lithium such as in the case of sodium-ion batteries) and thus reduce the economic dependence on those few countries owning the monopoly for their supply.

This chapter focuses on Power-to-X processes (see **Figure 5.1**), *i.e.* synthetic pathways in which the final product "X" (*e.g.*, hydrogen, ammonia, methanol, *etc.*) derives from renewable energy sources (hence totally or nearly carbon-free) (Mucci *et al.*, 2023b). This class of processes (also known in chemical engineering as Power-to-Chemicals) mainly involves, by way of "intermittency-mitigating" features, either a battery right amidst the renewable park harvesting the "green" electricity and the electrolyzer producing the "green" hydrogen required for the conversion process (*i.e.* the chemical plant) or a hydrogen storage tank between the electrolyzer and the conversion process (combinations of such two options are also viable (Mucci *et al.*, 2023a; Osman *et al.*, 2020)). As we have extensively discussed the issues affecting hydrogen storage systems in the previous chapter (Isella & Manca, 2025b), in which we propose a general criterion for the optimal design of dynamically operated storage tanks, we will now focus on battery electric storage systems.

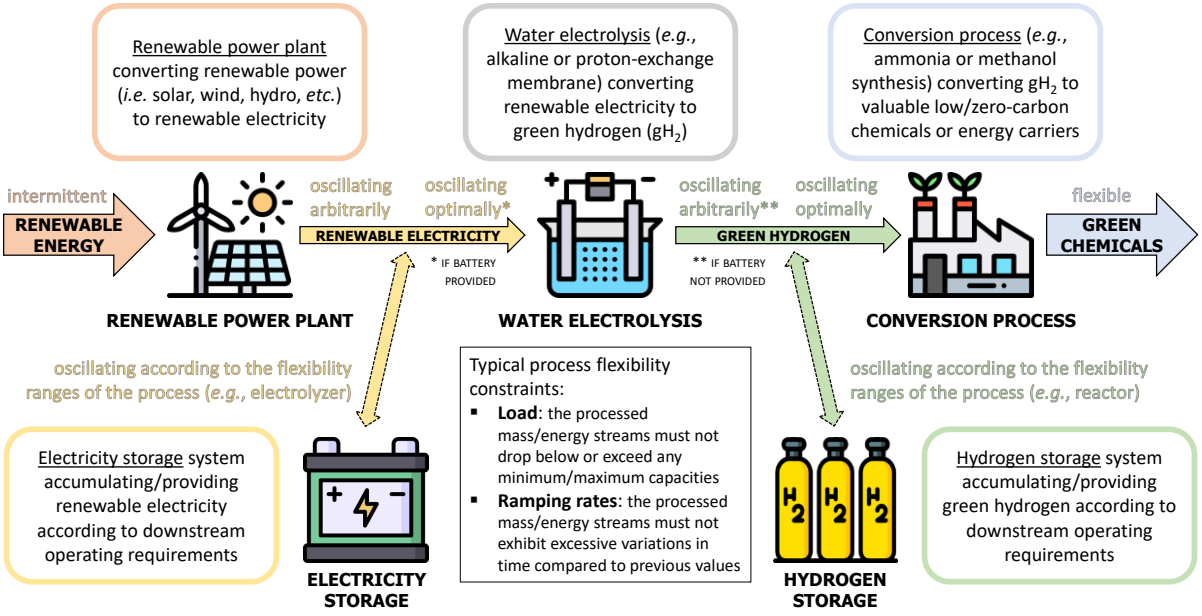

Figure 5.1: Typical scheme of a Power-to-X (applied to a Power-to-Chemicals) process. Electricity or hydrogen storage (or both) is needed to mitigate the intermittencies from renewable energy sources.

Precisely, the scope and novelty of this chapter are to develop a framework to identify the dynamically optimal electric power delivery schedule that minimizes the capacity of a battery storage system (in terms of both capital and operating expenditures) and

complies with multiple supply specifications according to the downstream conversion process (*e.g.*, ramping rates, load flexibility constraints, grade changes, servo and regulator problems, *etc.*). To our knowledge, no similar methodologies have ever been proposed in scientific literature to approach such an increasingly widespread problem. Indeed, suboptimal designs of this kind of process units (whose average installation costs, though continuously decreasing, now stand at ca. 300-350 USD/kWh (Mucci *et al.*, 2023a; Marocco *et al.*, 2024)) would lead to as severe as avoidable surges in the production cost of the resulting green chemicals.

The chapter is structured as follows: Section 5.2 presents the sizing methodology based on the mathematical model of a conventional BESS; Section 5.3 validates the resulting framework with a practical case study, *i.e.* an industrial facility producing green hydrogen from both solar and wind power sources, and discusses the results. Section 5.4 summarizes the conclusions.

5.2. Mathematical model

Our sizing criterion aims to minimize the size of battery energy storage systems through a suitable electric power delivery policy. Hence, the following discussion considers an elementary battery storage system like the one depicted in **Figure 5.2**.

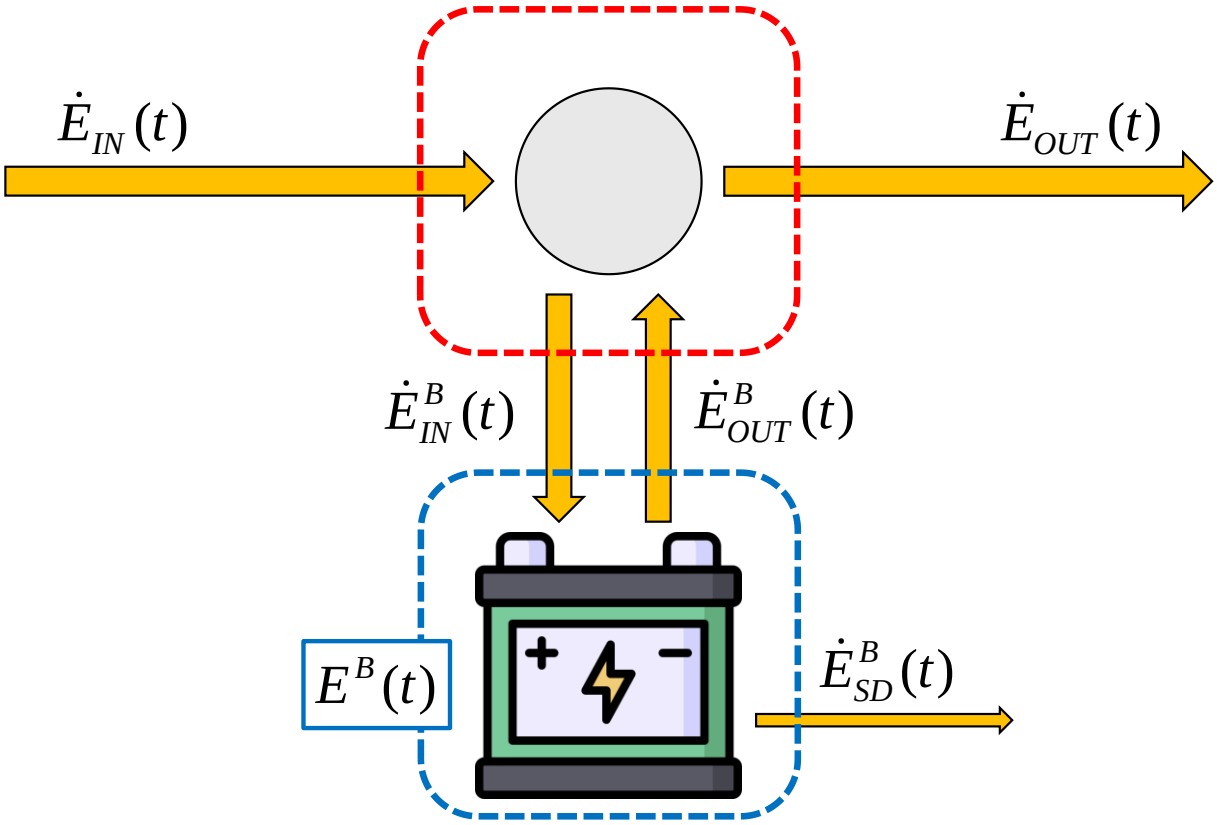

Figure 5.2: The system and control volumes described by the mathematical model, *i.e.* the "storage node" (*e.g.*, a switching station, enclosed in the red-dashed box) and the battery (enclosed in the blue-dashed box).

The general energy balance for the storage node (*i.e.* the red control volume in **Figure 5.2**: *e.g.*, a switching station) under steady-state conditions is:

$$\dot{E}_{IN}^{B}(t) - \dot{E}_{OUT}^{B}(t) = \dot{E}_{IN}(t) - \dot{E}_{OUT}(t) \tag{5.1}$$

Where $\dot{E}_{IN}(t)$ is the (given) amount of electric power conveyed to the storage node while $\dot{E}_{OUT}(t)$ is the unknown amount of electric power fed to the downstream process (*e.g.*, an electrolyzer), which we aim to evaluate (time)step-by-(time)step in such a way to minimize the battery storage capacity. $\dot{E}_{IN}^{B}(t)$ and $\dot{E}_{OUT}^{B}(t)$ are the inlet and outlet electric powers of the battery system, respectively.

Conversely, the general energy balance for the battery (*i.e.* the blue control box in **Figure 5.2**) is:

$$\frac{d}{dt}E^{B}(t) = \eta_{C} \cdot \dot{E}_{IN}^{B}(t) - \frac{1}{\eta_{D}} \cdot \dot{E}_{OUT}^{B}(t) - \dot{E}_{SD}^{B}(t) \tag{5.2}$$

Where η_{C} and η_{D} are the charging and discharging efficiencies, which our model considers constant, disregarding any dependence on the electric current and the battery's charge. $E^{B}(t)$ is the electrical energy stored within the battery and $\dot{E}_{SD}^{B}(t)$ denotes the corresponding power losses due to the self-discharge rate (σ_{SD}). Specifically, the latter can be expressed as:

$$\dot{E}_{SD}^{B}(t) = E^{B}(t) \cdot \sigma_{SD} \tag{5.3}$$

However, as $\dot{E}_{SD}^{B}(t)$ makes the handling of Eq. (5.2) sensibly more complicated and is generally much smaller than the other two terms (*e.g.*, in lithium-ion type batteries, self-discharge rates are typically around 0.15-0.20 %/day (Mucci *et al.*, 2023a; Marocco *et al.*, 2024)), it will be after this neglected for the derivation of the dynamic delivery criterion (which makes the calculations explicit and therefore more manageable) and accounted only *a posteriori* in the estimation of the storage capacity (consequently, we will verify the validity of such an approximation in the case study of Section 5.3).

Accordingly, the simplified energy balance of the battery can be rewritten as:

$$\frac{d}{dt}E^{B}(t) = \eta_{C} \cdot \dot{E}_{IN}^{B}(t) - \frac{1}{\eta_{D}} \cdot \dot{E}_{OUT}^{B}(t) \tag{5.4}$$

Now, the operation mode of a battery storage system can be partitioned into (i) charging (*i.e.* when it must retain part of $\dot{E}_{IN}(t)$, as it is too high) and (ii) discharging (*i.e.* when it must provide some electric power to supplement $\dot{E}_{IN}(t)$, as it is too low).

By referring to Eqs. (5.1) and (5.4), for charging case (i), the following relations hold:

Case (i) : charging

$$\text{if } \dot{E}_{IN}(t) - \dot{E}_{OUT}(t) \geq 0 \tag{5.5}$$

$$\begin{cases} \dot{E}^{B}_{IN}(t) = \left|\dot{E}_{IN}(t) - \dot{E}_{OUT}(t)\right| & \text{(a)} \\ \dot{E}^{B}_{OUT}(t) = 0 & \text{(b)} \\ \dfrac{d}{dt}E^{B}(t) = \eta_{C} \cdot \left|\dot{E}_{IN}(t) - \dot{E}_{OUT}(t)\right| & \text{(c)} \end{cases}$$

Note that case (i) also includes the limit case of $\dot{E}_{IN}(t)$ equal to $\dot{E}_{OUT}(t)$ (*i.e.* no accumulation).

Conversely, discharging case (ii) is described by the following relations:

Case (ii) : discharging

$$\text{if } \dot{E}_{IN}(t) - \dot{E}_{OUT}(t) < 0 \tag{5.6}$$

$$\begin{cases} \dot{E}^{B}_{IN}(t) = 0 & \text{(a)} \\ \dot{E}^{B}_{OUT}(t) = \left|\dot{E}_{IN}(t) - \dot{E}_{OUT}(t)\right| & \text{(b)} \\ \dfrac{d}{dt}E^{B}(t) = -\dfrac{1}{\eta_{D}} \cdot \left|\dot{E}_{IN}(t) - \dot{E}_{OUT}(t)\right| & \text{(c)} \end{cases}$$

As our proposed criterion aims to identify the most suitable $\dot{E}_{OUT}(t)$ values capable of minimizing the battery storage capacity, the main goal is to reduce as far as possible the accumulation term of the battery in such an ideal way that:

$$\frac{d}{dt}E^{B}(t) \to 0 \tag{5.7}$$

According to Eqs. (5.5) and (5.6), it follows that Eq. (5.7) holds if and only if:

$$\dot{E}_{OUT}(t) = \dot{E}_{IN}(t) \tag{5.8}$$

However, there are many cases/situations in which we cannot make the outlet electric power equal to the inlet one. Namely: (A) when $\dot{E}_{OUT}(t)$ falls below the minimum value of electric power allowed downstream; (B) when $\dot{E}_{OUT}(t)$ exceeds the maximum value of electric power allowed downstream; (C) when $\dot{E}_{OUT}(t)$ does not meet some required/suggested bumpless implementation (*e.g.*, a specific allowed ramping rate) of the output power such as ±X% variations at most as against either previous values or assigned maximum deviations. When these circumstances occur, the BESS must hold/release the absolute difference between the inlet and the (constrained) outlet currents. To account for these occurrences (and then to minimize the resulting

accumulation whenever possible, both to fully satisfy the downstream demand and curtail the required battery storage capacity), an additional term is introduced, which acts as a "memory" of the limitations encountered so far in applying Eq. (5.8):

$$\dot{E}_{OUT}(t)=\begin{cases}\dot{E}_{IN}(t)+\left[\eta_D\cdot\sum_{\tau=1}^{t-1}\left(\frac{d}{dt}E^B(\tau)\right)\right] & \text{if } \sum_{\tau=1}^{t-1}\left(\frac{d}{dt}E^B(\tau)\right)\geq 0 \quad \text{(a)}\\ \dot{E}_{IN}(t)+\left[\frac{1}{\eta_C}\cdot\sum_{\tau=1}^{t-1}\left(\frac{d}{dt}E^B(\tau)\right)\right] & \text{if } \sum_{\tau=1}^{t-1}\left(\frac{d}{dt}E^B(\tau)\right)<0 \quad \text{(b)}\end{cases} \tag{5.9}$$

Once again, as two different processes are involved, a distinction is necessarily drawn between discharging (when positive) and charging (when negative) the residual accumulation associated with the battery. In this regard, each summation term can be quickly evaluated by previous values of $\underline{\dot{E}}_{IN}$ and $\underline{\dot{E}}_{OUT}$, according to Eqs. (5.5) and (5.6). Therefore, Eq. (5.9) makes the proposed criterion an explicit method.

Consequently, the resulting $\dot{E}_{OUT}(t)$ should be checked to guarantee that it complies with the aforementioned (A), (B), and (C) cases. If yes, it can be imposed as it is; if not, it should be replaced by the closest allowed value (*i.e.* the one meeting either the lower or upper limits according to the downstream constraints). Furthermore, since the first element of $\underline{\dot{E}}_{OUT}$ cannot be estimated from Eq. (5.9) (being $(t-1)$ the upper bound of the summation), such a value is specially assigned ahead of the rest: if $\dot{E}_{IN}(1)$ falls within the allowed electric power range that can be provided downstream (according to the process specifications), $\dot{E}_{OUT}(1)$ shall match it; if $\dot{E}_{IN}(1)$ is higher/lower than the maximum/minimum allowed load, $\dot{E}_{OUT}(1)$ shall coincide with such a maximum/minimum value. Hence, falling either into case (i) or (ii) (*i.e.* Eqs. (5.5) and (5.6) respectively), the corresponding accumulation rate term can be evaluated accordingly and thus provided to Eq. (5.9) to initialize the iterative procedure.

By way of illustration, here follows the MATLAB source code that implements numerically the proposed framework (as for the notation used so far in the equations above, it is worth noting that MATLAB array indexing starts from 1 instead of 0):

Algorithm 5.1: BESS sizing framework

```
function E_out = BESS_size(E_in,E_MIN,E_MAX,rampL,rampU,etaC,etaD)
% Pre-allocation vector for E_out
E_out = zeros(1,length(E_in)); %[MW]
% Assigning E_out(1) ahead of the rest:
if E_in(1) <= E_MIN %[MW]
    E_out(1) = E_MIN; %[MW]
elseif E_in(1) >= E_MAX %[MW]
    E_out(1) = E_MAX; %[MW]
else
    E_out(1) = E_in(1); %[MW]
```

```
11:   end
12:   % Pre-allocation vectors for Eb_in, Eb_out, and dEb_dt
13:   Eb_in = zeros(1,length(E_in)); %[MW]
14:   Eb_out = zeros(1,length(E_in)); %[MW]
15:   dEb_dt = zeros(1,length(E_in)); %[MW]
16:   % Computing all the other values of E_out(t):
17:   for t = 2:length(E_in)
18:       % Eqs. (5.5) and (5.6):
19:       if E_in(t-1)-E_out(t-1) >= 0 %[MW]
20:           % Case (i): charging the battery
21:           Eb_in(t-1) = abs(E_in(t-1)-E_out(t-1)); %[MW]
22:           Eb_out(t-1) = 0; %[MW]
23:       else
24:           % Case (ii): discharging the battery
25:           Eb_in(t-1) = 0; %[MW]
26:           Eb_out(t-1) = abs(E_in(t-1)-E_out(t-1)); %[MW]
27:       end
28:   dEb_dt(t-1) = etaC*Eb_in(t-1)-(1/etaD)*Eb_out(t-1); %[MW]
29:   SUM = sum(dEb_dt(1:t-1)); %[MW]
30:       % Eqs. (5.9):
31:       if SUM >= 0 %[MW]
32:           % Discharge the (positive) residual battery accumulation
33:           E_out(t) = E_in(t) + etaD*SUM; %[MW]
34:       else
35:           % Charge the (negative) residual battery accumulation
36:           E_out(t) = E_in(t) + (1/etaC)*SUM; %[MW]
37:       end
38:       % Check the Ramp bounds
39:       if E_out(t-1) ~= 0 %[MW]
40:           E_out(t) = min(E_out(t),(1+rampU)*E_out(t-1)); % Upper bound
41:           E_out(t) = max(E_out(t),(1-rampL)*E_out(t-1)); % Lower bound
42:       end
43:   % Check the Output bounds
44:   E_out(t) = min(E_out(t),E_MAX); % Output upper bound
45:   E_out(t) = max(E_out(t),E_MIN); % Output lower bound
46:   end
47:   end
```

Finally, after having evaluated the optimal delivery schedule (*i.e.* $\underline{\dot{E}}_{OUT}$), the hold-up profile of the energy stored by the battery can be easily computed step-by-step by numerically integrating the corresponding battery accumulation terms (that can be

calculated for each time step just through the corresponding values of $\dot{E}_{IN}(t)$ and $\dot{E}_{OUT}(t)$, according to conditions (i) or (ii)):

$$E_0^B(t) = \sum_{\tau=1}^{t} \left(\frac{d}{dt} E^B(\tau) \right) \Delta t \tag{5.10}$$

Integration is performed through a Riemann sum due to the typically piecewise constant data profiles considered in those temporally discretized problems. In contrast, referring to other numerical integration techniques such as Bezout's (*i.e.* trapezoidal) or Simpson's (*i.e.* parabolic) formulae might likely introduce numerical artifacts to the original data. However, as Eq. (5.10) may provide negative hold-up values and the energy stored within the battery must necessarily be non-negative (*i.e.* $\forall E^B(t) \in \mathbb{R}_{\geq 0}$), $E_0^B(t)$ shall be adjusted accordingly:

$$E^B(t) = E_0^B(t) - \min\left(\underline{E}_0^B\right) \tag{5.11}$$

Hence, the (minimum) required battery storage capacity is equal to:

$$E_{\text{tot}}^B = \max\left(\underline{E}_0^B\right) - \min\left(\underline{E}_0^B\right) = \max\left(\underline{E}^B\right) \tag{5.12}$$

Once the required BESS size is determined, its capital and operating expenditures can be evaluated accordingly. It is worth stressing that such a criterion, whose core novelty primarily lies in Eq. (5.9), allows the estimation of $\underline{\dot{E}}_{OUT}$ (*i.e.* the vector of the electric power to be delivered downstream) and E_{tot}^B just from $\underline{\dot{E}}_{IN}$ (*i.e.* the vector of the electric power input) and the characteristic parameters of the battery (*i.e.* its charging and discharging efficiencies). Therefore, no further bits of information are required. Now, let us focus on the device self-discharging phenomenon, which has been neglected so far in sizing the battery. As Eq. (5.11) provides the electricity hold-up profile, Eq. (5.3) allows estimating the corresponding self-discharge losses. Hence, to understand how to face them properly during the operation of the battery, we can now refer to the discrete solution of Eq. (5.2) and add a term that allows counteracting the self-discharge losses:

$$E^B(t) = E^B(t-1) \cdot \left(1 - \sigma_{SD}\right) \cdot \Delta t + \eta_C \cdot \dot{E}_{IN}^B(t) \cdot \Delta t - \frac{1}{\eta_D} \cdot \dot{E}_{OUT}^B(t) \cdot \Delta t + \eta_C \cdot E_{\text{add}}(t) \tag{5.13}$$

Specifically, such a term considers an additional electric power input ($E_{\text{add}}(t)$) that depends on the electricity source the battery can rely on:

$$\dot{E}_{\text{add}}(t) = \begin{cases} \dfrac{E^B(t-1) \cdot \sigma_{SD}}{\eta_C} & \text{if } \dot{E}_{\text{add}} \text{ from Grid } (\dot{E}_{\text{grid}}) \quad \text{(a)} \\ \min\left(\dot{E}_{\text{curt}}(t) \cdot \Delta t, \dfrac{E_{\text{tot}}^B - E^B(t-1)}{\eta_C} \right) & \text{if } \dot{E}_{\text{add}} \text{ from Curtail } (\dot{E}_{\text{curt}}) \quad \text{(b)} \end{cases} \tag{5.14}$$

Eq. (5.14) makes a distinction between the case of electricity supply from the grid, which always allows integrating self-discharge losses *in toto* at any time step, and from

curtailment (*i.e.* the electric power surplus that is typically achieved in renewable-powered systems), which restores the self-discharge losses as much as it can (*i.e.* according to the current availability of excess power). Note that, while relying on the grid always allows equalizing the losses due to the battery self-discharge, conversely relying on curtailed power only does not. Indeed, the curtailed power made available by the renewable park during the assessed timespan might be insufficient to counteract such a phenomenon: if this is the case, the hold-up profile resulting from Eq. (5.13) will become negative in at least one occurrence and, since that behavior is not acceptable, the "first-guess" E^B_{tot} must be increased iteratively until this condition does not occur anymore (*i.e.* until the minimum of the corresponding hold-up profile is positive, hence $\forall E^B(t) \geq 0$). In some cases, it might also happen that even increasing E^B_{tot} does not solve the problem: this occurs when the curtailed power is so scarce or absent (at least for a certain extent of the assessed timespan) that it is not possible to rely on curtailed power only to counteract the self-discharge phenomenon (*i.e.* there is no solution unless an auxiliary supply system from the electric grid is provided).

5.3. Case study

A practical case study allows the validation of the proposed framework. Namely, a solar-and-wind-powered green hydrogen production facility located in California, USA, with a nominal capacity of 1 t_{H2}/h. The choice fell on such a geographical location since a comprehensive collection of renewable power generation data is currently available by CAISO, the California Independent System Operator (CAISO, 2024), featuring one of the world's largest and most modern power grids with high renewable integration. Our system is assumed to be like the one previously shown in **Figure 5.1**, although limited to the green hydrogen generation section featuring the renewable power plant and the electrolyzer only, with an intermediate storage system. Conversely, no downstream conversion processes or other final users are included within the control volume. To validate our framework, the intermediate storage system will consist of a BESS, placed amidst the renewable power plant and the electrolyzer, as the latter (an alkaline type) must continuously be operated at ranges between 10% and 100% of its nominal capacity (McPhy, 2023). Indeed, alkaline electrolyzers show strict minimum loads primarily due to safety reasons: above all, the volume fraction of hydrogen in the oxygen. Indeed, decreasing current densities makes the oxygen production rate slower than the hydrogen crossover rate. Therefore, operating at lower loads leads to higher values of such a key parameter (de Groot *et al.*, 2022). Furthermore, a BESS may also assist in satisfying possible bumpless requirements in operating the electrolyzer (even though, most of the time, both nominal ramp-up and ramp-down limitations of those units are already sufficiently fast to deal with renewable power inputs (Armijo & Philibert, 2020)). Consequently, our criterion may help find the smallest battery storage capacity needed to process the

renewable energy input profile and feed it to the electrolyzer accordingly. **Figure 5.3** reports the case study's process scheme and control volume.

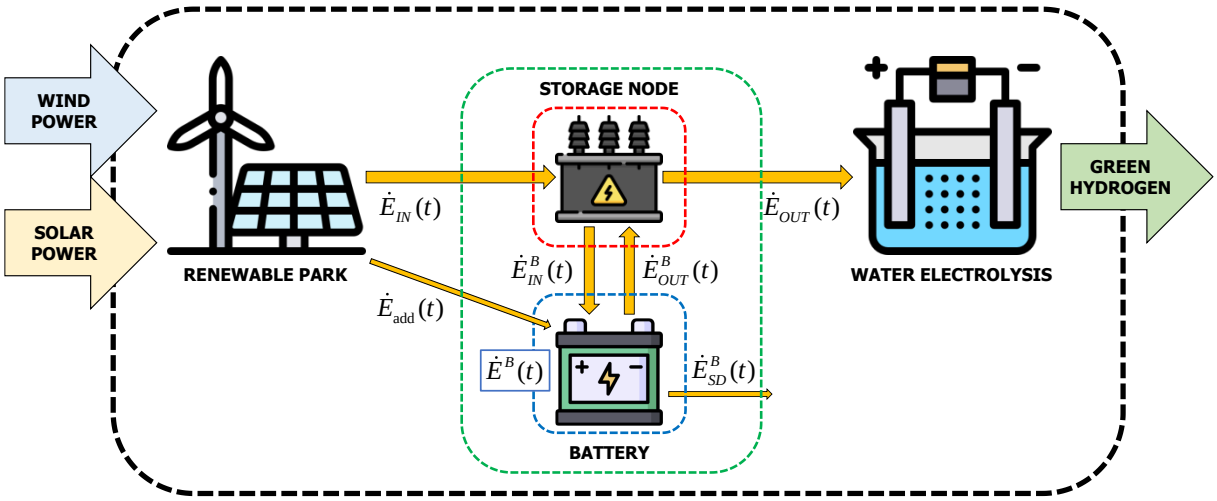

Figure 5.3: Process scheme and control volume (dashed black rectangle) of the green hydrogen production plant of the case study.

As we aim to identify the economically optimal design (*i.e.* minimizing the levelized cost of hydrogen, LCOH), we must solve an optimization problem that determines the best sizes of the renewable power plant, the electrolyzer, and the battery storage. Similar to the optimization procedure presented and discussed in (Isella & Manca, 2024), the one implemented herein investigates different solar and wind installed capacities (*i.e.* the degrees of freedom) and provides as input data renewable power profiles that call for some corresponding electrolyzer and BESS sizes subjected to the operating constraints. Eq. (5.15) summarizes the optimization problem:

$$
\begin{cases}
\underset{P^{S}_{\text{inst}},P^{W}_{\text{inst}}}{\textbf{Min}} \left[LCOH = \dfrac{\sum\limits_{j=S,W,E,B} (CapEx_y + OpEx)_j}{8760 \cdot \dot{m}^{H_2}_{\text{target}}} \right] \\
\text{s.t.:} \\
\dot{E}_{IN}(t) = \min(\dot{E}^{S}(t) + \dot{E}^{W}(t), P^{E}_{\text{inst}}) \quad \text{(a)} \\
\dot{E}_{OUT}(t) \text{ from Eq. (5.9)} \quad \text{(b)} \\
\sum\limits_{\tau=1}^{8760} \dot{E}_{OUT}(\tau) = 8760 \cdot \dot{E}^{E}_{\text{target}} \quad \text{(c)} \\
\dot{E}_{\text{add}}(t) \text{ from Eq. (5.14b)} \quad \text{(d)}
\end{cases}
\tag{5.15}
$$

Where P^{S}_{inst}, P^{W}_{inst}, and P^{E}_{inst} are the installed capacities of the solar farm, wind farm, and electrolyzer, respectively; $\left(CapEx_y + OpEx\right)_{S,W,E,B}$ are the sum of the annualized capital

expenditures ($CapEx_y$) and the annual operating expenditures ($OpEx$) of the solar farm, wind farm, electrolyzer, and battery storage system, respectively; 8760 (h) is the timespan assessed (*i.e.* one year, assuming no maintenance breaks or emergency shutdowns occur); $\dot{E}^S(t)$ and $\dot{E}^W(t)$ are the instantaneous renewable power delivered by the solar and wind farms, respectively (depending on the solar and wind total installed capacity); lastly, $\dot{E}^E_{\text{target}}$ is the electric power that the electrolyzer needs to operate at the nominal hydrogen production rate $\dot{m}^{H_2}_{\text{target}}$ (*i.e.* 1 t_{H2}/h). With regards to the equality constraints: (5.15a) $\dot{E}_{IN}(t)$ equals the overall (*i.e.* both solar and wind) generated renewable electricity but bounded above by the installed capacity of the electrolyzer (*i.e.* what exceeds such a threshold is curtailed); (5.15b) $\dot{E}_{OUT}(t)$ is evaluated applying Eq. (5.9), *i.e.* through our design criterion; (5.15c) the amount of renewable energy fed to the electrolyzer throughout the whole year must be equal to the electricity needed to meet the hydrogen productivity target; and (5.15d) self-discharge losses are counteracted by relying on curtailed power only (*i.e.* auxiliary electricity supply from the electric grid is not an option, which means we assume it is not available in line with the conservative approach to engineering design). In this regard, **Table 5.1** reports all the techno-economic specifications used as input data by the optimization procedure.

Table 5.1: Techno-economic input data for the optimization problem.

	Value	**Unit**	**Reference**
Interest rate	5	%	Mucci *et al.* (2023a)
Solar (Photovoltaics)			
Capacity factor	26.64	%	CAISO (2024)
CapEx	1119	USD/kW	IRENA (2023)
OpEx	1.70	% CapEx/y	Armijo and Philibert (2020)
Life	25	y	Armijo and Philibert (2020)
Wind (Onshore)			
Capacity factor	29.66	%	CAISO (2024)
CapEx	1285	USD/kW	IRENA (2023)
OpEx	2	% CapEx/y	Armijo and Philibert (2020)
Life	25	y	Armijo and Philibert (2020)

Battery (Lithium-ion)			
Charging efficiency	95	%	Marocco *et al.* (2024)
Discharging efficiency	95	%	Marocco *et al.* (2024)
Self-discharge rate	0.007	%/h	Marocco *et al.* (2024)
CapEx	310	USD/kWh	Mucci *et al.* (2023a)
OpEx	2	% CapEx/y	Marocco *et al.* (2024)
Life	10	y	Marocco *et al.* (2024)
Electrolyzer (Alkaline)			
Electricity consumption	4.65	kWh/Nm^3_{H2}	McPhy (2023)
Minimum power	10	% Rated power	ThyssenKrupp (2022)
Maximum power	100	% Rated power	ThyssenKrupp (2022)
Ramp-up	5	%/s	McPhy (2023)
Ramp-down	20	%/s	McPhy (2023)
CapEx	700	USD/kW	Isella *et al.* (2024)
OpEx	2	% CapEx/y	Armijo and Philibert (2020)

Hence, the optimization problem is solved by implementing a grid-search minimization routine on MATLAB R2024a and targeting an investigation region with installed solar and wind capacities ranging from 0 to 300 MW.

Figure 5.4 displays the main optimization results: Panel A shows the objective function (*i.e.* LCOH) as defined in Eq. (5.15) (in white, the infeasible region: *i.e.* those process configurations lacking sufficient installed power generation capacities to meet the hydrogen productivity constraint), while Panel B reports the renewable energy production (*i.e.* at the solar and wind farms) and consumption (*i.e.* at the electrolyzer) profiles of the optimal configuration (*i.e.* the minimum point in Panel A, as it minimizes the LCOH). Precisely, the winning configuration attains an LCOH of 2.92 USD/kg and calls for solar and wind installed capacities of 50 MW and 150 MW, respectively; an electrolyzer capacity of 69.88 MW; and a BESS capacity of 28.20 MWh. The resulting curtailed electrical power amounts to 10.54% of the total generation. The minimum of the LCOH objective function lies just before the unfeasibility region (although not precisely on the border), as the CapEx and OpEx of both the solar and

the wind farms represent the highest values of those reported in **Table 5.1**. On the other hand, higher amounts of renewable energy would allow reducing the size of the electrolyzer (Isella & Manca, 2024).

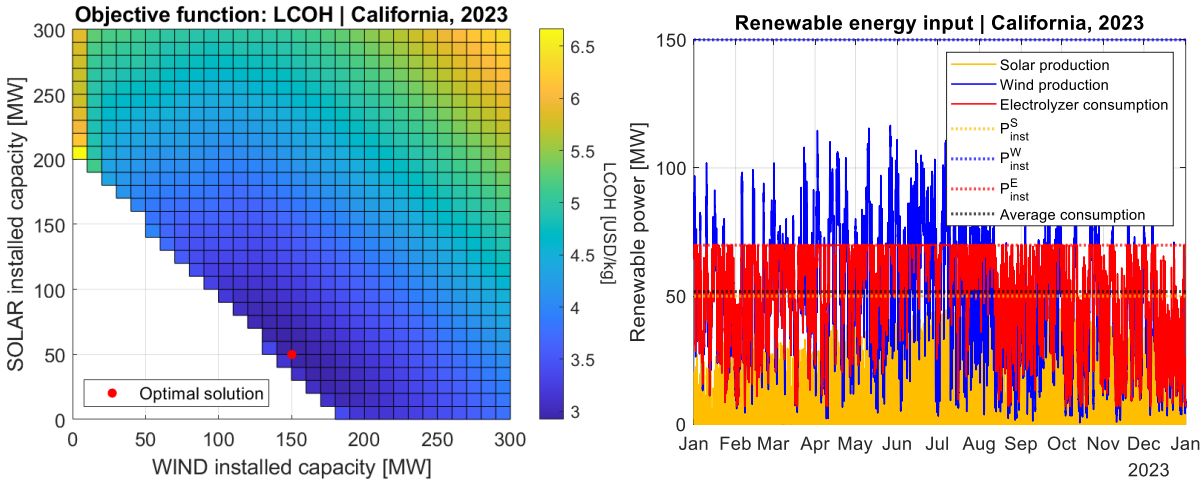

Figure 5.4: Panel A (left) shows the objective function (*i.e.* LCOH). The white area represents the unfeasibility region (*i.e.* all configurations whose renewable power installed capacities are not sufficiently high enough to meet the target hydrogen productivity). Panel B (right) shows the renewable energy production and consumption profiles corresponding to the optimal configuration.

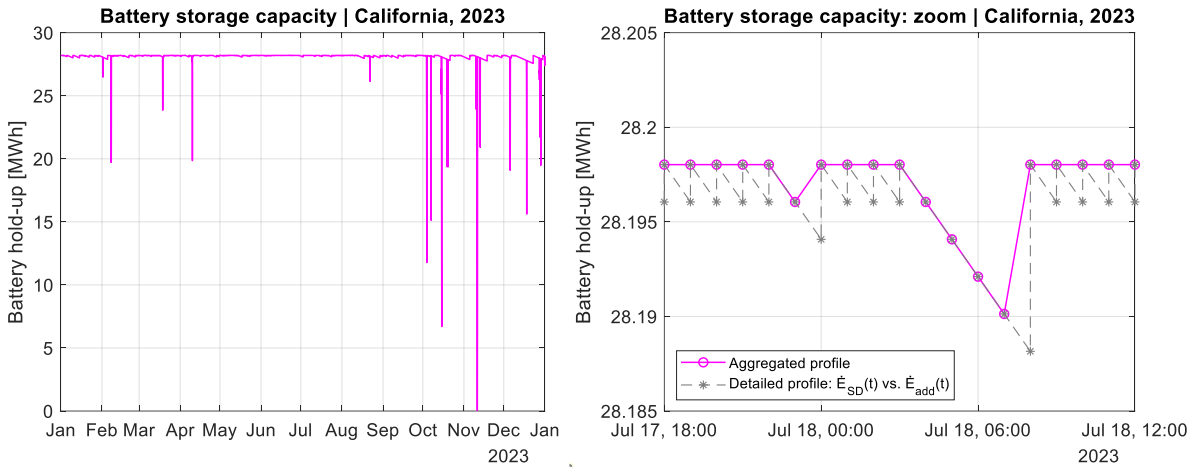

Figure 5.5: Panel A (left) shows the electrical energy hold-up profile within the battery (total installed capacity of 28.20 MWh) in 2023. Panel B (right), *i.e.* a zoom of Panel A, shows the effect of the self-discharge phenomenon: whenever possible, additional electric power (before any excess in renewable energy is curtailed) allows for restoring the self-discharge losses. Both panels refer to the optimal configuration reported in **Figure 5.4**.

Figure 5.5 addresses the optimal configuration's battery hold-up profile: Panel A provides a general overview of the battery's electrical energy hold-up throughout the whole year of assessment; Panel B shows a zoom to visualize better how the self-

discharge phenomenon was accounted for and (whenever possible) counteracted by the additional supply of electric power.

As we investigated a Californian plant, the demand for power supply from the battery visibly arises during the boreal autumn and winter, *i.e.* when renewable energy generation is particularly scarce. Conversely, in summer, its contribution is practically null, as the harvested solar and wind power already meet the input power requirements by the electrolyzer and are also capable of promptly counteracting every self-discharge loss. Therefore, another feature of this methodology is also providing an overview of renewable power generation throughout the assessed timespan by highlighting its abundance or scarcity periods.

Lastly, **Figure 5.6** reports the cumulative inlet and outlet electric power streams passing through the storage node (Panel A) and the battery (Panel B), as computing and visualizing them allows performing some consistency checks (such as verifying the principle of energy conservation). Hence, based on the case study results, the proposed methodology is a consistent and easy-to-implement tool for minimizing the required BESS capacity in dynamically operated industrial plants.

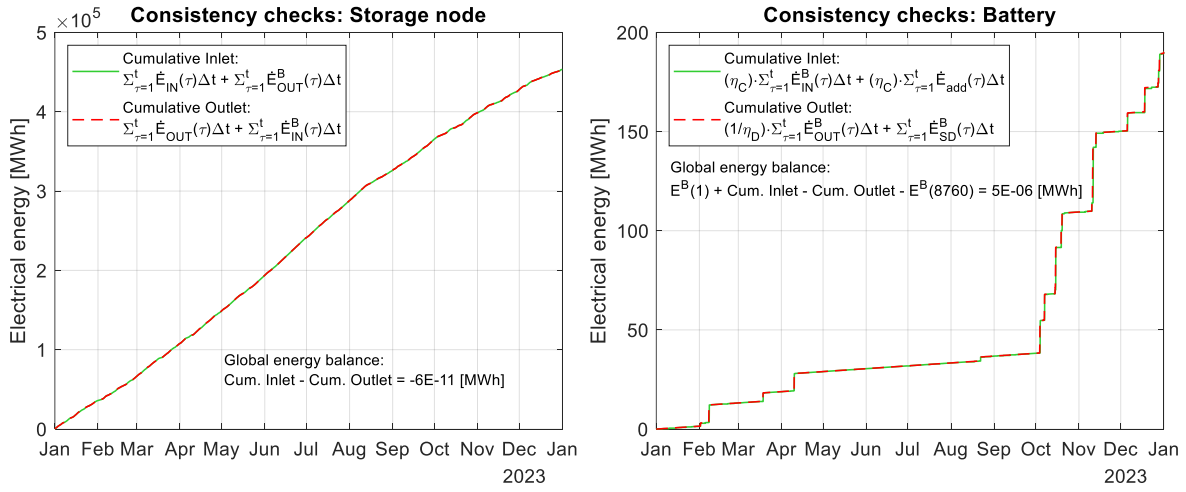

Figure 5.6: Panel A (left) shows the cumulative sum of the inlet and outlet profiles passing through the storage node, and Panel B (right) shows the cumulative sum of the inlet and outlet profiles passing through the battery. Both panels allow consistency checks (*e.g.*, computing the corresponding energy storage balances) to verify that all the energy fed to the storage node and the battery is subsequently conveyed to the electrolyzer.

To further verify the results' consistency, the same optimization routine was carried out regarding the solar and wind profiles recorded in the five years preceding 2023 (*i.e.* from 2018 to 2022). This allowed us to run a sensitivity analysis investigating the impact of different weather conditions on the optimal plant design. Accordingly, **Table 5.2** reports the optimal results for each year assessed.

Table 5.2: Optimization results from 2018 to 2023.

	Value	Unit	BESS hold-up profile
2018			
Solar capacity factor	27.37	%	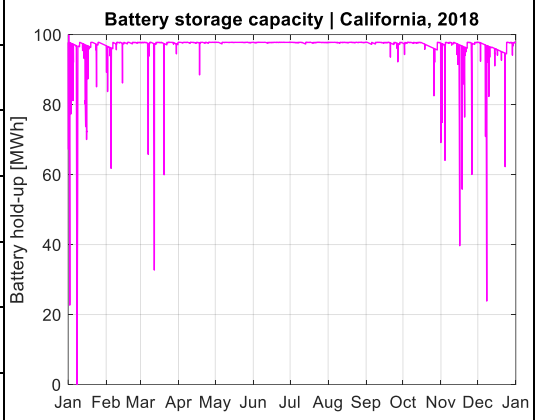
Wind capacity factor	29.62	%	
Solar installed capacity	60	MW	
Wind installed capacity	140	MW	
Electrolyzer size	73.92	MW	
BESS size	99.89	MWh	
LCOH	3.28	USD/kg	
2019			
Solar capacity factor	26.76	%	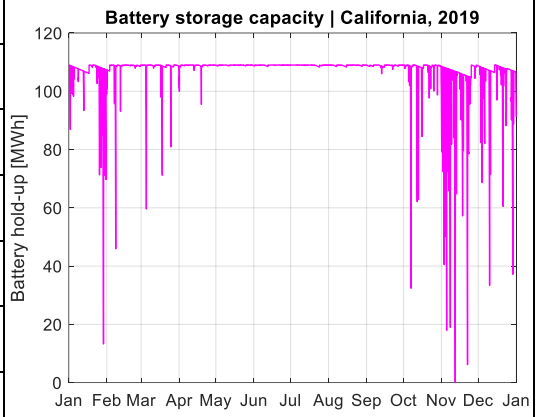
Wind capacity factor	27.06	%	
Solar installed capacity	70	MW	
Wind installed capacity	140	MW	
Electrolyzer size	80.96	MW	
BESS size	109.00	MWh	
LCOH	3.50	USD/kg	
2020			
Solar capacity factor	26.16	%	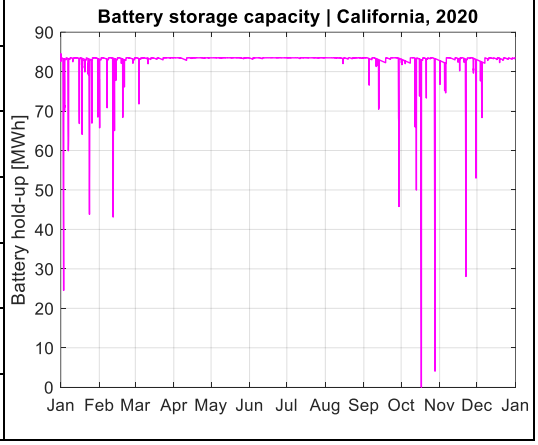
Wind capacity factor	26.82	%	
Solar installed capacity	70	MW	
Wind installed capacity	150	MW	
Electrolyzer size	73.43	MW	
BESS size	84.54	MWh	
LCOH	3.41	USD/kg	

2021		
Solar capacity factor	26.97	%
Wind capacity factor	30.28	%
Solar installed capacity	60	MW
Wind installed capacity	140	MW
Electrolyzer size	70.36	MW
BESS size	53.20	MWh
LCOH	3.03	USD/kg
2022		
Solar capacity factor	27.41	%
Wind capacity factor	26.64	%
Solar installed capacity	60	MW
Wind installed capacity	150	MW
Electrolyzer size	75.79	MW
BESS size	58.80	MWh
LCOH	3.22	USD/kg
2023		
Solar capacity factor	26.64	%
Wind capacity factor	29.61	%
Solar installed capacity	50	MW
Wind installed capacity	150	MW
Electrolyzer size	69.88	MW
BESS size	28.20	MWh
LCOH	2.92	USD/kg

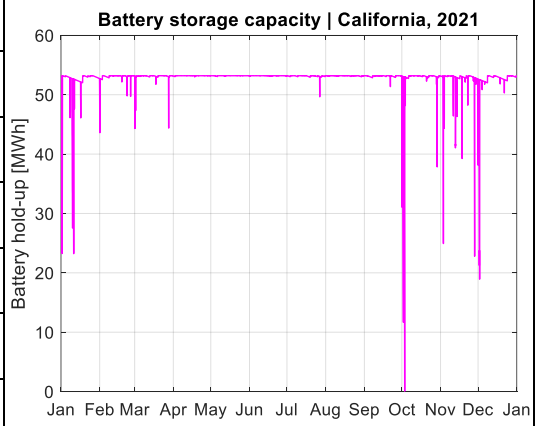

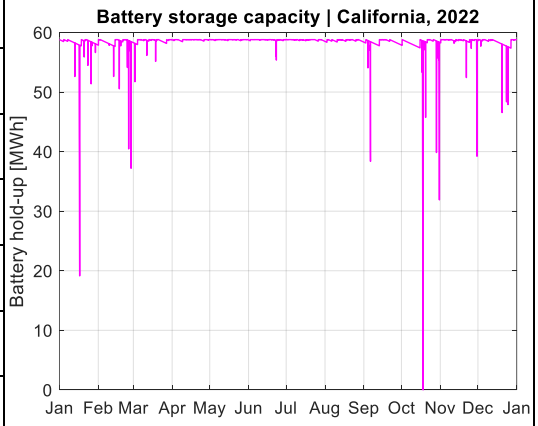

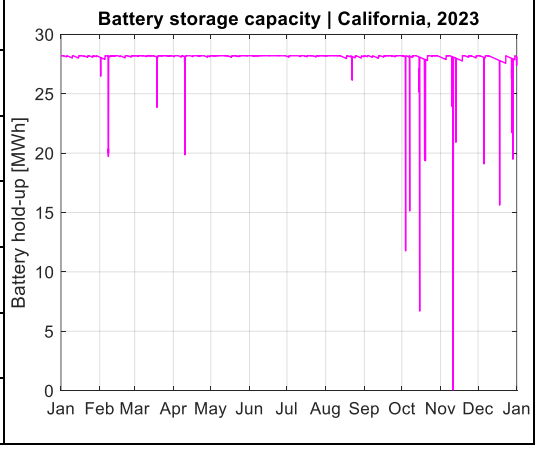

Here are some comments arising from the results reported in **Table 5.2**. First, to ensure the constant operation of the electrolyzer within its nominal ranges, the required BESS capacity sensibly changes from year to year. Such variations are primarily attributable to extended intervals of insufficient renewable power generation. In such instances, the battery becomes the sole source of electric power supply to the downstream

process, necessitating a larger storage capacity to ensure uninterrupted operation. Second, although the optimal BESS size changes from a minimum of 28.20 MWh in 2023 to a maximum of 109 MWh in 2019, all the estimated storage capacities are physically implementable as Mucci *et al.* (2023a) recommend 5 MWh and 400 MWh as reasonably valid lower and upper bounds for the BESS capacity in Power-to-X processes. Third, the required BESS capacity is determined by the distinctively scarce renewable generation arising between the second half of October and the first half of November, with the only exception being the 2018 case (as the critical need for electricity supply from the battery occurred on January 8th, 2018). Hence, the almost one-month period of the year (second half of October and first half of November) might be allocated to shut down and maintain the plant, as it would allow escaping from deplorable weather conditions and relying on smaller BESS capacities (*e.g.*, in 2022, disregarding the maximum peak achieved on October 18th, the second-highest demand for battery supply occurs on January 17th and is about 20 MWh less, allowing for a BESS capacity of 40 MWh only, instead of 58.80 MWh). It is also worth observing that the whole design and optimization of the BESS capacity were carried out under the strong assumption/hypothesis of islanded operations (*i.e.* no reliance on the electric grid to cover the unavailability of sufficient renewable sources in some specific periods of the year). Relaxing such a rigid assumption would significantly reduce the resulting BESS capacity, with a noteworthy impact on the corresponding LCOH.

5.4. Conclusions

This chapter introduced, derived, and validated a methodology for evaluating the optimal electric power delivery policy, with a (time)step-by-(time)step approach, of battery energy storage systems by minimizing their storage capacity. Specifically, the presented method requires input data from the electric power feed headed to the electricity storage node and a few battery specifications (*e.g.*, its charging and discharging efficiencies). Also, it meets full compliance with multiple supply conditions usually mandatory for downstream uses, such as ramping rates and load flexibility constraints. A case study concerning the production of green hydrogen from solar and wind power successfully tested the framework's performance. Moreover, such an assessment was referred to six different solar and wind energy profiles (*i.e.* every year from 2018 to 2023) to perform a sensitivity analysis to further stress the results' consistency and verify their robustness. Hopefully, the proposed methodology may assist researchers and stakeholders in designing and techno-economically assessing industrial applications featuring battery energy storage systems. One class above all is Power-to-X processes, whose flexible operation is crucial for their economic competitiveness against conventional (but often carbon-intensive) alternatives.

6 Green ammonia synthesis

Introductory comment

The doctoral program ended with the design and simulation of a fully green ammonia plant, *i.e.* whose hydrogen demands are fully met by renewable-powered electrolysis. What sets this assessment apart from other studies previously published by scientific literature is the innovative sizing criteria for the renewable power plant, electrolyzer, and hydrogen/electric storage systems (as discussed in the previous chapters) and the approach to maximize the whole plant's sustainability in its three-fold connotation: economic, environmental, and social (*i.e.* by a multi-objective optimization strategy). This led to interesting insights into the mutual conflict characterizing the "three pillars of sustainability", especially when addressing the design of green chemical plants.

The present chapter stems from:

Integrating economic, environmental, and social sustainability in Power-to-Ammonia plants: A multi-objective optimization methodology

Isella, A., & Manca, D.

Computers & Chemical Engineering, 2025, 198, 109082

DOI: https://doi.org/10.1016/j.compchemeng.2025.109082

Abstract

Consistent with actual decarbonization efforts in the ammonia industry, this chapter addresses the process design of Power-to-Ammonia plants (*i.e.* industrial facilities producing "green" ammonia starting from renewable energy via water electrolysis) by introducing a methodology based on the multi-objective optimization of the "three pillars of sustainability", *i.e.* economic, environmental, and social. Specifically, the proposed criterion evaluates the sizes and operating schedules of key process sections characterizing Power-to-Ammonia facilities (*e.g.*, the renewable power plant, the electrolyzer, electricity and hydrogen storage systems, *etc.*) to harmonize the three pillars (which are most often conflicting) as much as possible and identify the process configuration achieving the maximum attainable global sustainability. Valuable insights into the conceptual design of chemical processes integrating renewable energy and the associated sustainability assessment criteria are provided, and further industrial application opportunities are discussed.

6.1. Introduction

Due to the primary contribution of the ammonia industry to global greenhouse gas emissions (Isella & Manca, 2022), decarbonizing ammonia production by replacing its conventional fossil hydrogen feedstock with hydrogen from renewable-powered water electrolysis (*i.e.* a synthetic pathway typically referred as "green" ammonia (MPP, 2022)) is a topic that the scientific community has addressed with great interest in the last few years: *e.g.*, Sánchez and Martín (2018) developed and simulated equation-oriented models of the main sections of a green ammonia plant (*i.e.* renewable power generation, air separation, water electrolysis, and synthesis loop); Nayak-Luke *et al.* (2018) investigated the case of islanded (*i.e.* with neither grid connection nor alternative dispatchable power sources) green ammonia production sites; and Armijo and Philibert (2020) substantially improved previous green ammonia plant models by including an optimization methodology to compute costs of flexible production of hydrogen and ammonia from variable wind and solar energy. However, the integration of water electrolysis within chemical plants extends far beyond the ammonia industry, involving indeed many other Power-to-X processes (*i.e.* synthetic pathways in which the final product "X" derives from renewable "power"). For example, Chen and Yang (2021) and Mucci *et al.* (2023a) focused on Power-to-Methanol plants, providing valuable insights into the critical role of flexibility and buffer storage in renewable-powered processes. Concerning the multi-objective optimization (MOO) of the "three pillars of sustainability" (*i.e.* economic, environmental, and social), the proposed methodology benefits from the operating framework introduced by Scotti *et al.* (2017) and Scotti *et al.* (2018), which are pioneering works on this topic proposing a solution strategy for the MOO of sustainability in the conceptual design of conventional chemical plants (in the specific case, cumene production). On the other

hand, in the field of ammonia industry, Shin *et al.* (2023) wrote a prime reference for this chapter as they addressed the energy, economic, and environmental (*i.e.* "3E") impact of "gray" and "blue" ammonia plants (both depending on natural gas feedstocks, though "blue" technologies also feature carbon capture and storage). The present chapter aims to fill the current gap in scientific literature by extending previous publications (though applying completely different numerical techniques and replacing the energy impact analysis with the social sustainability assessment) to green ammonia synthesis, with all the increased process complexity that follows (*i.e.* unsteady-state operating conditions, new process sections such as renewable power generation and water electrolysis, need for flexible material and energy buffer storage systems, *etc.*).

This chapter is structured as follows: Section 6.2 defines the investigated system and reports the corresponding modeling tools and techno-economic assumptions; Section 6.3 states the optimization problem (*i.e.* the objective function(s), the degrees of freedom, and the constraints) and describes the adopted algorithms; Section 6.4 shows and discusses the results arising from the solution of the optimization problem; and, lastly, Section 6.5 summarizes the main findings and conclusions.

6.2. Methods

6.2.1. System description and modeling

This assessment considers a 100 MTD (*i.e.* metric tons per day) Power-to-Ammonia plant consisting of the following subsections and equipment:

- A dedicated solar and wind power plant generating renewable electricity to power the electrolysis process (however, any exceeding amount is used either to meet the electric demand of the other plant sections (see the last point of the list) or is curtailed if useless).
- A battery energy storage system (BESS) amidst the renewable park and the electrolyzer (allowing the latter always to receive electricity inputs compliant with its operating range).
- An alkaline water electrolyzer (AWE) producing green hydrogen from renewable electricity.
- A hydrogen compression (HC) and storage (HS) system amidst the electrolyzer and the Haber-Bosch process (allowing the latter always to receive a hydrogen input compliant with its operating range).
- An air separation unit (ASU) for nitrogen sourcing from air.

- A conventional Haber-Bosch process (HB) producing green ammonia starting from green hydrogen (fed by the electrolyzer or the hydrogen storage) and nitrogen (from the ASU).
- Grid connections for the HC, ASU, and HB subsections (to resort to whenever renewable electricity supply from the power plant is insufficient to power them).

Figure 6.1 reports these process units and their mutual interconnections, while the following paragraphs describe their modeling details.

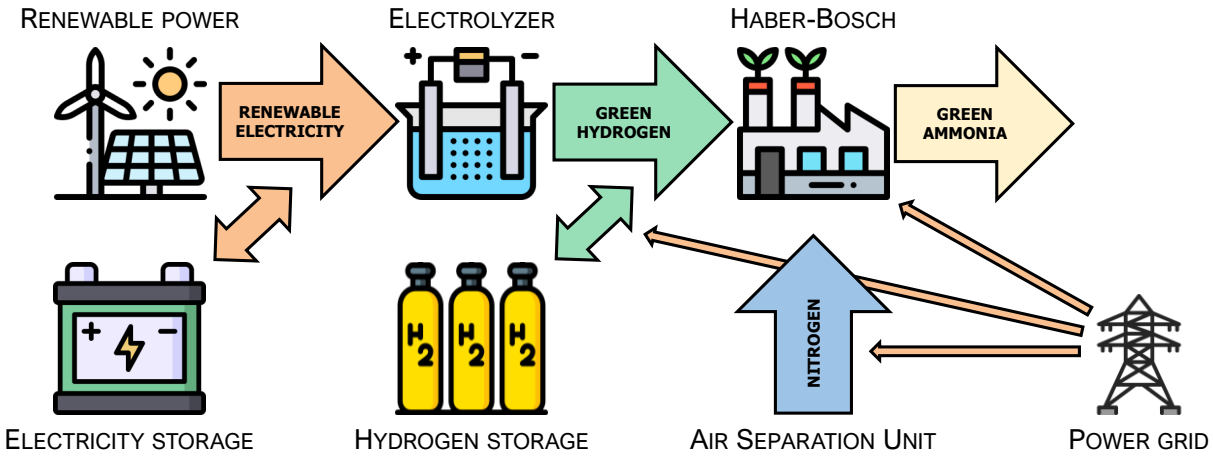

Figure 6.1: The assessed 100 MTD Power-to-Ammonia plant.

6.2.2. Solar and wind power plant

Both solar photovoltaics and wind onshore farms have been considered for the on-site harvesting of the renewable energy needed at the electrolyzer. The reference solar and wind profiles are taken from the Californian Independent System Operator (CAISO, 2024), *i.e.* one of the most extensive electrical grids worldwide featuring high renewable power integration and making its vast collection of renewable power generation data freely available on the web. **Table 6.1** reports the capacity factors of the reference renewable power profiles and the economic assumptions made to estimate the investment and operating costs of the solar and wind power plants (accordingly, values referring to the United States market were used).

6.2.3. Battery energy storage system (BESS)

A battery energy storage system (BESS) lies amidst the renewable power plant and the electrolyzer, as the latter must continuously operate within its flexibility range (see **Table 6.1**). Fundamentally, whenever the incoming renewable power is higher/lower than the maximum/minimum amount the electrolyzer can process, the battery stores/supplies such an electric energy surplus/deficit. The equations behind the battery sizing and operation (*i.e.* the BESS-related equality constraints featured by the

following optimization problem) are reported and extensively discussed in Isella and Manca (2025a), where a framework for the optimal design of such electricity storage systems is proposed. A lithium-ion type battery is considered since it is the most established large-scale battery storage technology (over 90% of the total installed capacity worldwide in 2019 (IRENA, 2019)). Also, their costs fell by 80% from 2010 to 2017 (IRENA, 2017), further pushing their adoption in the energy and industrial sectors. All the techno-economic assumptions made to model the BESS and estimate its capital and operating costs are reported in **Table 6.1**.

6.2.4. Alkaline water electrolyzer (AWE)

The electrolysis section converts the renewable energy input into hydrogen. At the present day, in terms of electrolyte types, different electrolyzer technologies are available: mainly alkaline (AWE), proton exchange membrane (PEM), and solid oxide (Arsad *et al.*, 2023). Though PEM electrolyzers have gained great interest in recent years due to their increasing technological readiness level and wider flexibility ranges, here we consider only AWEs since they show the highest maturity, the most extensive commercial outreach in the industrial sector (*e.g.*, having been employed in the chloralkali process for over a century), and the potential to be used in larger-scale green ammonia plants, while being also cheaper. Moreover, despite their higher inertia due to the greater liquid hold-up, alkaline water electrolyzers show sufficiently high flexibility to be integrated for ammonia synthesis by the Haber-Bosch process (Isella *et al.*, 2024). An AWE typically consists of two electrodes separated by a diaphragm and surrounded by an alkaline liquid electrolyte that conducts ions between them. At the cathode, water splits, producing hydrogen and releasing hydroxide anions that pass through the diaphragm and recombine at the anode to form oxygen (David *et al.*, 2019). Also, per the latest advancements, the electrolyzer is assumed to show perfectly flexible behavior, *i.e.* to follow fluctuating electricity inputs instantaneously (as long as within the minimum and maximum permitted power input range) and a constant efficiency (Armijo & Philibert, 2020). **Table 6.1** reports the technical data and operating assumptions of the AWE.

6.2.5. Hydrogen compression (HC) and storage (HS)

The investigated plant also features a compressed hydrogen storage system amidst the electrolyzer and the Haber-Bosch process (*i.e.* the conversion process), as the latter must continuously operate within its flexibility range (see **Table 6.1**). This means that when the incoming hydrogen mass flow is higher/lower than the maximum/minimum feedstock the Haber-Bosch process allows, the storage system accumulates/supplies such a hydrogen surplus/deficit. The model equations of the storage system (*i.e.* the hydrogen storage-related equality constraints of the following optimization problem) are all reported and extensively discussed in Isella and Manca (2025b), where we introduced a general criterion for the optimal design of flexible (*i.e.* dynamically

operated) hydrogen storage tanks. The selected storage system has a working pressure of 200 bar (*i.e.* much higher than in the electrolyzer), so hydrogen flows heading to the storage must first be compressed. Accordingly, multistage centrifugal compressors were considered and simulated in UniSim® Design R492 to evaluate the associated electricity consumption (see the **Appendix** for further details). **Table 6.1** reports the technical data and assumptions about hydrogen storage and compression.

6.2.6. Air separation unit (ASU)

While most conventional ammonia plants feed ambient air directly to the process (precisely, in the secondary reformer) to simultaneously meet the demands of nitrogen for ammonia synthesis and oxygen for partial oxidation of the fossil feedstock, green ammonia plants call for pure nitrogen and (green) hydrogen input flows. As the latter comes from the electrolyzer and the hydrogen storage sections, air fractionation is the most common way to supply pure nitrogen to the ammonia reactor. Hence, we developed a conventional double-column cryogenic ASU model in UniSim® Design R492 to estimate the nitrogen flows and the associated operating costs (see **Table 6.1**, **Figure 6.2**, and the **Appendix** for further details).

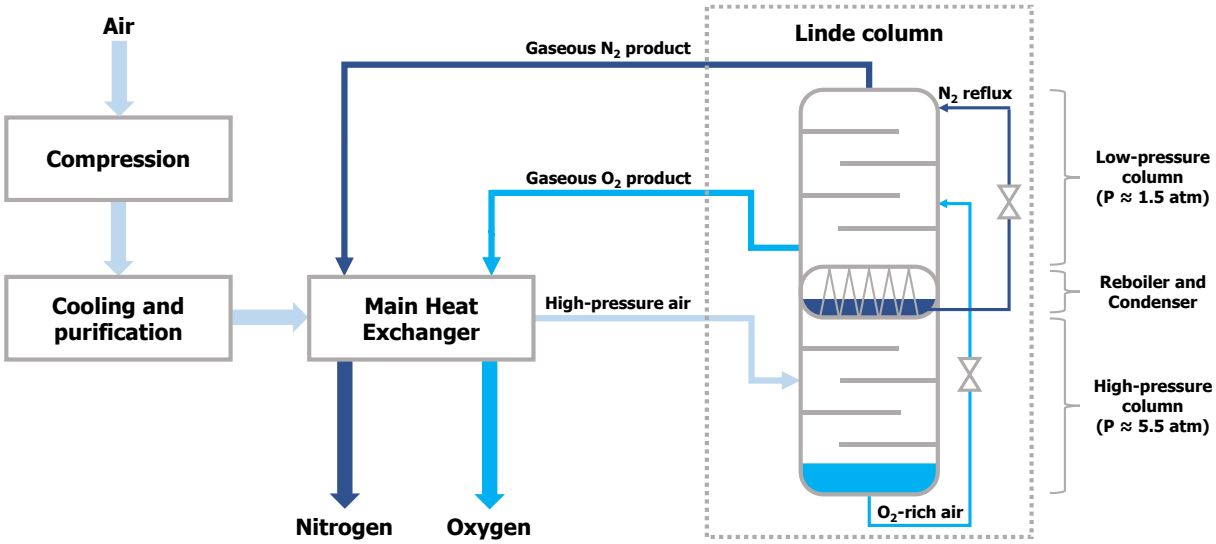

Figure 6.2: Block flow diagram of the ASU section.

Such a layout benefits from the pressure difference between the two columns, as it is such that the condensing reflux of the high-pressure column can provide heat to the low-pressure column reboiler; thus, there is no need for any cooling or heating external utilities (Soave *et al.*, 2006). However, despite the self-sufficient thermal integration of the two columns (proving stable as long as ramping rates are not faster than 10%/min (Cheng *et al.*, 2022): like in the present case, as discussed in Section 6.3 about the use of UniSim® models within the optimization routine), this process still features a high electricity consumption for compressing the air and nitrogen flows (Böcker *et al.*, 2013).

6.2.7. Haber-Bosch process (HB)

The model for the ammonia synthesis section mainly derives from Sánchez and Martín (2018) and was translated into UniSim® Design R492 (see **Figure 6.3**, **Table 6.1**, and the **Appendix** for further details). Specifically, it features a three-stage compression system, a direct-cooling three-bed reactor, and a separation section consisting of two flash drums. The synthesis loop operates at 200 bar since, as is typical for these scales (*i.e.* 100 MTD), no refrigeration cycles are implemented to condense the ammonia product, hence the need for quite high operating pressures. Specifically focusing on the reaction section, we assumed that the ammonia synthesis kinetics are described by the Temkin-Pyzhev equation (Morud & Skogestad, 1998).

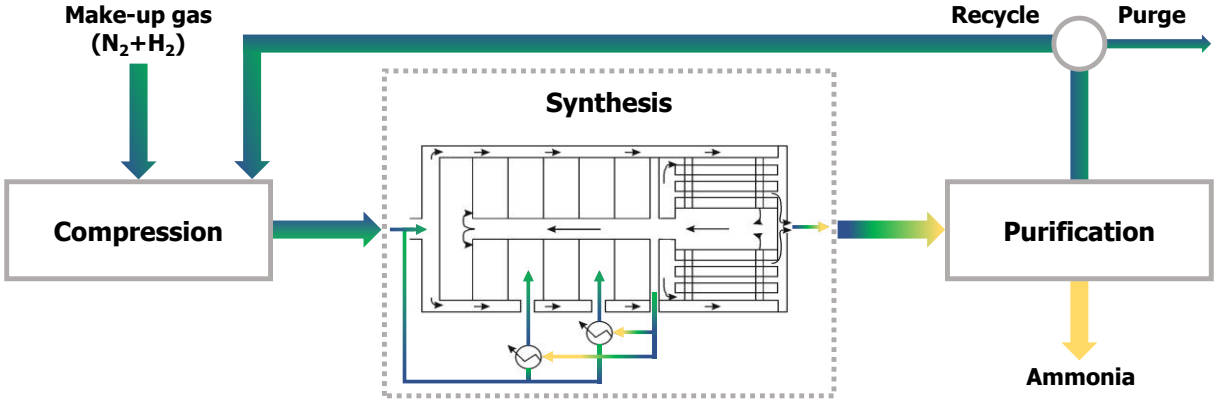

Figure 6.3: Block flow diagram of the HB section.

Note that the flexibility range of the Haber-Bosch section (*i.e.* the minimum and maximum allowed hydrogen input mass flow deviation from nominal conditions) is a critical parameter for the design of the hydrogen storage system and, hence, for the resulting global sustainability of the process.

Table 6.1: Input assumptions and technical data.

Item	Value	Unit	References/Notes
DATASET			
Location	California		
Year	2023		
Solar capacity factor	26.64%	[-]	CAISO (2024)
Wind capacity factor	29.66%	[-]	CAISO (2024)
Time discretization	1	[h]	
TECHNICAL DATA			
Discount rate	5%	[-]	Mucci *et al.* (2023a)

Solar Photovoltaics			
Lifetime	25	[y]	Armijo and Philibert (2020)
CapEx	1119	[USD/kWe]	IRENA (2023)
OpEx	1.70%	[CapEx/y]	Armijo and Philibert (2020)
GWP	136.24	[kg_{CO2eq}/MWh]	Rossi *et al.* (2023)
Wind Onshore			
Lifetime	25	[y]	Armijo and Philibert (2020)
CapEx	1285	[USD/kWe]	IRENA (2023)
OpEx	2%	[CapEx/y]	Armijo and Philibert (2020)
GWP	26.33	[kg_{CO2eq}/MWh]	Rossi *et al.* (2023)
Electricity storage			
Lifetime	10	[y]	Marocco *et al.* (2024)
CapEx	310	[USD/kWe]	Mucci *et al.* (2023a)
OpEx	2%	[CapEx/y]	Marocco *et al.* (2024)
Charging efficiency	0.95	[-]	Marocco *et al.* (2024)
Discharging efficiency	0.95	[-]	Marocco *et al.* (2024)
Self-discharge rate	0.007%	[load/h]	Marocco *et al.* (2024)
GWP	50	[kg_{CO2eq}/kWh]	Gutsch and Leker (2022)
Electrolyzer			
Lifetime	10	[y]	Fraunhofer ISE (2021)
CapEx	700	[USD/kWe]	Fraunhofer ISE (2021)
OpEx	2%	[CapEx/y]	Armijo and Philibert (2020)
Stack DC consumption	4.65	[kWh/Nm^3_{H2}]	McPhy (2023)
Maximum load flexibility	1	[nominal load]	McPhy (2023)
Minimum load flexibility	0.1	[nominal load]	McPhy (2023)
GWP	0.215	[kg_{CO2eq}/kg_{H2}]	Krishnan *et al.* (2024)

Hydrogen compression and storage			
Lifetime	20	[y]	DEA (2020)
CapEx[1]	1900	[USD/kg_{H2}]	DEA (2020)
OpEx[2]	1%	[CapEx/y]	Armijo and Philibert (2020)
P inlet (Electrolyzer)	30	[bar]	McPhy (2023)
P outlet (H_2 storage)	200	[bar]	DEA (2020)
Electricity consumption	1.03	[MWh/t_{H2}]	HC model
GWP	200	[kg_{CO2eq}/kg_{H2}]	Knop (2022)
Air Separation Unit			
Electricity consumption	0.08	[MWh/t_{N2}]	ASU model; Böcker *et al.* (2013)
Haber-Bosch			
NH_3 target productivity	4.17	[t_{NH3}/h]	*i.e.* 100 MTD
H_2 target feed	0.78	[t_{H2}/h]	HB model
Maximum ramp	100%	[load/h]	Genova and Panza (2022)
Maximum load flexibility	110%	[nominal load]	Genova and Panza (2022)
Minimum load flexibility	10%	[nominal load]	Genova and Panza (2022)
Electricity consumption	0.59	[MWh/t_{NH3}]	HB model
Electric grid			
Electricity cost	100	[USD/MWh]	Genova and Panza (2022)
GWP	370	[kg_{CO2eq}/MWh]	Our World in Data (2024)

[1] Capital costs for Type I tanks and the compression system; [2] Excluding compression power (*i.e.* electricity supplied by the renewable power plant or the grid).

6.3. The optimization problem

Once each section of the Power-to-Ammonia plant is modeled, the whole system undergoes an optimization procedure searching for the best design of the green hydrogen production line (*i.e.* the Power-to-Hydrogen segment): namely, the solar and wind farms' installed capacities, the electrolyzer size, and both the electricity and hydrogen storage capacities. Instead, the characteristic sizes of the ASU and HB

sections are already given according to the well-established state-of-the-art in small-capacity gray ammonia plants.

$$
\begin{cases}
\underset{P^{S}_{\text{inst}},P^{W}_{\text{inst}}}{\textbf{Min}}\left[\Phi^{\text{X}}_{\text{OBJ}}\right] \quad \text{with X = ECO, ENV, SOC, or MOO} \\
\text{s.t.:} \\
\dot{E}_{IN}(t) = \min(\dot{E}^{S}(t) + \dot{E}^{W}(t), P^{E}_{\text{inst}}) & \text{(a)} \\
\dot{E}_{OUT}(t) = \begin{cases} \dot{E}_{IN}(t) + \left[\eta_D \cdot \sum_{\tau=1}^{t-1}\left(\frac{d}{dt}E^{B}(\tau)\right)\right] & \text{if } \sum_{\tau=1}^{t-1}\left(\frac{d}{dt}E^{B}(\tau)\right) \geq 0 \quad \text{(i)} \\ \dot{E}_{IN}(t) + \left[\frac{1}{\eta_C} \cdot \sum_{\tau=1}^{t-1}\left(\frac{d}{dt}E^{B}(\tau)\right)\right] & \text{if } \sum_{\tau=1}^{t-1}\left(\frac{d}{dt}E^{B}(\tau)\right) < 0 \quad \text{(ii)} \end{cases} & \text{(b)} \\
\sum_{\tau=1}^{8760}\dot{E}_{OUT}(\tau) = 8760 \cdot \dot{E}^{E}_{\text{target}} & \text{(c)} \\
\dot{m}^{H_2}_{IN}(t) = \dot{E}_{OUT}(t) \cdot \frac{\rho_{H_2}}{\xi_E} & \text{(d)} \\
\dot{m}^{H_2}_{OUT}(t) = \dot{m}^{H_2}_{IN}(t) + \sum_{\tau=1}^{t-1}\left[\dot{m}^{H_2}_{IN}(\tau) - \dot{m}^{H_2}_{OUT}(\tau)\right] & \text{(e)} \\
\text{HC process simulation (Mass and Energy balances)} & \text{(f)} \\
\text{ASU process simulation (Mass and Energy balances)} & \text{(g)} \\
\text{HB process simulation (Mass and Energy balances)} & \text{(h)}
\end{cases}
\tag{6.1}
$$

Eq. (6.1) provides the formulation of the general optimization problem. According to the objective function assigned, it has been applied to three SOO (*i.e.* addressing only one pillar of sustainability at a time) and one MOO (*i.e.* addressing the three pillars of sustainability together) problems. The proposed optimization problem primarily derives from Isella and Manca (2024), Isella and Manca (2025a), and Isella and Manca (2025b). Analogously, the objective function is investigated by assessing different combinations of solar and wind installed capacities (*i.e.*, the degrees of freedom, each ranging from 0 to 500 MW with a resolution of 10 MW) through a brute-force but exhaustive grid-search routine in MATLAB R2024a, which allows estimating the corresponding electrolyzer and storage systems sizes. In this regard, the whole procedure summarized in Eq. (6.1) is subjected to several constraints. Constraint (a), in orange, refers to the electricity input harvested by the renewable power plant (*i.e.* the combination of both solar and wind farms); (b), in magenta, refers to the optimal electricity output from the electricity storage node heading to the electrolyzer (as discussed in Isella and Manca (2025a)); (c), in gray, is the productivity constraint, balancing the electricity input to the electrolyzer to the corresponding amount needed to meet the green hydrogen demand over the assessed timespan (in the present case, 8760 hours: *i.e.* one year, assuming no maintenance breaks or emergency shutdowns occur); (d), in red, refers to the electrolysis process (*i.e.* the conversion of electricity into hydrogen); (e), in green, refers to the optimal hydrogen output from the hydrogen

storage node heading to the ammonia synthesis (as discussed in Isella and Manca (2025b)); finally, (f), (g), and (h) refer to the mass and energy balances denoting the UniSim® models of the ASU, HC, and HB sections, respectively.

In this regard, it is worth mentioning that all these models run under stationary conditions. Indeed, as all these processes exhibit much shorter transients (*i.e.* 15 minutes at most) than the sampling time of the renewable energy input (*i.e.* solar and wind profiles with 1-hour resolution), the operating regimes of these sections were reasonably approximated as a piecewise constant series of different steady-state configurations. As said before, the optimization problem reported in Eq. (6.1) was first applied to each pillar of sustainability, individually. Consequently, the following paragraphs will define the corresponding objective functions (*i.e.* Φ_{OBJ}^{ECO}, Φ_{OBJ}^{ENV}, and Φ_{OBJ}^{SOC}). Finally, as the same formulation was also used to solve the MOO sustainability problem, the last paragraph of the present section defines the corresponding objective function (*i.e.* Φ_{OBJ}^{MOO}).

6.3.1. Economic sustainability

An industrial process is economically sustainable when it can incur expenses and earn profit; in other words, it generates new material wealth (Douglas, 1988). The most obvious economic sustainability metric is the manufacturing cost of the final product, as it can be easily compared to the corresponding market price for the estimation of potential profits. Concerning carbon-mitigating synthetic pathways, the success of such alternative production routes lies in production costs comparable, if not lower than (hopefully), to those of conventional technologies. Regarding the ammonia industry, market prices have recently experienced significant fluctuations due to rising international natural gas prices, influenced by geopolitical events such as the Russia-Ukraine war. Accordingly, such an event boosted research in decoupling ammonia production from fossil fuels (Isella *et al.*, 2023). Eq. (6.2) provides the formulation of the economic sustainability objective function (*i.e.* the levelized cost of ammonia, LCOA):

$$\Phi_{OBJ}^{ECO} = LCOA = \frac{\sum_{j=S,W,B,E,H,G} \left(\frac{CapEx_j}{\sum_{n=1}^{NY_j} (1+r)^{-n}} + OpEx_j \right)}{8760 \cdot \dot{m}_{target}^{NH_3}} \tag{6.2}$$

Precisely, it consists of the sum of the annualized capital expenditure (Aromada *et al.*, 2021) and the annual operating expenditure of each unit involved in the green hydrogen production line (*i.e.*, the renewable power plant, the electrolyzer, and the electricity/hydrogen storage systems), divided by the annual ammonia productivity target. Consistent with Eq. (6.1), the most economically sustainable configuration minimizes the LCOA, which leads to the lowest production costs.

6.3.2. Environmental sustainability

Traditionally, process design mainly focused on the economics of industrial plants. More recently, thanks to amplified awareness of ecological issues (such as global warming and climate change) and increasingly stringent environmental standards, a growing interest is taking place in the scientific and industrial communities to include environmental sustainability in process design (Stefanis *et al.*, 1995; Young & Cabezas, 1999; Grossmann & Guillén-Gosálbez, 2010). In this regard, process simulation and optimization still play a crucial role. Indeed, environmental issues are no longer regarded as mere constraints within economic optimization problems but are now expressed as independent objective functions (Azapagic & Clift, 1999). Consistently, environmental sustainability here is evaluated through the objective function reported in Eq. (6.3):

$$\Phi_{\mathrm{OBJ}}^{\mathrm{ENV}} = GWP_{\mathrm{tot}} = \frac{\sum_{j=S,W,B,E,H,G} \left(GWP_j^y \right)}{8760 \cdot \dot{m}_{\mathrm{target}}^{NH_3}} \tag{6.3}$$

Specifically, GWP (Global Warming Potential) accounts for the carbon intensity of all the process sections featured by the Power-to-Ammonia plant (see **Table 6.1** for the individual GWPs). Such emission factors may be retrieved from technical literature or accredited databases (*e.g.*, DOE (2025)) and typically depend on the plant's location and operating conditions. Indeed, GWP (*i.e.* the most popular metric to assess climate change in life cycle assessments, LCAs) is the most worrying LCA impact result for industries, engineering companies, and policymakers. To cite one example, tax credits for green hydrogen under the US Inflation Reduction Act of 2022 (Congress.gov, 2022) were granted solely according to specific thresholds of CO_2 equivalent emitted for a kilogram of hydrogen (ignoring other conventional LCA impact categories such as acidification, eutrophication, or human toxicity). Accordingly, Shin *et al.* (2023) suggest quantifying the environmental impact of ammonia synthesis by assessing the GWP only. Hence, referring to the GWP (or, in other words, the carbon intensity) of the ammonia product and the specific process sections of the ammonia plant is deemed discriminative for those dealing with the feasibility studies of such facilities. Specifically, each GWP is an intensive quantity since it refers to a given functional unit (*e.g.*, concerning the electrolyzer, per unit mass of hydrogen produced). In Eq. (6.3), first, GWPs must be expressed extensively and annualized: in the case of electricity and hydrogen storage (being one-time emissions), the GWP must be multiplied by the installed capacity and then divided by the lifetime; in all the other cases (being lifetime-long emissions), the GWP must be multiplied by the yearly amount of the functional unit (*i.e.* the total energy or mass processed throughout the assessed timespan). Therefore, these annualized extensive GWPs are made intensive again by dividing them by the annual ammonia productivity target. Consistent with Eq. (6.1), the most environmentally sustainable configuration minimizes the total GWP, which leads to the lowest carbon intensity. As previously said, the GWP metric was adopted to allow

easy comparisons with typical environmental regulatory limits; however, it expands the assessment to a "cradle-to-grave" perspective. Indeed, as GWPs are typically computed by LCA studies, they tend to account for all those emissions extending from the construction to the decommissioning phase. Nevertheless, industrial stakeholders are primarily concerned about "gate-to-gate" emissions, *i.e.* from the entrance "gate" to the exit "gate" of the production site, as they provide a more concrete measurement of the plant's accountability in polluting. The Power-to-Ammonia plant assessed in this chapter is fully green, except for the auxiliary electricity supply from the power grid: this means that no Scope 1 (*i.e.* direct) emissions are generated (EPA, 2024); if anything, Scope 2 (*i.e.* indirect) only when relying on the external electrical network (*i.e.* according to its energy mix). Therefore, the gate-to-gate emissions by the plant can be visualized by focusing only on the grid-related component of the total GWP.

6.3.3. Social sustainability

Social sustainability is perhaps the least defined and least understood dimension of sustainability. Indeed, a univocal definition of social sustainability is still lacking in dedicated literature. It embraces different topics such as social responsibility, equity, security, and quality of life. The social impact of a chemical plant may be broken down into several components and issues. One might identify the social contribution of a chemical plant or process in terms of safety, security, employment, ethical and political issues, citizen involvement, *etc*. Putting the safety aspect momentarily aside, we can assume that green or gray chemical plants do not make particular differences regarding security, ethical and political issues, and citizen involvement. Indeed, engineers handle both gray and green processes with a shared moral background. Moreover, as far as employment is concerned, modern chemical plants do not involve significant numbers of operators, which leads to a non-problem, even assuming little changes in the number of workers. Nonetheless, such variations (if any) would likely be negligible and certainly would not substantially affect the job politics of any specific country, region, or community. Back to the safety aspects concerning the social pillar of sustainability, by focusing on the battery limits of the plant (*i.e.* gate-to-gate approach), we have the operators (both field and control-room ones) whose safety must be preserved. In addition, any critical industrial accident might also have repercussions on people and the environment outside of the plant's gates. That is why our social assessment focuses on reducing the impact of accidents on humans. Accordingly, at the industrial level, health and safety play a paramount role and are, in most cases, delineated and compelled by law constraints. In a few words, industrial activities cannot be socially sustainable without being safe for the workers and the surrounding population. This way, assessing social sustainability also allows for identifying the "hot spots" of the system, *i.e.* those operations contributing most to the social impact and to be targeted for maximum improvement (Azapagic & Perdan, 2005). Consequently, we opted for a social sustainability metric based on the Fire and Explosion Index (FEI), developed by the Dow Chemical Company (American Institute

of Chemical Engineers, 2016), due to its wide popularity in the chemical industry since it was first released in the 1960s. Specifically, we referred to International Labour Organisation (1993), as it extensively discusses how to estimate such an index from a simplified version of the Dow method, with the advantage of using units of measurement that adhere to the metric system. Since such a methodology addresses only chemical processes handling and storing hazardous materials, the FEI assessment focused on the electrolyzer and hydrogen storage sections. This choice is consistent with the higher dangerousness associated with such units as against the renewable power plant and the battery; however, it also derives from the lack of inherent safety assessment methodologies allowing the evaluation of many process units associated with the generation and storage of electricity, even though ever more present in the chemical industry. Nevertheless, since the capacities of both electricity and hydrogen storage systems are directly correlated, even BESS-related hazards are implicitly undertaken by this methodology (however, this aspect will be debated in more detail in Section 6.4). Accordingly, Eq. (6.4) reports the objective function addressing social sustainability:

$$\Phi_{\mathrm{OBJ}}^{\mathrm{SOC}} = FEI_{\mathrm{tot}} = \sum_{j=E,H} \left(FEI_j \right) \tag{6.4}$$

Practically, the FEI of the electrolyzer and the hydrogen storage system is estimated for every investigated configuration (*i.e.* for each combination of solar and wind installed capacities) by referring to the highest values of material hold-up attained within the respective process units (hence uniquely depending on the corresponding installed sizes of the electrolyzer and the hydrogen storage system). **Table 6.2** shows the classification in hazard categories according to the FEI values. Consistent with Eq. (6.1), the most socially sustainable configuration must minimize the total FEI (*i.e.* leading to the lowest hazard severity).

Table 6.2: Categories of hazard severity according to the FEI (International Labour Organisation, 1993).

Category	Fire and Explosion Index (FEI)	Hazard severity
Category I	FEI < 65	Light
Category II	65 ≤ FEI < 95	Intermediate
Category III	FEI ≥ 95	Heavy

6.3.4. Multi-objective optimization

The search for the optimal solution to a problem is a common question in every industrial sector: multi-objective optimization problems involve multiple conflicting criteria (*i.e.* objective functions) rather than just one. Therefore, while SOO problems

usually show a unique optimal solution, MOO problems are characterized by a trade-off among conflicting objective functions leading to a set of compromise solutions, also known as the Pareto front (Osyczka, 1978). Hence, solving MOO problems inherently calls for some human decision-making, which can be supported by dedicated tools and strategies, to identify the optimal solution among all those theoretically acceptable. Accordingly, the present chapter resorts to the scalarization technique, a methodology aiming at combining more objective functions into one through an appropriate scalarization function (in this case, their linear combination proved to be the most user-friendly option). In this way, by selecting suitable weights to set the relative importance among the objective functions (here lies the core of the human decision-making process demanded by this technique), MOO problems can be easily converted to SOO problems (Miettinen & Mäkelä, 2002). In return, scalarization requires normalizing each objective function to make it comparable.

In the present case, each objective function is converted to a normalized index assuming a value of 1 for the "most sustainable" solution and 0 for the "least sustainable" one. Eqs. (6.5), (6.6), and (6.7) report the normalized sustainability indexes for each pillar of sustainability:

$$EcoSI_i = \frac{\max(LCOA) - LCOA_i}{\max(LCOA) - \min(LCOA)} \tag{6.5}$$

$$EnvSI_i = \frac{\max(GWP_{\text{tot}}) - GWP_{\text{tot},i}}{\max(GWP_{\text{tot}}) - \min(GWP_{\text{tot}})} \tag{6.6}$$

$$SocSI_i = \frac{\max(FEI_{\text{tot}}) - FEI_{\text{tot},i}}{\max(FEI_{\text{tot}}) - \min(FEI_{\text{tot}})} \tag{6.7}$$

As said above, the objective function of the scalarized MOO problem is simply the linear combination of the economic, environmental, and social Sustainability Indexes: each of them shall be weighed appropriately, according to the relative importance given by the user to the three pillars of sustainability. Hence, Eq. (6.8) provides the objective function related to the scalarized MOO problem, *i.e.* the Global Sustainability Score (GSS):

$$\begin{aligned} &\Phi_{\text{OBJ}}^{\text{MOO}} = -\left(GSS\right) = -\left(w_{\text{ECO}} \cdot EcoSI + w_{\text{ENV}} \cdot EnvSI + w_{\text{SOC}} \cdot SocSI\right) \\ &\text{with } \; w_{\text{ECO}} + w_{\text{ENV}} + w_{\text{SOC}} = 1 \end{aligned} \tag{6.8}$$

Like the single Sustainability Indexes, GSS ranges from 0 (*i.e.* worst-case scenario) to 1 (*i.e.* best-case scenario). It is worth noting that the minus sign in Eq. (6.8) allows maximizing GSS in line with the minimization approach of Eq. (6.1).

6.4. Results and discussion

6.4.1. SOO results

As mentioned before, we started addressing the three SOO problems individually (*i.e.* optimizing each sustainability pillar separately). After that, we moved on to the MOO problem (*i.e.* optimizing green ammonia plants' overall sustainability) by resorting to the scalarization technique, which requires an appropriate weighting factor for each dimension of sustainability.

Table 6.3 shows the optimal results for the SOO assessment of the three pillars of sustainability (*i.e.* the three configurations minimizing the LCOA, GWP, and FEI of the investigated Power-to-Ammonia plant, respectively).

Table 6.3: Characteristic sizes and objective function values by the optimal process configurations for each pillar of sustainability (SOO approach).

OPTIMAL SOLUTION		ECO	ENV	SOC
Solar park	[MW]	40	0	20
Wind farm	[MW]	190	190	470
Electrolyzer	[MW]	44.59	51.51	41.07
Hydrogen storage	[t_{H2}]	4.88	122.93	0.00
Battery storage	[MWh]	4.83	15.85	0.00
LCOA (Φ_{OBJ}^{ECO})	[USD/t_{NH3}]	720.15	1168.66	1338.25
GWP (Φ_{OBJ}^{ENV})	[t_{CO2eq}/t_{NH3}]	0.80	0.54	1.10
FEI (Φ_{OBJ}^{SOC})	[-]	158.38	170.89	113.02

Hereafter, the next lines discuss such results more in depth, singularly addressing each dimension of sustainability by visualizing and commenting on the corresponding objective functions.

Starting from the economic sustainability, **Figure 6.4** shows the values and topology of Φ_{OBJ}^{ECO}. Predictably, the economically optimal solution calls for renewable generation installed capacities to be neither too high nor too low. Indeed, by increasing the size of the renewable power plant (both solar and wind), the LCOA rises too due to its high costs (the CapEx, especially). Conversely, smaller power plants (hence, lower power inputs) call for bigger electrolyzers (as they need to process every potential power peak made available by the renewable park) and storage systems (to mitigate the stronger discontinuities arising from such operating regimes). Thus, the minimum lies halfway between those extreme behaviors, though closer to the feasibility limit due to the lower

costs associated with the electrolyzer and the storage systems than those of the power plant.

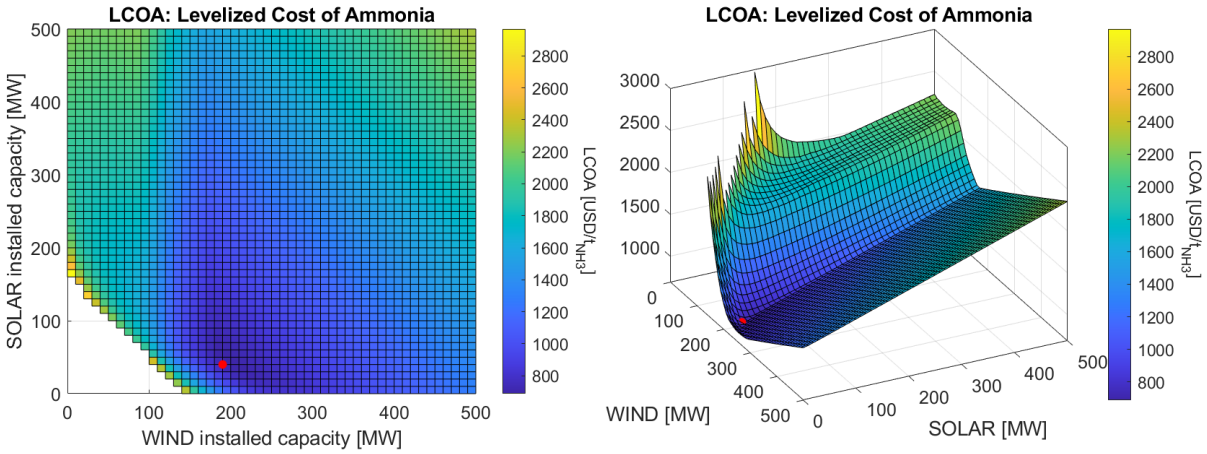

Figure 6.4: Two- (left) and three-dimensional (right) representations of the economic sustainability objective function (Φ_{OBJ}^{ECO}, *i.e.* LCOA). The red dot marks the minimum (*i.e.* the economically optimal solution). The white area in the 2D diagram represents the infeasible region (*i.e.* process configurations lacking sufficient installed power generation capacities to meet the ammonia productivity constraint).

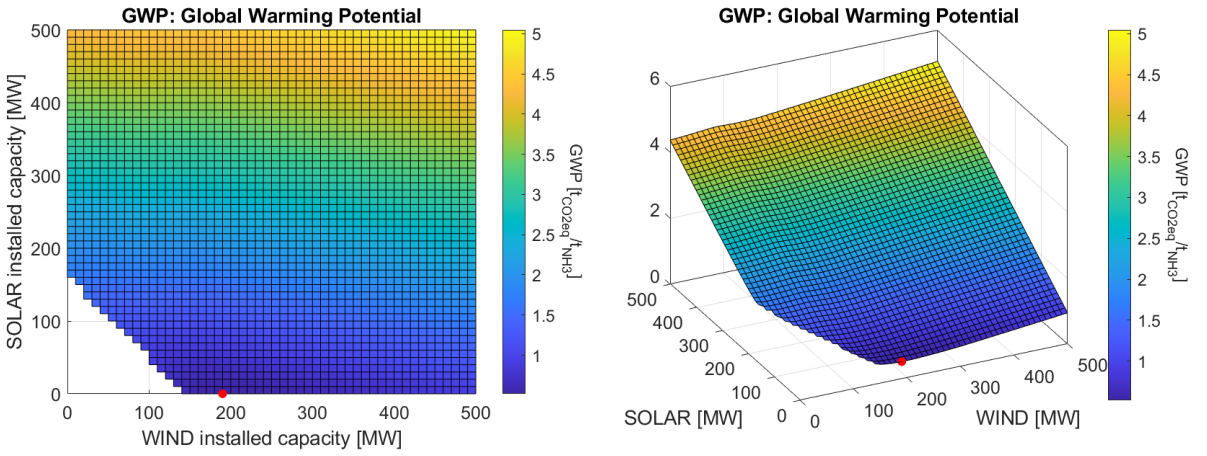

Figure 6.5: Two- (left) and three-dimensional (right) representations of the environmental sustainability objective function (Φ_{OBJ}^{ENV}, *i.e.* the total GWP). The red dot marks the minimum (*i.e.* the environmentally optimal solution). The white area in the 2D diagram represents the infeasible region (*i.e.* process configurations lacking sufficient installed power generation capacities to meet the ammonia productivity constraint).

Moving on to environmental sustainability, the corresponding objective function (*i.e.* Φ_{OBJ}^{ENV}) is illustrated in **Figure 6.5**. In this case, the optimal solution lies in the wind-power axis, *i.e.*, no reliance on solar power for renewable electricity generation. This is mainly due to the higher (cradle-to-grave) GWP shown by photovoltaic panels than wind turbines (see **Table 6.1**). Also, the optimal (wind-only) power plant capacity is

neither the minimum allowable one (*i.e.* bordering the feasibility limit), as it would call for higher GWP contributions from the electrolyzer and the storage systems, nor the maximum assessed (*i.e.* bordering the upper bound), as it would call for higher GWP contributions from the wind farm itself. Nevertheless, the first trend prevails due to the lower GWPs related to the electrolyzer and the storage systems (especially the latter, being one-time emissions) than those of renewable electricity generation; hence, the minimum lies closer to the feasibility limit.

Lastly, **Figure 6.6** shows the objective function associated with social sustainability (*i.e.* Φ_{OBJ}^{SOC}). Unlike the previous pillars, the optimal solution now calls for high renewable energy installed capacities. Indeed, neither solar parks nor wind farms are associated with fire and explosion hazards (according to the adopted metric), but instead, their increase in size leads to a decrease in the installed capacity of the electrolyzer and both electricity and hydrogen storages (hence in the overall hazard severity related to the plant). In other words, the most socially sustainable solution would be a green ammonia plant connected to a renewable electric grid, as it would ensure quasi-stationary operating regimes and exclude the need for storage systems and the oversizing of the electrolyzer (hence significantly lowering the overall process hazards).

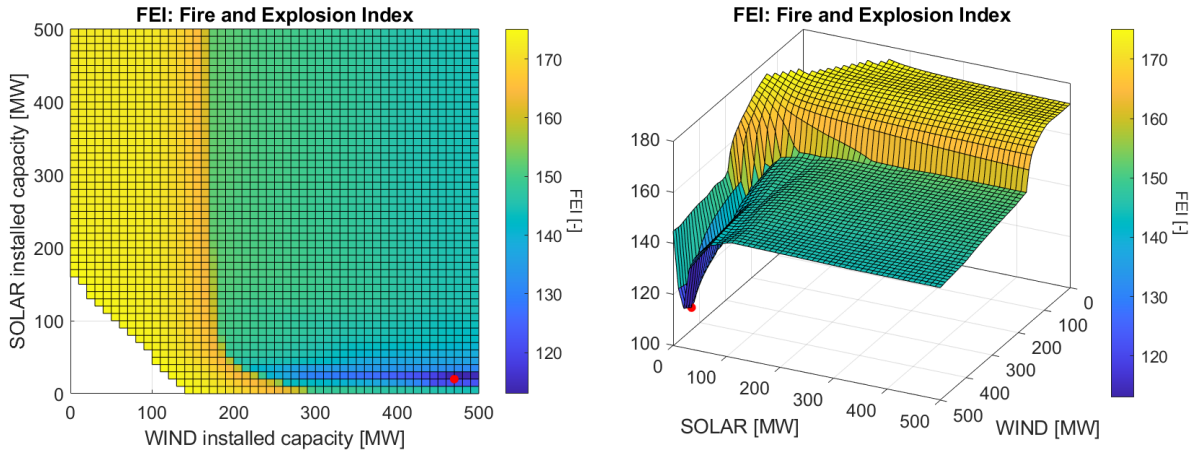

Figure 6.6: Two- (left) and three-dimensional (right) representations of the social sustainability objective function (Φ_{OBJ}^{SOC}, *i.e.* the total FEI). The red dot marks the minimum (*i.e.* the socially optimal solution). The white area in the 2D diagram represents the infeasible region (*i.e.* process configurations lacking sufficient installed power generation capacities to meet the ammonia productivity constraint).

Curiously, all SOO solutions encourage sourcing renewable energy from wind power; however, each does so for a different reason. First, economic sustainability benefits from wind power since it reduces the size of the electricity and hydrogen storage systems, hence both CapEx and OpEx of those sections. Indeed, wind profiles (according to the location assessed: California, USA) are much more persistent than solar ones (since wind is not subject to the day cycle as the sun is). This means higher

mitigation of the renewable energy demand throughout the nighttime and less need for auxiliary supply from the battery and hydrogen tanks. Second, environmental sustainability calls for high wind energy integration primarily because wind farms have lower GWPs than solar parks (see **Table 6.1**). This also explains the steep rise in Φ_{OBJ}^{ENV} when directed towards increasing solar installed capacities. However, as the total GWP reduces significantly with the decrease of installed capacities for power generation, the power plant is overstretched, leading to higher storage and electrolyzer sizes (as they show a minor impact on the GWP itself). Third, social sustainability follows similar considerations to the economic pillar: lower storage sizes (especially the hydrogen tanks) result in lower FEI values. Moreover, since no hazards are associated with renewable energy generation, the installed capacity of the wind farm increases tremendously in this regard, also reducing the electrolyzer size (indeed, the higher the energy input, the smaller the electrolyzer (Isella & Manca, 2024)), hence further mitigating the total FEI of the plant.

6.4.2. MOO results

Solving the three SOO problems together allows visualizing the Pareto fronts, *i.e.* those points within the decision space whose corresponding objective function values cannot be concurrently improved (Sepiacci *et al.*, 2017). This is a traditional "*a posteriori*" technique (*i.e.* postponing the decision process after the searching phase, thus no preference criteria need to be provided "*a priori*"), giving interesting information about the trade-off trends among the objective functions.

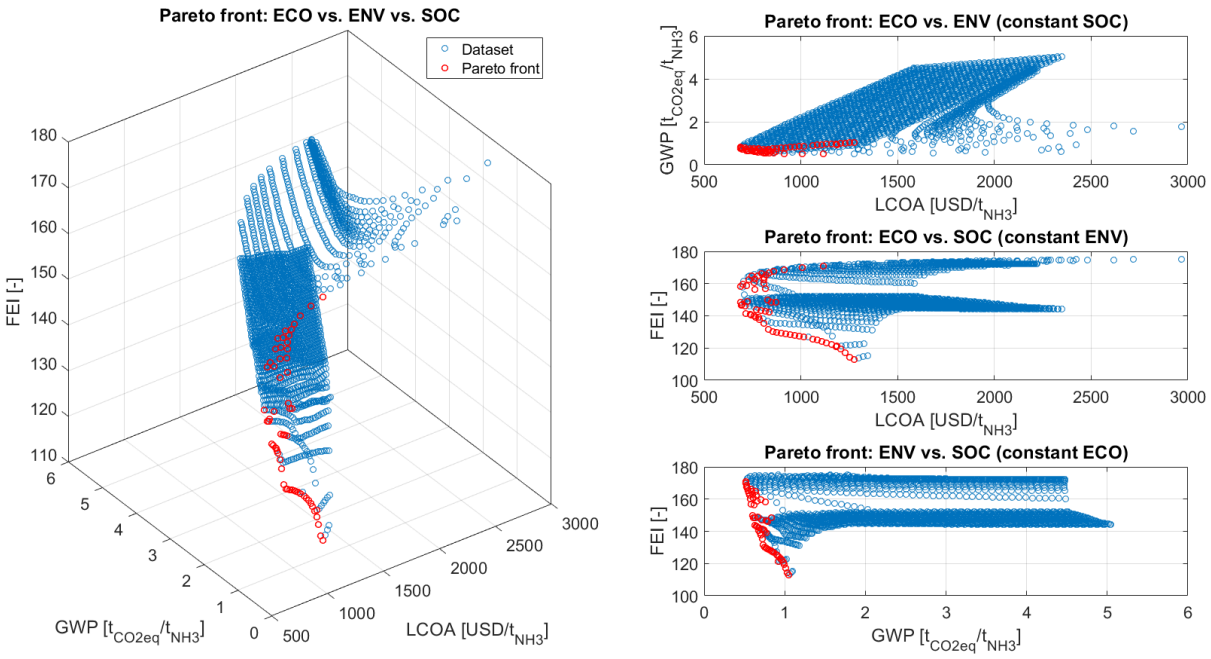

Figure 6.7: On the left, non-Pareto (blue dots) and Pareto (red dots) solutions for the general MOO problem. On the right, three corresponding two-dimensional representations of the Pareto fronts (*i.e.* pairing two pillars at a time).

Accordingly, from the results reported in **Figure 6.4**, **Figure 6.5**, and **Figure 6.6** (*i.e.* the LCOA, GWP, and FEI values scored by each investigated configuration), **Figure 6.7** shows the resulting three-dimensional (having assessed three different objective functions: Φ_{OBJ}^{ECO}, Φ_{OBJ}^{ENV}, and Φ_{OBJ}^{SOC}) Pareto front and the three two-dimensional Pareto fronts derived by slicing the former into three bi-objective optimization problems (to improve the graphical rendition and facilitate the reading). However, the Pareto front approach may be unsatisfactory and confusing for many reasons. Above all, the somewhat chaotic representation of all the solutions explored and the high number of Pareto optimal points (60 out of 2601 process configurations investigated, 117 of which were unfeasible), thus leaving still too much space for the decision maker's discretion. That is why we resorted to the scalarization method: as an "*a priori*" technique, it provides the decision criterion (assuming a specific hierarchy of importance in the objective functions) before the searching phase, hence allowing for the search of a unique solution. This was done by selecting a suitable set of weighting factors for each of the three pillars of sustainability (*e.g.*, $w_{ECO} = 60\%$; $w_{ENV} = 30\%$; and $w_{SOC} = 10\%$) and thus estimating the corresponding GSS.

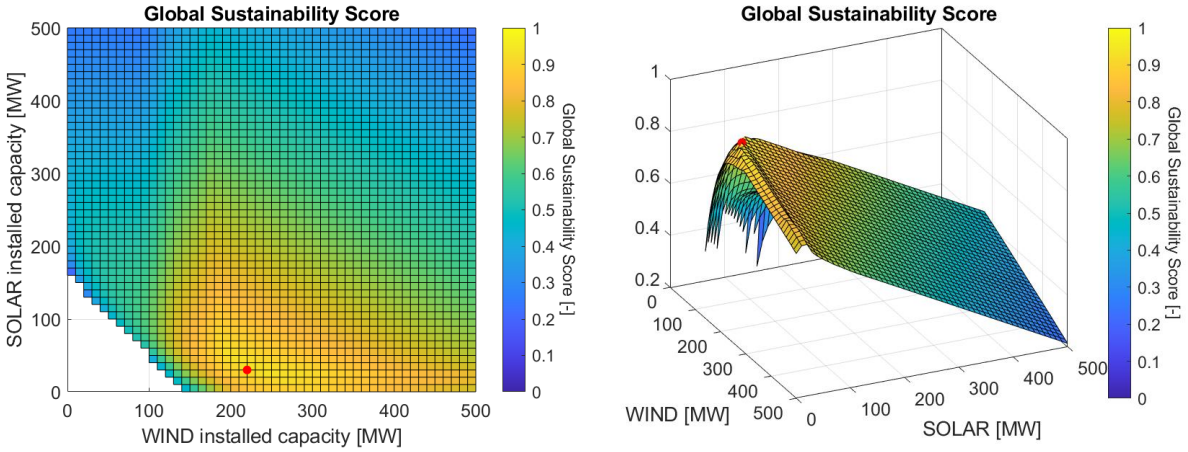

Figure 6.8: Two- (left) and three-dimensional (right) representations of the scalarized MOO problem (*i.e.* the Global Sustainability Score). In this case, 60%-ECO, 30%-ENV, and 10%-SOC weighting factors were applied. The red dot marks the maximum (*i.e.* the globally optimal solution). The white area in the 2D diagram represents the infeasible region (*i.e.* process configurations lacking sufficient installed power generation capacities to meet the productivity constraint).

Figure 6.8 reports the Global Sustainability Score according to the so-scalarized MOO problem (remembering from Eq. (6.8) that it corresponds to Φ_{OBJ}^{MOO} with a reversed sign, as required by the minimum formulation provided in Eq. (6.1)). Predictably, following the applied weighting factors, the maximum attainable Global Sustainability Score (equal to 0.93) is achieved for a process configuration very similar to the economically optimal one discussed previously. However, it differs by the slightly bigger capacity of the renewable power plant (*i.e.* 250 MW vs. 230 MW, which allows for reducing the total FEI) and, especially, a stronger dependence on wind power generation (*i.e.*

220 MW vs. 190 MW, which allows lowering the total GWP). Lastly, **Table 6.4** enables comparisons with the SOO results in more detail.

Table 6.4: Characteristic results of the optimal process configuration assessed through the scalarized MOO problem (60%-ECO, 30%-ENV, and 10%-SOC weighting factors). Specifically, the radar chart compares its objective function values with those corresponding to the SOO of each pillar of sustainability (see **Table 6.3**).

OPTIMAL SOLUTION		MOO	SOO vs. MOO graphical comparison
Solar park	[MW]	30	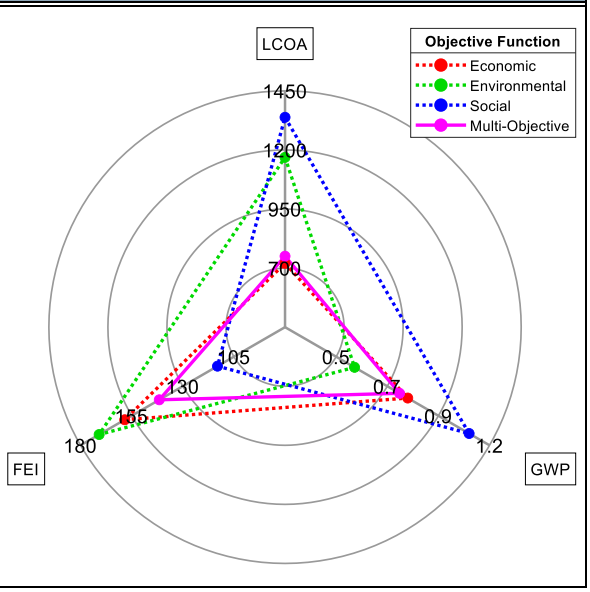
Wind farm	[MW]	220	
Electrolyzer	[MW]	43.91	
Hydrogen storage	[t_{H2}]	0.19	
Battery storage	[MWh]	3.96	
LCOA (Φ_{OBJ}^{ECO})	[USD/t_{NH3}]	750.40	
GWP (Φ_{OBJ}^{ENV})	[t_{CO2eq}/t_{NH3}]	0.76	
FEI (Φ_{OBJ}^{SOC})	[-]	141.48	
GSS ($-\Phi_{OBJ}^{MOO}$)	[-]	93%	

Therefore, compared to the Pareto front technique, the scalarization method proves more suitable in addressing the MOO problem of global sustainability and assessing the associated trade-offs. It consists of an intuitive and user-friendly approach that can be easily applied to process optimization at both the academic and industrial levels.

6.5. Conclusions

The present chapter introduced and discussed a methodology for the sustainable conceptual design of Power-to-Ammonia plants. Indeed, a global concern about sustainability and sustainable development has emerged in the last decades. As the chemical industry plays a leading role in international economic growth, making its manufacturing processes sustainable has become mandatory. Sustainability may be faced on three dimensions: economic, environmental, and social, *i.e.* the so-called "three pillars of sustainability". Specifically, we set up a multi-objective optimization strategy based on the scalarization technique to simultaneously address all of them, hence uniquely identifying the process configuration that achieves the maximum attainable global sustainability (here expressed through a "Global Sustainability Score"). Green ammonia production effectively shows very low carbon emissions (even from the cradle-to-grave perspective); however, it still calls for relatively high production costs (compared to conventional technologies) and involves hazardous

chemicals (above all, hydrogen) and process units (such as the electrolyzer and the hydrogen storage system) that lead to high hazard severity of the process. Optimization is compelling in designing and techno-economically assessing this and many other chemical industry applications that fall into the recently introduced class of Power-to-X processes.

Conclusions and future perspectives

The 2020s have been labeled the "decisive decade" for climate action (*A decisive decade*, 2021). Indeed, by the adoption of the Glasgow Climate Pact in 2021, over 190 countries acknowledged that "*limiting global warming to 1.5°C requires rapid, deep, and sustained reductions in global greenhouse gas emissions, including reducing global carbon dioxide emissions by 45% by 2030 relative to the 2010 level and to net zero around mid-century*" (UNFCCC, 2021). Equally, this decade is a critical time for the base chemical industry as the decisions that will be made in the next few years will determine the landscape of future production, its ability to meet future low-carbon energy demands, and its long-term success in meeting net-zero emissions by 2050. Accordingly, based on the best available scientific knowledge, the next years will necessitate strong and coordinated action from all actors (*e.g.*, policymakers, industry leaders, and financial institutions) to deliver rapid and sustained emissions reductions and thus meet the set climate targets.

Hopefully, the key value of this dissertation lies in having developed methodologies that are widely accessible not only for academic figures but also in industrial settings. Indeed, the latter often lack the same theoretical foundations and tools (*e.g.*, software) required to formulate and solve the rather complex optimization problems related to designing and operating renewable-powered chemical plants. Therefore, the objective of this thesis has been precisely to provide not only the scientific community but the industrial community as well (which, ultimately, is the one that makes the difference from the perspective of emissions and climate change mitigation) with tools that can support the sustainable design of chemical plants powered by renewable energy, characterized by great practicality both at an intuitive level of understanding and practical implementation. For instance, the two criteria proposed in Chapters 4 and 5 for hydrogen and electricity storage sizing show a paradigmatically different approach compared to conventional optimization-based methods. Indeed, rather than framing explicit optimization problems requiring design-and-scheduling formalization, direct analytical tools that identify optimal mass or power withdrawal patterns and resulting required sizes (calling for renewable energy profiles and downstream operational requirements only) are provided. Accordingly, an additional strength of the present dissertation presumably lies in providing an alternative, practical methodological framework that circumvents the need for formal optimization problem formulation altogether when designing mass and energy storage systems, whose need has been demonstrated essential in renewable-powered chemical plants.

Conversely, an apparent potential limitation in the adopted approach is the "gate-to-gate" perspective that has always been assumed throughout the featured discussions and techno-economical assessments (*e.g.*, in Chapters 1, 3, and 6). The sustainability impact of individual plants and production processes has indeed been quantified without considering any prior and subsequent phases (such as the procurement of raw materials or the transportation of products and their deployment on the market), thus providing an incomplete picture of the impact that such processes have on the entire Earth's ecosystem. Nevertheless, gate-to-gate is the distinctive standpoint of chemical engineers, who generally have the expertise and sensitivity only at the plant scale. Indeed, while presenting limitations concerning a global vision of environmental impact, this method offers significant advantages in specific contexts. Specifically, it allows for a more thorough and detailed analysis of chemical transformation processes, enabling targeted optimization of operational parameters that are directly under the control of process engineers. This focus is often necessary to develop practical solutions that can be immediately implemented in industry. On the other hand, the cradle-to-grave approach (or even more complete life cycle assessment) provides a more holistic understanding of environmental impact; still, it requires a significantly higher amount of data, interdisciplinary expertise, and computational resources. The consequential complexity can represent a barrier to its adoption by industry, especially for small and medium enterprises. Accordingly, the justification for the gate-to-gate approach in an academic-industrial context lies in its ability to balance scientific rigor with practical applicability. It is also worth noting that the gate-to-gate approach can constitute a fundamental first step toward more comprehensive analyses. Once processes are optimized at the plant level, extending the analysis to the entire value chain becomes easier. Indeed, in modern industrial sustainability strategies, methodological evolution is often observed that starts from gate-to-gate optimization and then gradually expands toward broader perspectives as expertise and available resources increase.

Concerning the lessons learned, this thesis has found that decarbonizing base-chemical processes (above all, ammonia synthesis) through the progressive replacement of fossil hydrogen with renewable hydrogen is possible and an "available-to-date" pathway. Indeed, although on a smaller scale than conventional technologies, it is possible to operate plants to synthesize fully green hydrogen and ammonia relying on renewable power plants and electrolyzers having fully compatible sizes with current industrial practices.

This leads to the inevitable clash with two revered paradigms of chemical engineering: (i) steady-state operations and (ii) economy of scale.

Concerning the former, previous chapters have repeatedly stressed the fundamental role of process flexibility (hence dynamic operations) in reconciling non-dispatchable renewable inputs with related chemical plants. Renewable energy sources such as solar and wind exhibit inherent variability across multiple temporal scales, from

minute-to-minute fluctuations to diurnal and seasonal patterns. This variability contrasts with the historical development of chemical processes, which evolved under the assumption of continuous mass and energy flows. However, enforcing steady-state operations on renewable-powered facilities requires extensive mass and energy buffer storage to flatten all fluctuations, thus increasing capital expenditure and operating costs. In this way, the economic implications of such buffer systems can undermine the financial viability of renewable integration, potentially delaying or preventing the transition away from fossil dependence. Conversely, the economic consequences of dynamic operations lead to highly competitive advantages. Chemical plants capable of adjusting their productivity to renewable energy availability require much smaller buffer storage systems (resulting in much lower capital and operating expenditures). Furthermore, thanks to their flexibility, such facilities can eventually participate in electricity markets as demand response resources, potentially generating additional revenue streams. This economic optimization potential represents a fundamental shift in operational strategy for chemical manufacturers. Still, the social advantages of steady-state operations, particularly regarding control and monitoring simplicity, must be carefully considered in the design of dynamically operated facilities. Indeed, addressing safety and control challenges remains essential. Enhanced safety systems and comprehensive operator training programs might help mitigate these concerns. Accordingly, developing inherently safer process technologies specifically designed for dynamic operation represents an important research direction.

Regarding the latter, as is widely known, an inverse relationship exists between the scale of production (*e.g.*, a chemical plant) and the unit cost of the product. The technological readiness level of renewable energy infrastructures (*e.g.*, power plants, electrolyzers, renewable electricity grids) might not allow replicating today the large scales reached by conventional plants (*e.g.*, 2000 MTD ammonia plants, consuming ca. 15 t_{H2}/h, would require at least 750 MW of electrolysis capacity to be entirely fed by green hydrogen) yet are already suitable for applications on smaller scales (as seen in previous chapters, by average consumption rates equal to 1 t_{H2}/h, producing ca. 136 MTD of ammonia requires about 50 MW of electrolysis capacity). However, this shift from large to small (or medium) scale should also be properly framed within the threefold sustainability perspective. Though production costs would inevitably rise, many other positive effects might arise from a social perspective (alongside the evident environmental advantages). Above all, "deglobalization" stands out: a phenomenon that has gained significant momentum in recent years, particularly within industrial sectors traditionally dependent on extensive global supply chains. This restructuring of production and resource acquisition paradigms has profound implications for the chemical industry, which stands at a critical juncture in its evolution from fossil-based to renewable-based processes. Indeed, the sudden resurgence of global hostilities has precipitated a fundamental reconsideration of supply chain security for fossil resources and essential raw materials. This geopolitical volatility has exposed the

inherent vulnerabilities of a chemical industry predicated on centralized production facilities and long-distance transportation networks. Traditionally, industrial progress has been characterized by economies of scale favoring large, consolidated operations near fossil fuel extraction sites or major transportation hubs. However, the resulting centralization has made the sector susceptible to supply disruptions from geopolitical tensions. Green hydrogen represents a disruptive alternative to such an established paradigm. The input requirements for its production (essentially water and renewable electricity) allow for restructuring fundamentally the chemical industry's geographic distribution. Rather than being tied to fossil resource extraction or major logistics corridors, production facilities can be established in diverse locations with access to renewable resources. This decentralization capacity leads to a previously unattainable resilience against geopolitical disruptions. Indeed, the rise of smaller, more numerous production nodes can potentially replace the historically dominant standard of large-scale centralized facilities. This dispersed architecture inherently enhances system resilience by eliminating bottlenecks and single points of failure, reducing dependency on extended supply chains crossing politically volatile regions. However, significant challenges remain in realizing this vision of a scattered, resilient chemical industry. The capital expenditure requirements for establishing green hydrogen infrastructure are substantial, and, as mentioned above, current production costs of green chemicals exceed those of conventional fossil-based alternatives. Despite these challenges, the trajectory towards deglobalization in the chemical industry appears increasingly inevitable. The recent convergence of geopolitical instability, climate imperatives, and technological advancement creates the conditions for a real structural transformation. As this transition progresses, we may witness the development of a chemical industry characterized by dispersed production, enhanced resilience, and minor environmental impact. The implications of this shift outspread beyond the chemical sector itself, potentially establishing a template for industrial and societal reorganization across multiple sectors. The principles of decentralization and resource autonomy enabled by renewable energy systems could reshape manufacturing paradigms more broadly, contributing to a more resilient and sustainable industrial ecosystem. In the specific cases addressed by the previous chapters, the solar and wind farms assessed in the feasibility studies of Power-to-X facilities may make renewable energy permeate even in surrounding manufacturing and urban activities, leading to higher environmental and social benefits for the local and national population.

Accordingly, future research should extend beyond traditional gate-to-gate process analysis to encompass the broader environmental and social context in which chemical facilities operate. The resulting control volume, evidently larger, demands “tailor-made” process solutions optimizing renewable energy integration and interconnection with the surrounding infrastructure. While such an approach transcends conventional chemical engineering boundaries, incorporating elements of land management, political economy, and supply chain logistics, process systems engineers are uniquely

positioned to address this multifaceted challenge. Their established expertise in process optimization provides the requisite computational foundation for navigating this complex interdisciplinary terrain. The future of the sustainable chemical industry depends on embracing this holistic perspective, transforming potential constraints into opportunities for wide-ranging optimization across traditionally segregated domains.

Bibliography

A decisive decade (2021). Nature Ecology & Evolution, 5, 1465-1465.

Akah, A., & Al-Ghrami, M. (2015). Maximizing propylene production via FCC technology. Applied Petrochemical Research, 5, 377-392.

Allen, D. T., & Shonnard, D. R. (2001). Green Engineering: Environmentally Conscious Design of Chemical Processes: Pearson Education.

Allied Market Research (2022). Toluene Market. Available online: https://www.alliedmarketresearch.com/toluene-market (accessed on June 29, 2022).

Althaus, H.-J., Chudacoff, M., Hischier, R., Jungbluth, N., Osses, M., & Primas, A. (2007). Life Cycle Inventories of Chemicals. Final report ecoinvent data v2.0 No. 8. Swiss Centre for Life Cycle Inventories. Available online.

American Institute of Chemical Engineers (2016). Dow's Fire and Explosion Index Hazard Classification Guide: Wiley.

Amir, M., Deshmukh, R. G., Khalid, H. M., Said, Z., Raza, A., Muyeen, S. M., Nizami, A.-S., Elavarasan, R. M., Saidur, R., & Sopian, K. (2023). Energy storage technologies: An integrated survey of developments, global economical/environmental effects, optimal scheduling model, and sustainable adaption policies. Journal of Energy Storage, 72, 108694.

Anastas, P. T., & Zimmerman, J. B. (2003). Design Through the 12 Principles of Green Engineering. Environmental Science & Technology, 37, 94A-101A.

Armijo, J., & Philibert, C. (2020). Flexible production of green hydrogen and ammonia from variable solar and wind energy: Case study of Chile and Argentina. International Journal of Hydrogen Energy, 45, 1541-1558.

Aromada, S. A., Eldrup, N. H., & Erik Øi, L. (2021). Capital cost estimation of CO2 capture plant using Enhanced Detailed Factor (EDF) method: Installation factors and plant construction characteristic factors. International Journal of Greenhouse Gas Control, 110, 103394.

Arsad, A. Z., Hannan, M. A., Al-Shetwi, A. Q., Begum, R. A., Hossain, M. J., Ker, P. J., & Mahlia, T. M. I. (2023). Hydrogen electrolyser technologies and their modelling for sustainable energy production: A comprehensive review and suggestions. International Journal of Hydrogen Energy, 48, 27841-27871.

Azapagic, A., & Clift, R. (1999). The application of life cycle assessment to process optimisation. Computers & Chemical Engineering, 23, 1509-1526.

Azapagic, A., & Perdan, S. (2005). An integrated sustainability decision-support framework Part II: Problem analysis. International Journal of Sustainable Development & World Ecology, 12, 112-131.

Azmi, A., & Aziz, N. (2017). Comparison Study of Model Based Industrial Low-Density Polyethylene Production in Tubular Reactor. Chemical Engineering Transactions, 56, 751-756.

Bach, P. W., Haije, W. G., Neelis, M. L., & Patel, M. K. (2005). Analysis of energy use and carbon losses in the chemical and refinery industries. Available online.

Bakshi, B. R., & Fiksel, J. (2003). The quest for sustainability: Challenges for process systems engineering. AIChE Journal, 49, 1350-1358.

Belis, D., Marcu, A., Stoefs, W., & Tuokko, K. (2015). Sectoral case study – Soda ash: Climate for Sustainable Growth: CEPS Centre for European Policy Studies.

Beroe (2020a). LDPE (Low Density Polyethylene) Market Intelligence. Available online: https://www.beroeinc.com/category-intelligence/ldpe-market/ (accessed on May 11, 2022).

Beroe (2020b). LLDPE (Linear low-density polyethylene) Market Intelligence. Available online: https://www.beroeinc.com/category-intelligence/lldpe-market/ (accessed on May 11, 2022).

Beroe (2020c). Phenol Market Intelligence. Available online: https://www.beroeinc.com/category-intelligence/phenol-market/ (accessed on May 11, 2022).

Bicer, Y., Dincer, I., Zamfirescu, C., Vezina, G., & Raso, F. (2016). Comparative life cycle assessment of various ammonia production methods. Journal of Cleaner Production, 135, 1379-1395.

BlueWeave Consulting (2022a). Global High-Density Polyethylene (HDPE) Market to Boost in Coming Years – Projected to Reach 78.0 Million Tons by 2028 | BlueWeave Consulting. Available online: https://www.globenewswire.com/en/news-release/2022/03/24/2409624/0/en/Global-High-Density-Polyethylene-HDPE-Market-to-Boost-in-Coming-Years-Projected-to-Reach-78-0-Million-Tons-by-2028-BlueWeave-Consulting.html (accessed on May 11, 2022).

BlueWeave Consulting (2022b). Global Polyethylene Terephthalate (PET) Resin Market to Boost in Coming Years – Projected to Reach Worth 114.7 Million Tons in 2028 | BlueWeave Consulting. Available online: https://www.globenewswire.com/en/news-release/2022/04/04/2415938/0/en/Global-Polyethylene-Terephthalate-PET-

Resin-Market-to-Boost-in-Coming-Years-Projected-to-Reach-Worth-114-7-Million-Tons-in-2028-BlueWeave-Consulting.html (accessed on May 11, 2022).

Böcker, N., Grahl, M., Tota, A., Häussinger, P., Leitgeb, P., & Schmücker, B. (2013). Nitrogen. Ullmann's Encyclopedia of Industrial Chemistry,1-27.

BP (2021). Statistical Review of World Energy. BP. Available online: https://www.bp.com/content/dam/bp/business-sites/en/global/corporate/pdfs/energy-economics/statistical-review/bp-stats-review-2021-full-report.pdf.

Byrne, E. P., & Fitzpatrick, J. J. (2009). Chemical engineering in an unsustainable world: Obligations and opportunities. Education for Chemical Engineers, 4, 51-67.

CAISO (2021). Managing Integration of Renewables and Distributed Energy Resources (DERs) into the Transmission System in Deregulated Markets. California Independent System Operator. Available online: https://www.caiso.com/Documents/Presentation-Managing-Renewable-Integration-in-CAISO.pdf.

CAISO (2024). California Independent System Operator. Available online: https://www.caiso.com/.

ChemAnalyst (2021). Mono Ethylene Glycol (MEG) Market Analysis: Plant Capacity, Production, Operating Efficiency, Technology, Demand & Supply, Application, Distribution Channel, Regional Demand, 2015-2030. Available online: https://www.chemanalyst.com/industry-report/mono-ethylene-glycol-meg-market-646 (accessed on June 24, 2022).

ChemIntel360 (2021). Global Benzene Market - Trends, COVID-19 impact and Growth Forecasts to 2026. Available online: https://www.chemintel360.com/reportdetails/Global-Benzene-Market/24 (accessed on June 29, 2022).

Chen, C., & Yang, A. (2021). Power-to-methanol: The role of process flexibility in the integration of variable renewable energy into chemical production. Energy Conversion and Management, 228, 113673.

Chen, C., Yang, A., & Bañares-Alcántara, R. (2021). Renewable methanol production: Understanding the interplay between storage sizing, renewable mix and dispatchable energy price. Advances in Applied Energy, 2, 100021.

Cheng, M., Verma, P., Yang, Z., & Axelbaum, R. L. (2022). Flexible cryogenic air separation unit—An application for low-carbon fossil-fuel plants. Separation and Purification Technology, 302, 122086.

Climate Watch (2022). Historical GHG Emissions. Available online: https://www.climatewatchdata.org/ghg-

emissions?breakBy=sector&chartType=area&end_year=2019&sectors=total-including-lucf&start_year=1990 (accessed on June 8, 2022).

Congress.gov (2022). H.R.5376 - Inflation Reduction Act of 2022. Available online: https://www.congress.gov/bill/117th-congress/house-bill/5376 (accessed on February 15, 2025).

Congressional Budget Office (2013). Effects of a Carbon Tax on the Economy and the Environment. Congressional Budget Office. Available online: https://www.cbo.gov/publication/44223.

Corona, A., Biddy, M. J., Vardon, D. R., Birkved, M., Hauschild, M. Z., & Beckham, G. T. (2018). Life cycle assessment of adipic acid production from lignin. Green Chemistry, 20, 3857-3866.

David, M., Ocampo-Martínez, C., & Sánchez-Peña, R. (2019). Advances in alkaline water electrolyzers: A review. Journal of Energy Storage, 23, 392-403.

de Groot, M. T., Kraakman, J., & Garcia Barros, R. L. (2022). Optimal operating parameters for advanced alkaline water electrolysis. International Journal of Hydrogen Energy, 47, 34773-34783.

de Jong, M., Reinders, A. H. M. E., Kok, J. B. W., & Westendorp, G. (2009). Optimizing a steam-methane reformer for hydrogen production. International Journal of Hydrogen Energy, 34, 285-292.

DEA (2020). Technology Data for Energy Storage. Danish Energy Agency. Available online: https://ens.dk/en/our-services/projections-and-models/technology-data/technology-data-energy-storage.

DEA (2022). Technology Data for Generation of Electricity and District Heating. Danish Energy Agency. Available online: https://ens.dk/en/our-services/technology-catalogues/technology-data-generation-electricity-and-district-heating.

DOE (2023). End-of-Life Management for Solar Photovoltaics. Available online: https://www.energy.gov/eere/solar/end-life-management-solar-photovoltaics (accessed on October 10, 2023).

DOE (2025). Greenhouse gases, Regulated Emissions, and Energy use in Technologies (GREET®). Available online: https://www.energy.gov/eere/greet.

Douglas, J. M. (1988). Conceptual Design of Chemical Processes: McGraw-Hill.

ECHEMI (2022). Propylene oxide: from a gap of 467,000 tons to self-sufficiency is just around the corner. Available online: https://www.echemi.com/cms/257860.html (accessed on June 24, 2022).

EERE (2001). Hydrogen Fuel Cell Engines and Related Technologies Course Manual. Office of Energy Efficiency & Renewable Energy. Available online: https://www.energy.gov/eere/fuelcells/articles/hydrogen-fuel-cell-engines-and-related-technologies-course-manual.

EIA (2022). U.S. ammonia prices rise in response to higher international natural gas prices. Available online: https://www.eia.gov/todayinenergy/detail.php?id=52358 (accessed on September 29, 2023).

EPA (2024). Scope 1 and Scope 2 Inventory Guidance. U.S. Environmental Protection Agency. Available online: https://www.epa.gov/climateleadership/scope-1-and-scope-2-inventory-guidance (accessed on October 10, 2024).

Euro Chlor (2010). The European Chlor-Alkali industry: an electricity intensive sector exposed to carbon leakage. Euro Chlor. Available online.

European Commission (2019). Paris Agreement. Available online: https://ec.europa.eu/clima/eu-action/international-action-climate-change/climate-negotiations/paris-agreement_en (accessed on June 8, 2022).

European Commission (2022). REPowerEU: Affordable, secure and sustainable energy for Europe. Available online: https://commission.europa.eu/strategy-and-policy/priorities-2019-2024/european-green-deal/repowereu-affordable-secure-and-sustainable-energy-europe_en (accessed on December 13, 2023).

European Commission, Joint Research Centre, Boulamanti, A., & Moya, J. (2017). Energy efficiency and GHG emissions: prospective scenarios for the chemical and petrochemical industry: Publications Office.

Fischer, I., Schmitt, W. F., Porth, H.-C., Allsopp, M. W., & Vianello, G. (2014). Poly(Vinyl Chloride). Ullmann's Encyclopedia of Industrial Chemistry, 1-30.

Fraunhofer ISE (2021). Cost Forecast for Low-Temperature Electrolysis. Fraunhofer Institute for Solar Energy Systems ISE. Available online.

Genova, G., & Panza, S. (2022). Casale flexible green ammonia plant, the economically viable green production. In CRU Nitrogen+Syngas 35th Int. Conf. & Exhibition.

Global CCS Institute (2021). Global Status of CCS 2021: CCS Accelerating to Net Zero. Available online: https://www.globalccsinstitute.com/wp-content/uploads/2021/10/2021-Global-Status-of-CCS-Report_Global_CCS_Institute.pdf.

Grossmann, I. E., & Guillén-Gosálbez, G. (2010). Scope for the application of mathematical programming techniques in the synthesis and planning of sustainable processes. Computers & Chemical Engineering, 34, 1365-1376.

Guilbert, D., Collura, S. M., & Scipioni, A. (2017). DC/DC converter topologies for electrolyzers: State-of-the-art and remaining key issues. International Journal of Hydrogen Energy, 42, 23966-23985.

Gutsch, M., & Leker, J. (2022). Global warming potential of lithium-ion battery energy storage systems: A review. Journal of Energy Storage, 52, 105030.

Herzog, T., Pershing, J., & Baumert, K. A. (2005). Navigating the Numbers: Greenhouse Gas Data and International Climate Policy. World Resources Institute. Available online: https://www.wri.org/research/navigating-numbers.

IEA (2007). Tracking Industrial Energy Efficiency and CO2 Emissions. International Energy Agency. Available online: https://www.iea.org/reports/tracking-industrial-energy-efficiency-and-co2-emissions.

IEA (2020). Average annual capacity factors by technology, 2018. International Energy Agency. Available online: https://www.iea.org/data-and-statistics/charts/average-annual-capacity-factors-by-technology-2018 (accessed on November 13, 2024).

IEA (2021). Electricity Information: Overview. International Energy Agency. Available online: https://www.iea.org/reports/electricity-information-overview (accessed on June 22, 2022).

IEA (2021). Is carbon capture too expensive? International Energy Agency. Available online: https://www.iea.org/commentaries/is-carbon-capture-too-expensive.

IEA (2023). Global Hydrogen Review 2023. International Energy Agency. Available online: https://www.iea.org/reports/global-hydrogen-review-2023.

IEA (2023). World Energy Outlook 2023. International Energy Agency. Available online.

IEA, ICCA, & DECHEMA (2013). Technology Roadmap – Energy and GHG Reductions in the Chemical Industry via Catalytic Processes. International Energy Agency. Available online.

IFA (2021a). Nitrogen Products: Ammonia. International Fertilizer Association. Available online: https://www.ifastat.org/supply/Nitrogen%20Products/Ammonia (accessed on June 23, 2022).

IFA (2021b). Nitrogen Products: Urea. International Fertilizer Association. Available online: https://www.ifastat.org/supply/Nitrogen%20Products/Urea (accessed on June 23, 2022).

IFA (2021c). Processed Phosphates. International Fertilizer Association. Available online:

https://www.ifastat.org/supply/Phosphate%20Products/Processed%20Phosphates (accessed on June 23, 2022).

IHS Markit (2016). Ethylene - Global. Available online: https://cdn.ihs.com/www/pdf/Steve-Lewandowski-Big-Changes-Ahead-for-Ethylene-Implications-for-Asia.pdf (accessed on June 29, 2022).

IHS Markit (2020a). Chemical Economics Handbook: Ethylbenzene. Available online: https://ihsmarkit.com/products/ethylbenzene-chemical-economics-handbook.html (accessed on May 4, 2022).

IHS Markit (2020b). Ethylene Market Outlook considering the impact of COVID-19. Available online: https://ihsmarkit.com/research-analysis/ethylene-market-outlook-considering-the-impact-of-covid19.html (accessed on May 4, 2022).

IHS Markit (2021). Chemical Economics Handbook: Vinyl Chloride Monomer (VCM). Available online: https://ihsmarkit.com/products/vinyl-chloride-monomer-chemical-economics-handbook.html (accessed on May 4, 2022).

IHS Markit (2022). Chemical Economics Handbook: para-Xylene. Available online: https://ihsmarkit.com/products/paraxylene-chemical-economics-handbook.html (accessed on May 4, 2022).

Incer-Valverde, J., Korayem, A., Tsatsaronis, G., & Morosuk, T. (2023). "Colors" of hydrogen: Definitions and carbon intensity. Energy Conversion and Management, 291, 117294.

International Labour Organisation (1993). Major Hazard Control: A Practical Manual. An ILO Contribution to the International Programme on Chemical Safety of UNEP, ILO, WHO (IPCS): I.L.O.

Intratec (2023a). Cooling Water Current Costs, Historical Series & Forecasts. Available online: https://www.intratec.us/products/water-utility-costs/commodity/cooling-water-cost (accessed on December 18, 2023).

Intratec (2023b). Demineralized Water Current Costs, Historical Series & Forecasts. Available online: https://www.intratec.us/products/water-utility-costs/commodity/demineralized-water-cost (accessed on December 18, 2023).

Invest Saudi (2021a). Adipic Acid: Investment Opportunity Scorecard. Available online: https://investsaudi.sa/medias/Adipic-Acid.pdf?context=bWFzdGVyfHBvcnRhbC1tZWRpYXwzNjY3MjN8YXBwbGljYXRpb24vcGRmfHBvcnRhbC1tZWRpYS9oNDgvaGZmLzg5MDk1OTI5NTI4NjIucGRmfGMzMjkxMTk1MTNhYzZhNTllZGFmNjA4OWE2OWQyNzczNzkwZjdjYWUyNTI5OWFlZDg4ODEwN2I1ODg3N2Q2YTU (accessed on May 27, 2022).

Invest Saudi (2021b). Nitric Acid (HNO3): Investment Opportunity Scorecard. Available online: https://investsaudi.sa/medias/Nitric-Acid-HNO3-

.pdf?context=bWFzdGVyfHBvcnRhbC1tZWRpYXw1MDczNDV8YXBwbGljYXRpb24vcGRmfHBvcnRhbC1tZWRpYS9oMDgvaDllLzg5MDk1OTM5MzU5MDIucGRmfDkxZTlkYmUyYzU1ODMwMjU3NWNkMWY1ZjdhM2I5NDdkNTk1NjE2YTRkYzRmNTkzYjE0NDQxN2IwOWFmNTIzOTI (accessed on May 27, 2022).

IPCC (2006). 2006 IPCC Guidelines for National Greenhouse Gas Inventories. Intergovernmental Panel on Climate Change. Available online: https://www.ipcc-nggip.iges.or.jp/public/2006gl/pdf/2_Volume2/V2_1_Ch1_Introduction.pdf.

IRENA (2017). Electricity storage and renewables: Costs and markets to 2030. International Renewable Energy Agency. Available online: http://www.irena.org/publications/2017/Oct/Electricity-storage-and-renewables-costs-and-markets.

IRENA (2019). Innovation landscape brief: Utility-scale batteries. International Renewable Energy Agency. Available online.

IRENA (2019). Innovation landscape brief: Utility-scale batteries. International Renewable Energy Agency. Available online: https://www.irena.org/publications/2019/Sep/Utility-scale-batteries.

IRENA (2020). Renewable power generation costs in 2019. International Renewable Energy Agency. Available online.

IRENA (2023). Renewable power generation costs in 2022. International Renewable Energy Agency. Available online.

IRENA, & Methanol Institute (2021). Innovation Outlook: Renewable Methanol. Available online: https://www.irena.org/-/media/Files/IRENA/Agency/Publication/2021/Jan/IRENA_Innovation_Renewable_Methanol_2021.pdf.

Isella, A., & Manca, D. (2022). GHG Emissions by (Petro)Chemical Processes and Decarbonization Priorities—A Review. Energies, 15.

Isella, A., & Manca, D. (2024). Green Hydrogen Production from Solar-powered Electrolysis: A Novel Optimization Methodology. Computer Aided Chemical Engineering, 53, 2365-2370.

Isella, A., & Manca, D. (2025a). A framework for the design of battery energy storage systems in Power-to-X processes. Journal of Energy Storage, 123, 116744.

Isella, A., & Manca, D. (2025b). A general criterion for the design and operation of flexible hydrogen storage in Power-to-X processes. International Journal of Hydrogen Energy, 99, 649-660.

Isella, A., Lista, A., Colombo, G., Ostuni, R., & Manca, D. (2023). Gray and hybrid green ammonia price sensitivity to market fluctuations: the Russia-Ukraine war case. Computer Aided Chemical Engineering, 52, 2285-2290.

Isella, A., Ostuni, R., & Manca, D. (2024). Towards the decarbonization of ammonia synthesis – A techno-economic assessment of hybrid-green process alternatives. Chemical Engineering Journal, 486, 150132.

Jing, L., El-Houjeiri, H. M., Monfort, J.-C., Brandt, A. R., Masnadi, M. S., Gordon, D., & Bergerson, J. A. (2020). Carbon intensity of global crude oil refining and mitigation potential. Nature Climate Change, 10, 526-532.

Kaufman, N., Barron, A. R., Krawczyk, W., Marsters, P., & McJeon, H. (2020). A near-term to net zero alternative to the social cost of carbon for setting carbon prices. Nature Climate Change, 10, 1010-1014.

Kern, C., & Jess, A. (2021). Reducing Global Greenhouse Gas Emissions to Meet Climate Targets—A Comprehensive Quantification and Reasonable Options. Energies, 14.

Klöpffer, W. (2005). Life Cycle Assessment in the Mirror of Int J LCA: Past, Present, Future. The International Journal of Life Cycle Assessment, 10, 379-380.

Klöpffer, W., & Grahl, B. (2014). Life Cycle Impact Assessment. Life Cycle Assessment (LCA), 181-328.

Knop, V. (2022). Life Cycle Analysis of hydrogen storage tanks. AWOE: A World of Energy. Available online: https://www.awoe.net/Hydrogen-Storage-LCA.html (accessed on September 24th, 2024).

Krishnan, S., Corona, B., Kramer, G. J., Junginger, M., & Koning, V. (2024). Prospective LCA of alkaline and PEM electrolyser systems. International Journal of Hydrogen Energy, 55, 26-41.

Krungsri Research (2019). Petrochemical Industry. Available online: https://www.krungsri.com/bank/getmedia/ab0bcb7e-f3ba-42f5-929f-47ce1ce12bb4/IO_Petrochemicals_190626_EN_EX.aspx (accessed on June 24, 2022).

Li, H. (2023). Solid state battery, what's next? Next Energy, 1, 100007.

Li, J., Lin, J., & Song, Y. (2020). Capacity Optimization of Hydrogen Buffer Tanks in Renewable Power to Ammonia (P2A) System. In 2020 IEEE Power & Energy Society General Meeting (PESGM) (pp. 1-5).

LyondellBasell (2015). Optimized Ziegler-Natta Catalysts for Gas Phase PP Processes. LyondellBasell. Available online: https://www.lyondellbasell.com/globalassets/products-technology/technology/gas-phase-pp-processes.pdf.

Manca, D. (2007). Calcolo numerico applicato: Pitagora.

Marocco, P., Gandiglio, M., & Santarelli, M. (2024). Optimal design of PV-based grid-connected hydrogen production systems. Journal of Cleaner Production, 434, 140007.

McPhy (2023). McLyzer product line: Pressurized alkaline electrolysis. Available online.

Meessen, J. H. (2010). Urea. Ullmann's Encyclopedia of Industrial Chemistry.

Merchant Research and Consulting Ltd. (2022). Ethylene Dichloride (EDC): 2022 World Market Outlook and Forecast up to 2031. Available online: https://mcgroup.co.uk/researches/ethylene-dichloride-edc (accessed on June 24, 2022).

Methanol Institute (2019). Methanol as a vessel fuel & energy carrier. Available online: https://www.methanol.org/wp-content/uploads/2019/09/Methanol-as-a-vessel-fuel-and-energy-carrier.pdf (accessed on June 29, 2022).

Miettinen, K., & Mäkelä, M. M. (2002). On scalarizing functions in multiobjective optimization. OR Spectrum, 24, 193-213.

MMSA (2022). MMSA Global Methanol Supply and Demand Balance. Available online: https://www.methanol.org/methanol-price-supply-demand/ (accessed on June 24, 2022).

Mordor Intelligence (2021a). Chlorine Market - Growth, Trends, COVID-19 Impact, And Forecasts (2022 - 2027). Available online: https://www.mordorintelligence.com/industry-reports/chlorine-market (accessed on May 27, 2022).

Mordor Intelligence (2021b). Cumene Market - Growth, Trends, COVID-19 Impact, And Forecasts (2022 - 2027). Available online: https://www.mordorintelligence.com/industry-reports/cumene-market (accessed on May 27, 2022).

Morud, J. C., & Skogestad, S. (1998). Analysis of instability in an industrial ammonia reactor. AIChE Journal, 44, 888-895.

MPP (2022). Making Net-Zero 1.5°C-Aligned Ammonia Possible. Mission Possible Partnership. Available online: https://www.energy-transitions.org/publications/making-net-zero-ammonia-possible/.

Mucci, S., Mitsos, A., & Bongartz, D. (2023a). Cost-optimal Power-to-Methanol: Flexible operation or intermediate storage? Journal of Energy Storage, 72, 108614.

Mucci, S., Mitsos, A., & Bongartz, D. (2023b). Power-to-X processes based on PEM water electrolyzers: A review of process integration and flexible operation. Computers & Chemical Engineering, 175, 108260.

Nayak-Luke, R., Bañares-Alcántara, R., & Wilkinson, I. (2018). "Green" Ammonia: Impact of Renewable Energy Intermittency on Plant Sizing and Levelized Cost of Ammonia. Industrial & Engineering Chemistry Research, 57, 14607-14616.

Nel Hydrogen (2021). Nel Hydrogen Electrolyzers: The World's Most Efficient and Reliable Electrolysers. Available online: https://nelhydrogen.com/wp-content/uploads/2020/03/Electrolysers-Brochure-Rev-D.pdf.

Nel Hydrogen (2023). Nel Hydrogen Official Website. Available online: https://nelhydrogen.com/ (accessed on October 3, 2023).

Nexant (2009). Propylene Oxide. Nexant. Available online: https://engage.aiche.org/HigherLogic/System/DownloadDocumentFile.ashx?DocumentFileKey=a8300833-1d78-4d92-b692-1a1fd7548cfe&ssopc=1.

NexantECA (2020). Global Styrene Market Snapshot. Available online: https://www.nexanteca.com/blog/202009/global-styrene-market-snapshot (accessed on June 24, 2022).

Noelker, K., & Ruether, J. (2011). Low Energy Consumption Ammonia Production: Baseline Energy Consumption, Options for Energy Optimization. In Nitrogen & Syngas 2011 International Conference & Exhibition. Duesseldorf. Germany.

NRC, U. S. (2023). Capacity factor. U.S. Nuclear Regulatory Commission. Available online: https://www.nrc.gov/reading-rm/basic-ref/glossary/capacity-factor.html (accessed on November 12, 2024).

Osman, O., Sgouridis, S., & Sleptchenko, A. (2020). Scaling the production of renewable ammonia: A techno-economic optimization applied in regions with high insolation. Journal of Cleaner Production, 271, 121627.

Osyczka, A. (1978). An approach to multicriterion optimization problems for engineering design. Computer Methods in Applied Mechanics and Engineering, 15, 309-333.

Our World in Data (2022). Total greenhouse gas emissions. Available online: https://ourworldindata.org/explorers/co2?facet=none&country=~OWID_WRL&Gas=All+GHGs+%28CO%E2%82%82eq%29&Accounting=Production-based&Fuel=Total&Count=Per+country&Relative+to+world+total=false (accessed on June 8, 2022).

Our World in Data (2024). Carbon intensity of electricity generation. Available online: https://ourworldindata.org/grapher/carbon-intensity-electricity?time=latest.

Pexapark (2023). PEXA EURO COMPOSITE. Available online: https://pexapark.com/pexaquote-freemium/ (accessed on October 16, 2023).

Prieto, C., Blindu, A., Cabeza, L. F., Valverde, J., & García, G. (2024). Molten Salts Tanks Thermal Energy Storage: Aspects to Consider during Design. In Energies (Vol. 17).

ReportLinker (2021). Global Acrylonitrile Industry. Available online: https://www.reportlinker.com/p05817756/Global-Acrylonitrile-Industry.html?utm_source=GNW (accessed on June 24, 2022).

Rey, S. O., Romero, J. A., Romero, L. T., Martínez, À. F., Roger, X. S., Qamar, M. A., Domínguez-García, J. L., & Gevorkov, L. (2023). Powering the Future: A Comprehensive Review of Battery Energy Storage Systems. In Energies (Vol. 16).

Rivera, A., Movalia, S., Pitt, H., & Larsen, K. (2021). Preliminary 2020 Global Greenhouse Gas Emissions Estimates. Available online: https://rhg.com/research/preliminary-2020-global-greenhouse-gas-emissions-estimates/ (accessed on June 8, 2022).

Robèrt, K. H. (2002). The Natural Step Story: Seeding a Quiet Revolution: New Society Publishers.

Rossi, F., Zuffi, C., Parisi, M. L., Fiaschi, D., & Manfrida, G. (2023). Comparative scenario-based LCA of renewable energy technologies focused on the end-of-life evaluation. Journal of Cleaner Production, 405, 136931.

Sánchez, A., & Martín, M. (2018). Optimal renewable production of ammonia from water and air. Journal of Cleaner Production, 178, 325-342.

Scotti, F., Fabricatore, N., & Manca, D. (2018). Multi-objective optimization of sustainability criteria in the design of chemical plants. Computer Aided Chemical Engineering, 43,743-748.

Scotti, F., Fabricatore, N., Sepiacci, P., & Manca, D. (2017). A MOO approach towards sustainable process design: integrating the three pillars of sustainability. Computer Aided Chemical Engineering, 40,637-642.

Sepiacci, P., Depetri, V., & Manca, D. (2017). A systematic approach to the optimal design of chemical plants with waste reduction and market uncertainty. Computers & Chemical Engineering, 102, 96-109.

Sheppard, D., & Hodgson, C. (2021). Cost of polluting in EU soars as carbon price hits record €50. In Financial Times.

Shin, B.-J., Mun, J.-H., Devkota, S., Kim, S.-M., Kang, T.-H., Mazari, S. A., Cho, K., Kim, S. H., Chun, D.-H., Kim, K.-M., Yoon, H. C., & Moon, J.-H. (2023). Comparative assessment and multi-objective optimization for the gray and

blue ammonia synthesis processes: Energy, Economic and Environmental (3E) analysis. International Journal of Hydrogen Energy, 48, 35123-35138.

Simbeck, D., & Beecy, D. (2011). The CCS paradox: The much higher CO2 avoidance costs of existing versus new fossil fuel power plants. Energy Procedia, 4, 1917-1924.

Soave, G., Pellegrini, L., Barbatti, D., Susani, N., & Bonomi, S. (2006). Energy saving in distillation columns: the Linde column revisited. Computer Aided Chemical Engineering, 21,645-650.

Statista (2022a). Market volume of benzene worldwide from 2015 to 2021, with a forecast for 2022 to 2029. Available online: https://www.statista.com/statistics/1245172/benzene-market-volume-worldwide/ (accessed on June 23, 2022).

Statista (2022b). Market volume of ethylene oxide worldwide from 2015 to 2021, with a forecast for 2022 to 2029. Available online: https://www.statista.com/statistics/1245260/ethylene-oxide-market-volume-worldwide/ (accessed on June 23, 2022).

Statista (2022c). Market volume of polypropylene worldwide from 2015 to 2021, with a forecast for 2022 to 2029. Available online: https://www.statista.com/statistics/1245169/polypropylene-market-volume-worldwide/ (accessed on June 23, 2022).

Statista (2022d). Market volume of purified terephthalic acid worldwide from 2015 to 2021, with a forecast for 2022 to 2029. Available online: https://www.statista.com/statistics/1245249/purified-terephthalic-acid-market-volume-worldwide/ (accessed on June 23, 2022).

Statista (2022e). Market volume of soda ash worldwide from 2015 to 2021, with a forecast for 2022 to 2029. Available online: https://www.statista.com/statistics/1245254/soda-ash-market-volume-worldwide/ (accessed on June 23, 2022).

Statista (2022f). Xylene demand and production capacity worldwide from 2015 to 2022. Available online: https://www.statista.com/statistics/1246700/xylene-demand-capacity-forecast-worldwide/ (accessed on June 23, 2022).

Statista (2022g). Market volume of toluene worldwide from 2015 to 2021, with a forecast for 2022 to 2029. Available online: https://www.statista.com/statistics/1245224/toluene-market-volume-worldwide (accessed on June 23, 2022).

Statista (2022h). Propylene demand and capacity worldwide from 2015 to 2022. Available online: https://www.statista.com/statistics/1246689/propylene-demand-capacity-forecast-worldwide/ (accessed on June 23, 2022).

Statista (2022i). Market volume of sulfuric acid worldwide from 2015 to 2021, with a forecast for 2022 to 2029. Available online: https://www.statista.com/statistics/1245226/sulfuric-acid-market-volume-worldwide/ (accessed on June 30, 2022).

Stefanis, S. K., Livingston, A. G., & Pistikopoulos, E. N. (1995). Minimizing the environmental impact of process Plants: A process systems methodology. Computers & Chemical Engineering, 19, 39-44.

Stephanopoulos, G. (1984). Chemical Process Control: An Introduction to Theory and Practice: Prentice-Hall.

Syed, F. H., & Vernon, W. D. (2002). Status of Low Pressure PE Process Licensing. Chemical Market Resources, Inc. Available online: https://www.researchgate.net/profile/Prem_Baboo/post/What_is_the_compositions_of_HDPE_reactors_for_slurry_process/attachment/59d6280579197b80779865fb/AS%3A328309301891076%401455286445317/download/Status+of+Low+Pressure+Polyehtylene+-+LDPE++Process+Technology+Licensing+CMR+Inc+Analysis.pdf.

The Brattle Group (2017). The Future of Cap-and-Trade Program in California: Will Low GHG Prices Last Forever? The Brattle Group, Inc. Available online.

The Royal Society (2020). Ammonia: zero-carbon fertiliser, fuel and energy store. The Royal Society. Available online: https://royalsociety.org/-/media/policy/projects/green-ammonia/green-ammonia-policy-briefing.pdf.

ThyssenKrupp (2022). Large-scale water electrolysis for green hydrogen production. Available online: https://ucpcdn.thyssenkrupp.com/_binary/UCPthyssenkruppBAISUhdeChlorineEngineers/en/products/water-electrolysis-hydrogen-production/210622-gH2-product-brochure.pdf.

Trading Economics (2023). EU Natural Gas. Available online: https://tradingeconomics.com/commodity/eu-natural-gas (accessed on October 11, 2023).

UNFCCC (2021). Glasgow Climate Pact: Decision -/CMA.3. United Nations Framework Convention on Climate Change. Available online: https://unfccc.int/documents/310497.

UNFCCC (2022). The Paris Agreement. United Nations Framework Convention on Climate Change. Available online: https://unfccc.int/process-and-meetings/the-paris-agreement/the-paris-agreement (accessed on June 8, 2022).

United Nations (1992). Agenda 21: UNCED.

United Nations (2019). World Population Prospects 2019. Available online: https://population.un.org/wpp/ (accessed on June 8, 2022).

United States Senate: Committee on Finance (2010). Statement of ANSAC on the U.S.–China Trade Relationship: Finding a New Path Forward.

Vecchi, A., Li, Y., Ding, Y., Mancarella, P., & Sciacovelli, A. (2021). Liquid air energy storage (LAES): A review on technology state-of-the-art, integration pathways and future perspectives. Advances in Applied Energy, 3, 100047.

Wang, S., Zhang, P., Zhuo, T., & Ye, H. (2023). Scheduling power-to-ammonia plants considering uncertainty and periodicity of electricity prices. Smart Energy, 11, 100113.

Weiss, R., & Ikäheimo, J. (2024). Flexible industrial power-to-X production enabling large-scale wind power integration: A case study of future hydrogen direct reduction iron production in Finland. Applied Energy, 365, 123230.

World Commission on Environment and Development (1987). Our Common Future: Oxford University Press.

WRI (2021). World Greenhouse Gas Emissions: 2018. World Resources Institute. Available online: https://www.wri.org/data/world-greenhouse-gas-emissions-2018 (accessed on June 9, 2022).

Young, D. M., & Cabezas, H. (1999). Designing sustainable processes with simulation: the waste reduction (WAR) algorithm. Computers & Chemical Engineering, 23, 1477-1491.

Zhang, X., Gao, Z., Zhou, B., Guo, H., Xu, Y., Ding, Y., & Chen, H. (2024). Advanced Compressed Air Energy Storage Systems: Fundamentals and Applications. Engineering.

Zimmerman, M. (1979). Marx and Heidegger on the Technological Domination of Nature. Philosophy Today, 23, 99-112.

A Appendix

A.1. Air separation unit (ASU)

Equation of State: Redlich-Kwong-Soave

Material streams

	A1	A2	A3	A4	A5
Temperature [°C]	30.00	108.98	40.00	121.39	40.00
Pressure [bar]	1.01	1.98	1.93	3.76	3.71
Mass Flow [t/h]	4.75	4.75	4.75	4.75	4.75
Molar Fraction: N_2	78.11%	78.11%	78.11%	78.11%	78.11%
Molar Fraction: O_2	20.96%	20.96%	20.96%	20.96%	20.96%
Molar Fraction: Ar	0.93%	0.93%	0.93%	0.93%	0.93%

	A6	A7	A8	A9	A10
Temperature [°C]	94.14	30.00	30.00	30.00	-173.80
Pressure [bar]	5.85	5.80	5.80	5.80	5.70
Mass Flow [t/h]	4.75	4.75	0.71	4.04	4.04
Molar Fraction: N_2	78.11%	78.11%	78.11%	78.11%	78.11%
Molar Fraction: O_2	20.96%	20.96%	20.96%	20.96%	20.96%
Molar Fraction: Ar	0.93%	0.93%	0.93%	0.93%	0.93%

	A11	A12	A13	A14	A15
Temperature [°C]	-177.77	-173.91	-133.20	-174.79	-177.90
Pressure [bar]	5.60	5.70	5.70	1.30	5.55
Mass Flow [t/h]	3.31	2.55	0.71	0.71	3.31
Molar Fraction: N_2	99.88%	64.72%	78.11%	78.11%	99.88%
Molar Fraction: O_2	0.00%	33.86%	20.96%	20.96%	0.00%
Molar Fraction: Ar	0.12%	1.42%	0.93%	0.93%	0.12%

	BoilUp	Bottoms	Distillate	Reflux	To-BoilUp
Temperature [°C]	-180.26	-180.26	-177.90	-177.89	-180.26
Pressure [bar]	1.35	1.35	5.55	5.60	1.35
Mass Flow [t/h]	3.43	1.14	1.49	1.82	3.43
Molar Fraction: N_2	0.83%	0.84%	99.88%	99.90%	0.84%
Molar Fraction: O_2	96.15%	96.14%	0.00%	0.00%	96.14%
Molar Fraction: Ar	3.02%	3.02%	0.12%	0.10%	3.02%

	To-Reflux-1	To-Reflux-2	A16	A17	A18
Temperature [°C]	-177.90	-177.89	-190.41	-194.27	-180.45
Pressure [bar]	5.55	5.60	1.30	1.20	1.35
Mass Flow [t/h]	1.82	1.82	2.55	1.49	4.57
Molar Fraction: N_2	99.88%	99.88%	64.72%	99.88%	0.84%
Molar Fraction: O_2	0.00%	0.00%	33.86%	0.00%	96.14%
Molar Fraction: Ar	0.12%	0.12%	1.42%	0.12%	3.02%

	A19	A20	A21	A22
Temperature [°C]	-180.26	-194.20	23.52	25.00
Pressure [bar]	1.35	1.20	1.10	1.25
Mass Flow [t/h]	4.57	3.60	3.60	1.14
Molar Fraction: N_2	0.84%	99.53%	99.53%	0.84%
Molar Fraction: O_2	96.14%	0.12%	0.12%	96.14%
Molar Fraction: Ar	3.02%	0.35%	0.35%	3.02%

Energy streams

	Wcomp1	Qcool1	Wcomp2	Qcool2
Power [kW]	105.60	92.55	109.09	109.57

	Wcomp3	Qcool3	Wpump	Wexp
Power [kW]	72.35	86.31	0.005	7.25

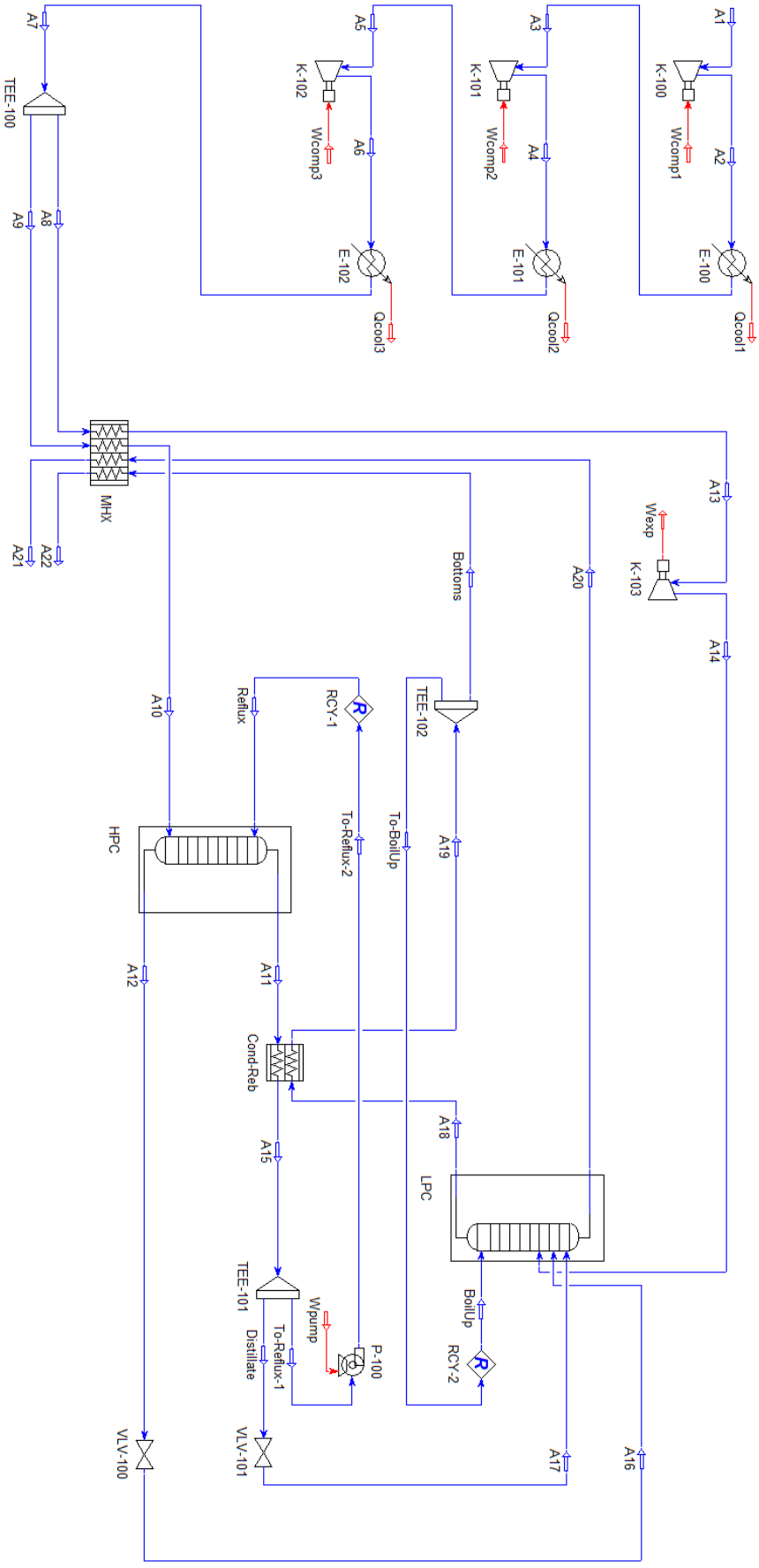

Figure A.1: UniSim® flowsheet of the simulated ASU model.

A.2. Hydrogen compression (HC)

Equation of State: Peng-Robinson

Material streams

	H2-to-Tank	B1	B2	B3
Temperature [°C]	25.00	150.00	25.00	155.23
Pressure [bar]	30.00	76.42	76.32	200.00
Mass Flow [t/h] (*)	1.00	1.00	1.00	1.00
Molar Fraction: H_2	100.00%	100.00%	100.00%	100.00%

(*) Base of Calculus

Energy streams

	Wc-HC1	Qc-HC1	Wc-HC2
Power [kW]	498.42	497.84	531.16

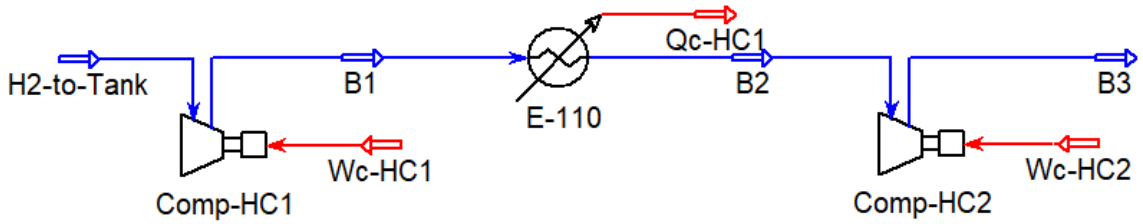

Figure A.2: UniSim® flowsheet of the simulated HC model.

A.3. Haber-Bosch process (HB)

Equation of State: Redlich-Kwong-Soave

Material streams

	H2 feed	N2 feed	C1	C2	C3
Temperature [°C]	25.00	25.00	24.01	131.23	30.00
Pressure [bar]	30.00	30.00	30.00	72.00	71.95
Mass Flow [t/h]	0.78	3.60	4.38	4.38	4.38
Molar Fraction: N_2	0.00%	99.53%	24.83%	24.83%	24.83%
Molar Fraction: O_2	0.00%	0.12%	0.03%	0.03%	0.03%
Molar Fraction: Ar	0.00%	0.35%	0.09%	0.09%	0.09%
Molar Fraction: H_2	100.00%	0.00%	75.05%	75.05%	75.05%
Molar Fraction: NH_3	0.00%	0.00%	0.00%	0.00%	0.00%

	C4	C4.1	C4.2	C5.1	C5.2
Temperature [°C]	139.63	30.00	46.65	29.90	150.00
Pressure [bar]	172.68	172.63	200.00	200.00	199.95
Mass Flow [t/h]	4.38	4.38	4.38	21.76	21.76
Molar Fraction: N_2	24.83%	24.83%	24.83%	24.66%	24.66%
Molar Fraction: O_2	0.03%	0.03%	0.03%	0.28%	0.28%
Molar Fraction: Ar	0.09%	0.09%	0.09%	2.89%	2.89%
Molar Fraction: H_2	75.05%	75.05%	75.05%	66.17%	66.17%
Molar Fraction: NH_3	0.00%	0.00%	0.00%	6.01%	6.01%

	C6	C7	C8	C9	C10
Temperature [°C]	150.00	150.00	150.00	300.00	372.07
Pressure [bar]	199.95	199.95	199.95	199.90	199.89
Mass Flow [t/h]	13.06	4.35	4.35	13.06	13.06
Molar Fraction: N_2	24.66%	24.66%	24.66%	24.66%	23.56%
Molar Fraction: O_2	0.28%	0.28%	0.28%	0.28%	0.29%
Molar Fraction: Ar	2.89%	2.89%	2.89%	2.89%	3.01%
Molar Fraction: H_2	66.17%	66.17%	66.17%	66.17%	62.53%
Molar Fraction: NH_3	6.01%	6.01%	6.01%	6.01%	10.61%

	C11	C12	C13	C14	C15
Temperature [°C]	200.00	328.90	483.88	250.00	436.28
Pressure [bar]	199.90	199.89	199.85	199.90	199.85
Mass Flow [t/h]	4.35	17.41	17.41	4.35	21.76
Molar Fraction: N_2	24.66%	23.85%	21.26%	24.66%	22.01%
Molar Fraction: O_2	0.28%	0.28%	0.31%	0.28%	0.30%
Molar Fraction: Ar	2.89%	2.98%	3.28%	2.89%	3.19%
Molar Fraction: H_2	66.17%	63.47%	54.90%	66.17%	57.39%
Molar Fraction: NH_3	6.01%	9.42%	20.25%	6.01%	17.10%

	C16	C17	C18	C19	C20
Temperature [°C]	486.34	486.34	486.34	486.34	385.81
Pressure [bar]	199.82	199.82	199.82	199.82	199.77
Mass Flow [t/h]	21.76	4.35	4.35	13.06	4.35
Molar Fraction: N_2	21.12%	21.12%	21.12%	21.12%	21.12%
Molar Fraction: O_2	0.31%	0.31%	0.31%	0.31%	0.31%
Molar Fraction: Ar	3.29%	3.29%	3.29%	3.29%	3.29%
Molar Fraction: H_2	54.45%	54.45%	54.45%	54.45%	54.45%
Molar Fraction: NH_3	20.82%	20.82%	20.82%	20.82%	20.82%

	C21	C22	C23	C24	C25
Temperature [°C]	436.49	334.25	365.19	238.02	25.00
Pressure [bar]	199.77	199.77	199.77	199.72	199.67
Mass Flow [t/h]	4.35	13.06	21.76	21.76	21.76
Molar Fraction: N_2	21.12%	21.12%	21.12%	21.12%	21.12%
Molar Fraction: O_2	0.31%	0.31%	0.31%	0.31%	0.31%
Molar Fraction: Ar	3.29%	3.29%	3.29%	3.29%	3.29%
Molar Fraction: H_2	54.45%	54.45%	54.45%	54.45%	54.45%
Molar Fraction: NH_3	20.82%	20.82%	20.82%	20.82%	20.82%

	C26	C28	C29	C30	C31
Temperature [°C]	25.00	27.45	27.45	27.45	25.00
Pressure [bar]	199.67	50.00	50.00	50.00	199.67
Mass Flow [t/h]	4.37	4.37	4.32	0.05	17.38
Molar Fraction: N_2	0.47%	0.47%	0.15%	23.66%	24.53%
Molar Fraction: O_2	0.04%	0.04%	0.03%	0.84%	0.36%
Molar Fraction: Ar	0.13%	0.13%	0.06%	5.19%	3.82%
Molar Fraction: H_2	0.78%	0.78%	0.16%	44.85%	63.31%
Molar Fraction: NH_3	98.58%	98.58%	99.60%	25.47%	7.99%

	C33	C34	C35	C36	C37
Temperature [°C]	25.19	20.91	20.91	20.91	18.85
Pressure [bar]	200.00	10.00	10.00	10.00	10.00
Mass Flow [t/h]	17.38	4.32	4.17	0.15	0.05
Molar Fraction: N_2	24.53%	0.15%	0.00%	4.08%	23.66%
Molar Fraction: O_2	0.36%	0.03%	0.01%	0.73%	0.84%
Molar Fraction: Ar	3.82%	0.06%	0.00%	1.50%	5.19%
Molar Fraction: H_2	63.31%	0.16%	0.00%	4.56%	44.85%
Molar Fraction: NH_3	7.99%	99.60%	99.98%	89.14%	25.47%

	C38	Recycle	NH3 product
Temperature [°C]	19.15	25.19	-32.56
Pressure [bar]	10.00	200.00	1.01
Mass Flow [t/h]	0.20	17.38	4.17
Molar Fraction: N_2	9.62%	24.61%	0.00%
Molar Fraction: O_2	0.76%	0.36%	0.00%
Molar Fraction: Ar	2.54%	3.81%	0.00%
Molar Fraction: H_2	15.96%	63.23%	0.00%
Molar Fraction: NH_3	71.11%	7.99%	99.99%

Energy streams

	Wcomp4	Qcool4	Wcomp5	Qcool5
Power [kW]	452.04	423.95	478.70	467.95

	Wcomp6	Qcool6	Wcomp7
Power [kW]	75.66	4818.12	2.64

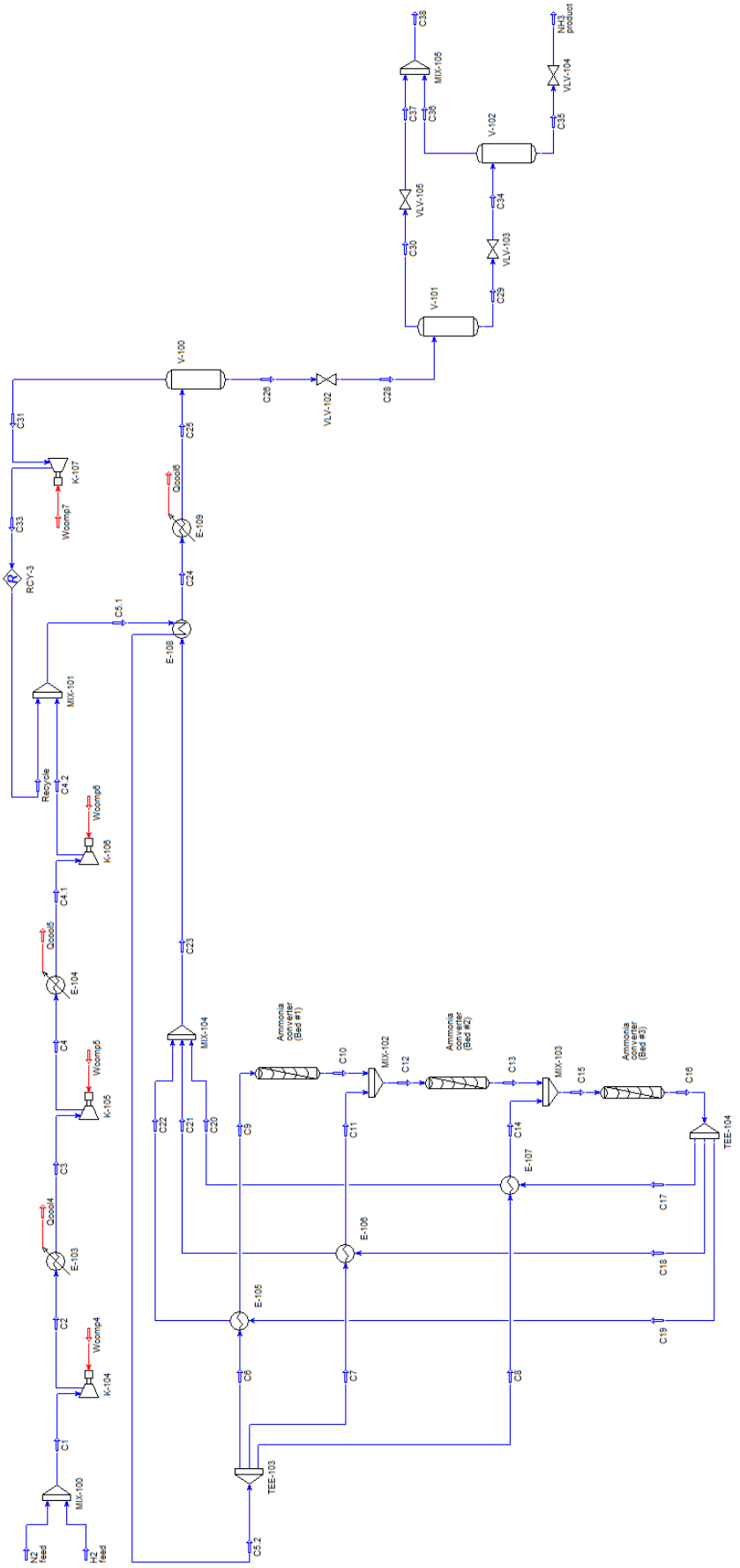

Figure A.3: UniSim® flowsheet of the simulated HB model.

List of Figures

List of Tables

Notation

Acronyms and Abbreviations

2D	Two-Dimensional
AEM	Anion Exchange Membrane Electrolyzer
ASU	Air Separation Unit
AWE	Alkaline Water Electrolyzer
BESS	Battery Energy Storage System
CAISO	California Independent System Operator
CapEx	Capital Expenditure
CCUS	Carbon Capture, Utilization, and Storage
CF	Capacity Factor
CW	Cooling Water
DC	Direct Current
$deCO_2$	Overall decarbonization extent
DMW	Demineralized Water
DR1	Throughput decrease in the primary reformer
EL	Electrolyzer
EU	European Union
FEI	Fire and Explosion Index
G2GHR	Green-to-gray hydrogen ratio
GSS	Global Sustainability Score
GWP	Global Warming Potential
HB	Haber-Bosch process
HC	Hydrogen compression
HS	Hydrogen storage
LCA	Life Cycle Assessment
LCOA	Levelized Cost of Ammonia

LCOH	Levelized Cost of Hydrogen
MOO	Multi-Objective Optimization
MTD	Metric Tons per Day
NG	Natural gas
O&M	Operation & Maintenance
OpEx	Operating Expenditure
PEM	Proton Exchange Membrane Electrolyzer
PPA	Power Purchase Agreement
PV	Photovoltaic
SOE	Solid Oxide Electrolyzer
SOO	Single-Objective Optimization
ST	Hydrogen compression and storage
USA	United States of America
USD	United States Dollar
VALCOE	Value-Adjusted Levelized Cost of Electricity

Latin symbols

E	Electric energy, [MWh]
$\dot{E}$	Electric power, [MW]
$EcoSI$	Economic Sustainability Index, [-]
$EnvSI$	Environmental Sustainability Index, [-]
m	Mass, [t]
$\dot{m}$	Mass flow, [t/h]
NY	Lifetime, [y]
P	Power capacity, [MW]
r	Discount rate, [-]
$SocSI$	Social Sustainability Index, [-]
t	Time (step), [h]
w	Weighting factor, [-]

Greek symbols

Δt	Time interval (temporal discretization), [h]
η	Efficiency, [-]
ξ	Electricity consumption, [MWh/Nm^3]
ρ	Mass density, [t/Nm^3]
σ_{SD}	Self-discharge rate, [1/h]
τ	Time (step) index, [h]
Φ_{OBJ}	Objective function

Subscripts and Superscripts

add	Additional
B	Battery
C	Charging (Battery)
curt	Curtailment (Electricity)
D	Discharging (Battery)
E	Electrolyzer
ECO	Economic sustainability
ENV	Environmental sustainability
G	Electric grid
grid	Grid (Electricity)
H	Hydrogen compression and storage
H_2	Hydrogen
i	i-th configuration
IN	Inlet
inst	Installed
j	j-th process section
k	k-th time step
min	Minimum
max	Maximum
n	n-th operating year

NH_3	Ammonia
OUT	Outlet
S	Solar
SD	Self-discharge (Battery)
SOC	Social sustainability
target	Target (*i.e.* at nominal conditions)
tot	Total
W	Wind
y	Annual

Acknowledgments

I miei più vivi sentimenti di gratitudine al prof. Davide Manca, per avermi guidato al suo prezioso sapere con animo probo e paterno, e ai miei genitori, per essere stati un modello che non avrebbe potuto essere migliore dal punto di vista morale.

ENG: *The research activities underlying this thesis were made possible thanks to the financial support received under the European project PON FSE REACT-EU, and the resources allocated by Ministerial Decree No. 1061 of August 10, 2021, for active and accredited doctoral programs in the framework of the XXXVII cycle.*

ITA: *Le attività di ricerca alla base di questa tesi sono state possibili grazie al sostegno finanziario ricevuto nell'ambito del progetto europeo PON FSE REACT-EU, e le risorse assegnate dal Decreto Ministeriale del 10 agosto 2021, n. 1061, per percorsi di dottorato di ricerca attivi e accreditati nell'ambito del XXXVII ciclo.*